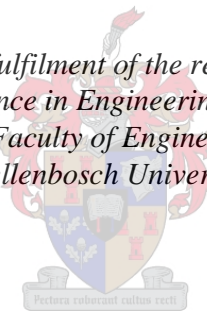# Design methodology of an axial-flow turbine for a micro jet engine

by
Johan George Theron Basson

Thesis presented in partial fulfilment of the requirements for the degree of
Master of Science in Engineering (Mechanical)
in the Faculty of Engineering at
Stellenbosch University

Supervisor: Prof. T.W. von Backström
Co-supervisor: Dr S.J. van der Spuy

December 2014

DECLARATION

By submitting this thesis electronically, I declare that the entirety of the work contained therein is my own, original work, that I am the sole author thereof (save to the extent explicitly otherwise stated), that reproduction and publication thereof by Stellenbosch University will not infringe any third party rights and that I have not previously in its entirety or in part submitted it for obtaining any qualification.

Date: ....

i

Abstract

Design methodology of an axial-flow turbine for a micro jet engine

J.G.T. Basson

Department of Mechanical and Mechatronic Engineering, Stellenbosch University,
Private Bag X1, Matieland 7602, South Africa
Thesis: MEng. (Mechanical)

December 2014

The main components of a micro gas turbine engine are a centrifugal or mixed-flow compressor, a combustion chamber and a single stage axial-flow or radial-flow turbine. The goal of this thesis is to formulate a design methodology for small axial-flow turbines. This goal is pursued by developing five design-related capabilities and applying them to develop a turbine for an existing micro gas turbine engine. Firstly, a reverse engineering procedure for producing digital three-dimensional models of existing turbines is developed. Secondly, a procedure for generating candidate turbine designs from performance requirement information is presented. The third capability is to use independent analysis procedures to analyse the performance of a turbine design. The fourth capability is to perform structural analysis to investigate the behavior of a turbine design under static and dynamic loading. Lastly, a manufacturing process for prototypes of a feasible turbine design is developed. The reverse engineering procedure employs point cloud data from a coordinate measuring machine and a CT-scanner to generate a three-dimensional model of the turbine in an existing micro gas turbine engine. The design generation capability is used to design three new turbines to match the performance of the turbine in the existing micro gas turbine engine. Independent empirical and numerical turbine performance analysis procedures are developed. They are applied to the four turbine designs and, for the new turbine designs, the predicted efficiency values differ by less than 5% between the two procedures. A finite element analysis is used to show that the stresses in the roots of the turbine rotor blades are sufficiently low and that the dominant excitation frequencies do not approach any of the blade natural frequencies. Finally prototypes of the three new turbine designs are manufactured through an investment casting process. Patterns made of an organic wax-like material and a polystyrene material are used, with the former yielding superior results.

Opsomming

'n Ontwerpsmetodologie van 'n aksiaalvloei-turbine vir 'n mikro-gasturbiene-enjin

J.G.T. Basson

Departement van Meganiese en Megatroniese Ingenieurswese, Universiteit van Stellenbosch,
Privaatsak X1, Matieland 7602, Suid-Afrika
Tesis: MIng. (Meganies)

Desember 2014

Mikro-gasturbiene-enjins bestaan uit 'n sentrifugaal- of 'n gemende-vloeikompressor, 'n verbrandingsruim en 'n enkel-stadium-aksiaalvloei- of 'n radiaalvloei-turbine. Die doel van hierdie tesis is om 'n ontwerpsmetodologie vir klein aksiaalvloei-turbines saam te stel. Hierdie doel word deur die ontwikkeling en toepassing van vyf ontwerpsverwante vermoëns nagestreef. Eerstens word 'n tru-waartse-ingenieursproses ontwikkel om drie-dimensionele rekenaarmodelle van die bestaande turbines te skep. Tweedens word 'n metode om kandidaatturbineontwerpe vanaf werkverrigtingsvereistes te verkry, voorgestel. Die derde ontwerpsvermoë is om die werksverrigting van 'n turbineontwerp met onafhanklike analises te evalueer. Die vierde ontwerpsvermoë is om die struktuur van 'n turbinelem te analiseer sodat die effek van statiese en dinamiese belastings ondersoek kan word. Laastens word 'n vervaardigingsproses vir prototipes van geskikte turbineontwerpe ontwikkel. Die tru-waartse-ingenieursproses maak gebruik van 'n koördinaat-meet-masjien en 'n CT-skandeerder om puntewolkdata vanaf die turbine in 'n bestaande mikro-gasturbiene-enjin te verkry. Die data word dan gebruik om 'n drie-dimensionele model van die turbine te skep. Die ontwerpskeppingsvermoë word dan gebruik om drie kandidaatturbineontwerpe vir die bestaande mikro-gasturbiene-enjin te skep. Onafhanklike empiriese en numeriese prosedures om die werkverrigting van 'n turbineontwerp te analiseer word ontwikkel. Beide prosedures word op die vier turbineontwerpe toegepas. Daar word gevind dat die voorspelde benuttingsgraadwaardes van die nuwe ontwerpe met minder as 5% verskil vir die twee prosedures. 'n Eindige-element-analise word dan gebruik om te wys dat die spannings in die wortels van die turbinelemme laag genoeg is, asook dat die dominante opwekkingsfrekwensies nie die lem se natuurlike frekwensies nader nie. Laastens word prototipes van die drie nuwe turbineontwerpe deur 'n beleggingsgietproses vervaardig. In die vervaardigingproses word die effektiwiteit van twee materiale vir die gietpatrone

getoets, naamlik 'n organiese wasagtige materiaal en 'n polistireen-materiaal. Daar word bevind dat die gebruik van die wasagtige gietpatrone tot beter resultate lei.

Acknowledgements

I would not have completed this project had it not been for certain people.

My Lord and Savior Jesus Christ, for the peace and hope I have in Him.

My father, Anton, who has always set an example and never has shied away from telling me what I need to hear.

My mother, Erina. Your willing company and unconditional support has always kept me confident and positive.

My friends and family. You have supported me and kept me interested throughout the duration of my studies.

My supervisors: Prof. T.W. von Backström for his patience and interesting stories and Dr. S.J. van der Spuy for optimism and guidance.

My wife, Elsje. Going home to you is what I look forward to at the end of every day.

To my parents

Table of contents

List of figures

List of tables

Nomenclature

Roman symbols

Symbol	Meaning
A	Area
a	Gas sonic velocity
b_z	Axial chord
C	Absolute gas velocity
C_L	Lift coefficient
$\boldsymbol{c}$	Vector representing the starting point of a line in parametric space
c	Point on a straight line at the zero parameter value, blade chord
d	Diameter
$\boldsymbol{E}$	Vector representing the squared error of the three linear approximations in parametric space
E	Squared error of a linear approximation in parametric space
e	Roughness height, calculation error
F_{AR}	Aspect ratio correction factor, area ratio correction
f_0	Static pressure ratio across the stator blade row
f_1	Static pressure ratio across the rotor blade row
H	Blade height
h	Gas specific enthalpy
I	Moment of inertia of a fluid particle
i	Index running from 1 to k or from 0 to 3, incidence angle
i_s	Stalling incidence angle
i_{sr}	ξ-Dependent term of the stalling incidence angle
Δi_s	(s/c)-Dependent stalling incidence angle correction

j	Index running from 1 to n
K_1	Factor used in calculating the compressibility correction factor, factor used in calculating the turbine efficiency estimate
K_2	Standard tip clearance approximation
K_{inc}	Off-design Incidence angle correction factor
K_M	Mach number correction factor for the profile loss coefficient
K_{mod}	Modern blade design modification factor for the profile loss coefficient
K_p	Compressibility correction factor
$K_R E$	Reynolds number correction factor
K_s	Modified form of the compressibility correction factor
k	Number of sampled points on a given blade profile
L	Angular momentum
l	Camber line length
l_{tot}	Total camber line length
M	Gas flow Mach number
M'	Relative gas flow Mach number
$\widetilde{M}'$	Modified relative mach number
$\boldsymbol{m}$	Vector representing the slope of a line in parametric space
m	Slope of the straight line
$\dot{m}$	Mass flow rate
N	Rotational speed, revolutions per minute
n	Number of blade profiles
P	Power output
$\boldsymbol{p}$	Vertex in three-dimensional space
p	Pressure

R	Reaction ratio
R_{air}	Gas constant for dry air, 278 J/kg/K
R_c	Uncovered turning radius
r	Radius
s	Blade pitch
s^o	Gas specific temperature dependend entropy
T	Temperature
t	Blade profile thickness
U	Blade velocity
W	Relative gas velocity
X	Reaction ratio dependent aspect ratio correction
X_1	Shock loss contribution parameter
X_2	Diffusion loss contribution parameter
X_{is}	(s/c)-Dependent parameters used to calculate Δi_s
X_p	Factor used in calculating the compressibility correction factor
x	Cartesian coordinate running along the blade length
Y	Relative total pressure loss coefficient, or component thereof
Y_{CL}	Blade tip clearance loss coefficient
Y_p	Profile loss coefficient
Y_{p1}	Pure nozzle blade profile loss coefficient
Y_{p2}	Impulse blade profile loss coefficient
Y_s	Secondary flow loss coefficient
$\tilde{Y}_s$	Preliminary secondary flow loss coefficient
Y_S	Stator blade row relative total pressure loss coefficient

Y_{SH}	Shock loss coefficient
$\tilde{Y}_{SH}$	Preliminary shock loss coefficient estimate
ΔY_{TE}	Trailing edge loss correction factor
y	Cartesian coordinate running tangent to the circumferential direction
Z	Ainley loading parameter
z	Cartesian and polar coordate running in the axial direction, axial length
Δz	Axial gap between stator and rotor

Greek symbols

Symbol	Meaning
α	Gas flow angle
α'	Relative flow angle
α'_m	Mean relative flow angle
β	Blade angle
β_g	Blade gauge angle
γ	Stagger angle
δ	Tip clearance or deviation angle
δ_0	Zero relative exit Mach number deviation angle
η_{tt}	Turbine total-to-total efficiency
μ	Gas dynamic viscosity
ξ	Gas deflection ratio
ϕ	Stage flow coefficient
ψ	Stage work coefficient
ω	Angular velocity
ξ	Gas deflection ratio

xvi

Subscripts

Symbol	Meaning
b	Generic blade angle convention
C	Compressor
h	Hub
in	Inlet property
m	Mean, or at mean radius
max	Maximum
opt	Optimal
out	Outlet
s	Shroud
T	Turbine
t	Total conditions
x	Cartesian coordinate along the blade length
y	Cartesian coordinate tangent to the circumferential direction
z	Cartesian and polar coordinate in the axial direction
θ	Circumferential direction
$0, 1, 2, 3$	Indices denoting positions throughout a turbine stage

Acronyms

ATM	–	Automatic Topology and Meshing
BMT	–	Baird Micro Turbine
CFD	–	Computational Fluid Dynamics
CMM	–	Coordinate Measuring Machine
CSIR	–	Council for Scientific and Industrial Research

CT	–	Computed Tomography
EM	–	Empirical Model
FEM	–	Finite Element Method
FINE	–	Flow Integrated Environment
KS	–	Kero Start
LE	–	Leading Edge
NURBS	–	Non-Uniform Rational B-Spline
PS	–	Pressure Surface
SAAF	–	South African Air Force
SS	–	Suction Surface
STL	–	Stereo Lithography
TE	–	Trailing Edge

1.   Introduction

The Ballast project is a collaboration between the Counsil for Scientific and Industrial Research (CSIR), the South African Air Force (SAAF), the Armaments Corporation of South Africa (ARMSCOR) and the various universities within South Africa. This project, funded by the SAAF, involves the training of postgraduate students in the field of aerospace propulsion. Since its inception in 2010, the Ballast project has funded various research projects relating to the design and analysis of micro gas turbine engines. The present project focuses on the turbine stage of a micro jet engine. This thesis documents the research done into compiling a methodology for designing axial-flow turbines for micro jet engines.

1.1.   Background and motivation

The Department of Mechanical and Mechatronic Engineering at Stellenbosch University has been performing ongoing research in the field of small and micro gas turbine engines. Recent years have seen a number of postgraduate students completing projects in the design and analysis of jet engine components. The bulk of the research has revolved around improving the performance of small centrifugal compressors that are often used in micro gas turbine engines.

De Wet (2011) developed a method for analysing the performance of a diesel locomotive turbocharger compressor using one-dimensional theory based on the work of Aungier (2000). The results generated by this one-dimensional analysis method were compared to centrifugal compressor test cases found in literature. The comparison served to verify the accuracy of this one-dimensional method as a centrifugal compressor analysis tool.

Van der Merwe (2012) used the one-dimensional centrifugal compressor performance analysis program, developed by De Wet (2011), to design an impeller for a micro gas turbine compressor. This design was then optimised for certain pressure ratio, efficiency and mass flow rate targets using computational fluid dynamics (CFD). Finite element methods (FEM) were used to analyse the structure of this optimised compressor impeller design. The new impeller design was finally manufactured and tested using the turbocharger test bench developed as a postgraduate research project by Struwig (2012).

Krige (2012) focussed on the analysis and design of the radial diffuser for the centrifugal compressor of a micro jet engine. The performance of the radial diffuser in the Baird Micro Turbine 120 Kero Start (BMT 120 KS) micro turbojet engine was evaluated using CompAero, a commercial one-dimensional analysis

program based on the centrifugal compressor theory by Aungier (2000). The performance of the diffuser was also analysed using FINE Turbo, a commercial CFD package developed by Numeca International. A replacement radial diffuser for the BMT 120 KS compressor was designed and manufactured. The existing jet engine, fitted with the new radial diffuser, was also tested experimentally using a jet engine test bench that was constructed as part of the project.

The present project moves away from the study and development of centrifugal compressors and focuses on the analysis and development of axial-flow turbines found in micro jet engines. The goal of this project is the formulation of a methodology for designing axial-flow turbines for use in small jet engines. Such a design methodology must be able to generate a turbine design that conforms to the dimensional restrictions and performance requirements that prevail in a micro jet engine.

1.2.   Objectives

The primary purpose of this study is to formulate a methodology for designing axial-flow gas turbines for use in small jet engines. This is achieved through five secondary objectives.

The first objective is to obtain a baseline turbine design to which any new design can be compared. This design would have to be available in the different formats required for different types of analyses.

The second objective is to develop a method for generating a viable candidate (theoretical) turbine design for a given set of operational requirements. The method should then be used to design a replacement turbine for the baseline design obtained in meeting the first objective.

The third objective is to develop independent turbine performance analysis procedures that investigate the suitability of a given turbine design for certain operating conditions. Furthermore, a comparison of the results yielded by the different analyses procedures would serve to validate the procedures themselves.

The fourth objective is to investigate the structural integrity of any candidate design. Both the static and dynamic structural behaviour should be analysed to ensure the viability of a given turbine design.

The fifth objective is to prove the manufacturability of new candidate design. A manufacturing process, capable of producing prototypes of new turbine designs,

2

should be proposed. This process must then be implemented to create prototypes of the new turbine designs.

1.3.   Overview of the thesis

The presentation of the proposed design methodology is organised into six sections. These sections form Section 2 to Section 7 of this thesis.

The start of the design process is described in Section 2, where a reverse engineering process is used to generate a three-dimensional model of a turbine from an existing engine. The geometries of the turbine stator and rotor are digitised using respectively an X-ray computed tomography (CT) scanner and a coordinate measuring machine (CMM). The raw data from the measurement devices is then processed and reconstructed to yield three-dimensional models of the two components. These models will form the baseline turbine design to which any new designs could be compared.

In Section 3 a turbine performance analysis procedure that relies on an empirical loss model is introduced. The empirical loss model is used to estimate the relative total pressure loss coefficient of a blade row for given operating conditions. These estimated loss coefficients for the stator and rotor blade rows are used in through flow analyses to obtain the mass flow rates and the total-to-total efficiencies of a turbine design for a range of pressure ratios. Since the computational cost of obtaining the resulting turbine performance curves is low, this process is well suited to an iterative design process.

A process for designing a single stage axial-flow turbine for an existing jet engine is described in Section 4. This process involves determining the various performance parameters and using these parameters to generate a turbine design that would meet the requirements of the existing engine. The new turbine designs can then be subjected to the performance analysis procedure described in Section 3. Such a performance assessment would then suggest whether further investigation into each design is justified.

CFD performance analyses of the existing turbine and three new turbine designs are shown in Section 5. The CFD methodology is detailed and the performance analysis procedure is described. The results of the CFD performance analysis would serve two purposes. Firstly the CFD results for a turbine design provide a more accurate indication of the viability of that particular design. If the results of a CFD analysis were to suggest that a turbine design would not perform adequately, the analysis of such a design would not be pursued further. Secondly,

the CFD results of a turbine design can be compared to the corresponding results of the performance analysis described in Section 3. Such a comparison could lead to valuable insights into the validity of the two performance analysis tools.

In Section 6 the static structural and modal analyses of the existing turbine rotor and the rotors of the three new designs are described. The FEM modelling is detailed and the analysis methods are described. The static structural analysis allows the structural integrity of the different turbine designs to be examined at the operating conditions. The modal analysis enables the natural frequencies of each turbine blade design to be compared to the excitation frequencies present at any given rotational speed. Such a comparison is necessary for avoiding structural resonance.

Section 7 documents the process followed to create the prototypes of the turbine components. Firstly, the appropriate material for the prototypes is chosen, thus enabling appropriate manufacturing processes to be specified. Three-dimensional models of the desired final geometries are then generated and adapted as necessitated by the chosen manufacturing processes. Finally, the results of the different manufacturing processes can be compared.

Section 8 contains an overview of the results found in the preceding sections and some concluding remarks.

1.4.   A note on turbine blade and flow angle conventions

An angle convention is required when describing the flow field and blade geometry of a turbo-machine. However, there is little standardization of flow angle conventions in literature. Some authors use a plane through the axis of the machine as the reference from where flow and blade angles are measured and others measure the angles from the circumferential direction. Furthermore, different authors differ in how the sign of a given angle is defined.

For the present design process an angle convention is defined that is consistent for blade and flow field angles. All angles are measured from the axial direction and are defined as positive in the direction of machine rotation. Figure 1-1 shows this angle convention as applied to both the absolute and relative flow field angles, α and α' respectively, and the blade angles, β, for a single stage axial-flow turbine. Negative angles are shown by dotted line arrows.

4
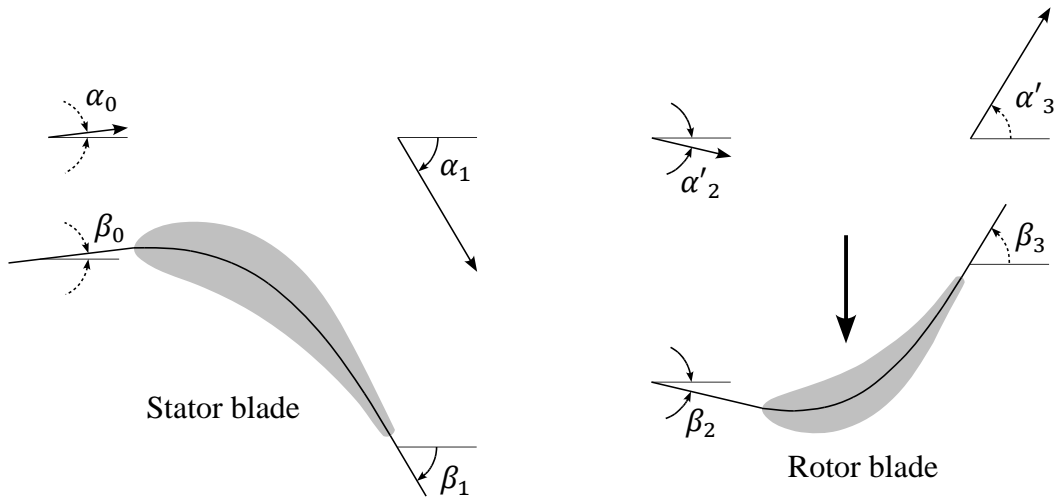
Figure 1-1: Consistent blade and flow angle convention

Despite the author's attempt to use only one angle convention, a generic blade angle convention is also used due to its compatibility with certain published empirical correlations. In this generic blade convention angles are measured from the circumferential direction and always from the pressure, or concave, side of the blade. This convention is shown in Figure 1-2 as it is applied to the same axial-flow turbine stage shown in Figure 1-1. As shown in Figure 1-2 all the angles are defined positive, so one can't deduce whether a blade is a rotor or a stator blade by observing the angle signs.
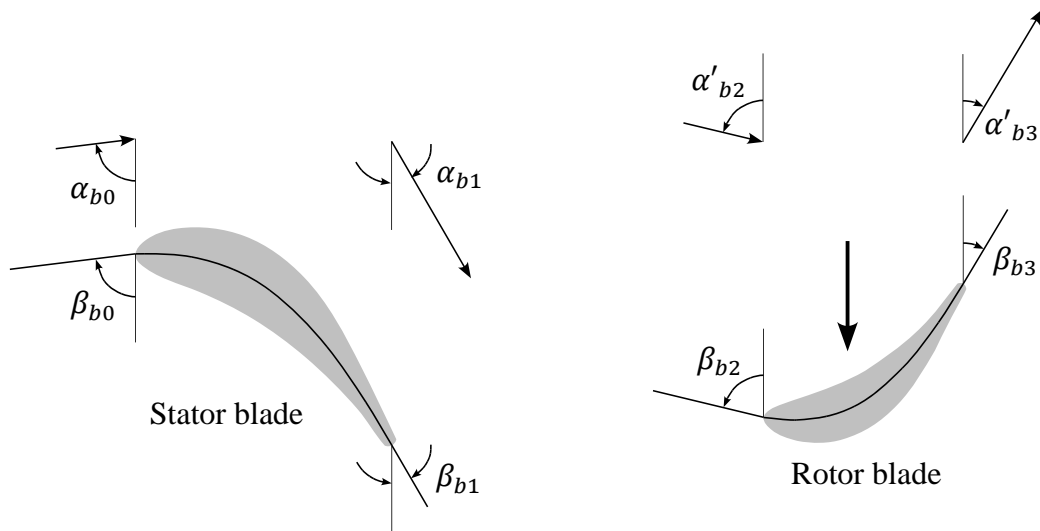
Figure 1-2: Generic blade angle convention

The translation between the consistent convention and the generic blade angle conventions for a turbine stage is shown is equations (1.1) through (1.4). This translation is shown only for the blade angles, but it also applies to the absolute and relative flow field angles.

$$\beta_{b0} = 90° + \beta_0 \tag{1.1}$$

$$\beta_{b1} = 90° - \beta_1 \tag{1.2}$$

$$\beta_{b2} = 90° - \beta_2 \tag{1.3}$$

$$\beta_{b3} = 90° + \beta_3 \tag{1.4}$$

2.   Reverse engineering an existing turbine

2.1.   Introduction

This section describes how the geometries of the stator and the rotor wheels of the BMT 120 KS engine are digitized as part of a process known as reverse engineering. Reverse engineering allows structural and performance analyses to be performed on the components of an existing turbine stage. The results of these analyses are then used as a baseline to which the performance of any new turbine stage design is compared. Reverse engineering is widely recognised as an essential step in the design cycle (Chen & Lin, 2000).

The rotor wheel has two complex geometrical features that require high resolution sampling: the axisymmetric hub profile and the radially varying blade profile. These two features are digitized by using a three-dimensional coordinate measuring machine (CMM) to record traces of points along the aforementioned profiles.

The stator wheel also has complex blade profiles, but the hub and shroud profiles are simple cylindrical surfaces that can be defined by a small number of easily measured variables. Therefore only the blades of the stator wheel need to be sampled at a high resolution. An X-ray computed tomography (CT) scanner is used to create a point cloud of the stator wheel, since the shroud restricts the physical access to the blades for profile measuring.

The digitisations of the turbine components as they are collected from the measurement instruments are in a point cloud format. These point clouds are processed to yield usable geometries of the physical features they represent. Finally the processed geometric information is compiled into complete three-dimensional models of the turbine components.

2.2.   Component point cloud extraction

2.2.1. Obtaining turbine rotor point cloud data using a CMM

A *Mitutoyo Bright STRATO 710* coordinate measuring machine (CMM), shown in Figure 2-1, is used to generate the turbine rotor point cloud. CMMs have the ability to measure the coordinates of points on the surface of an object very accurately and are well suited to measuring the complex shapes found in turbine blades (Junhui, et al., 2010). The present CMM has a precision ground granite table to serve as a flat reference surface to which the measured object is secured. The granite table top also has various mounting holes that accept auxiliary

precision machined mounting blocks. These blocks provide additional configuration options when mounting an object.

Figure 2-1: *Mitutoyo Bright Apex 710*

The measurements are made using a contact sensitive computer numerically controlled (CNC) probe. The end of the probe is equipped with a stylus consisting of a metal stem with a spherical ball at its tip. The probe is moved in the vicinity of the object and the coordinates of the end-ball are recorded whenever contact with the object is made.

The radius of the end-ball imposes a constraint on the minimum radius of curvature that can be perceived by the CMM. Clearly the CMM cannot detect a concave curve that has a radius of less than the radius of the probe end-ball. However, using a larger ball increases the reach of the probe when measuring surfaces under overhanging features like curved turbine blades.

The machine set-up and part configuration
The turbine rotor wheel is temporarily glued to a mounting block that is in turn attached to the CMM table. This use of a mounting block allows the turbine rotor to be secured with its rotational axis parallel to the table and one of the blades pointing directly upward. The configuration of the turbine rotor is shown in Figure 2-2 where the illustrations of the turbine rotor wheel, the mounting block

8

and the granite table of the CMM can be seen. This configuration permits the CMM probe to record the coordinates of a large number of points along the blade profile at a fixed height above the table. Additionally, this setup allows the probe unobstructed access to one side of the hub of the turbine rotor wheel.
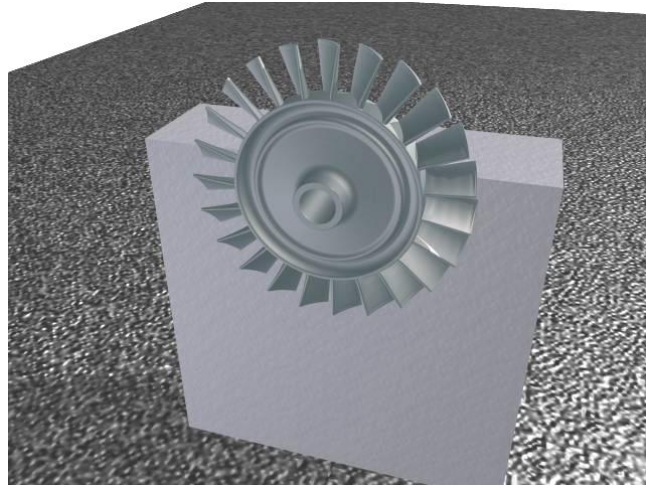
Figure 2-2: CMM turbine rotor configuration

The measurement paths

Rotor blade profile
The variation of the turbine rotor blade profile from its root to its tip is digitised by recording point traces at different radial positions along the blade length. The CMM probe is constrained to a height above the table slightly below the tip of the upward facing turbine blade. The probe then follows a path along the blade surface at that height and records the coordinates of the points where the end-ball contacts the surface. This process is repeated a number of times with the fixed height being moved downwards incrementally. The lowest possible fixed height is slightly above the blade root since the hub of the turbine rotor would interfere with the path of the probe. This process yields blade profile data that ranges from slightly below the blade tip to slightly above the blade root.

Rotor hub profile
The rotor hub contour is digitised by recording a point trace starting in the centre of the shaft hole and moving radially outwards. This is accomplished by keeping the probe at a fixed height and allowing it to follow the hub profile until it reaches the blade root.

Figure 2-3 shows the paths followed by the CMM probe as black lines. It can be seen that the blade profile is sampled at six locations and the trace along the hub profile is also visible.

Figure 2-3: CMM measurement paths on the turbine rotor wheel

2.2.2. Obtaining turbine stator wheel point cloud data from CT-scanner data

X-ray computed tomography (CT) scanners can produce a three-dimensional point cloud of an object by integrating information from different X-ray images of the object. A high-resolution CT-scanner, the *Phoenix v|tome|x m* shown in Figure 2-4 on the next page, is used to create a three-dimensional point cloud of the turbine stator wheel.

The CT-scanner software outputs the point cloud data in a stereo lithography (STL) file format. This file is not a solid model, but rather a collection of point coordinates. It is however possible to draw surfaces between all sufficiently close neighbouring points in order to visualise the CT-scanner output. Such visualisations of the front and back views of the stator wheel point cloud are shown in Figure 2-5 on the next page. These visualisations can be used to assess the quality of the geometric reproduction produced by the CT-scanner.

Figure 2-4: *Phoenix v/tome/x m* high resolution CT-scanner

Front view   Back view
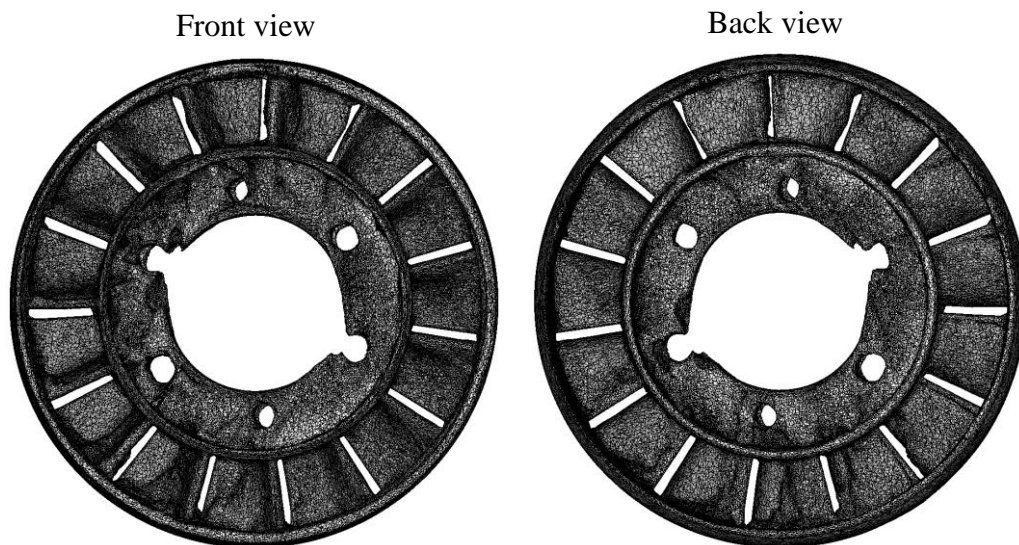
Figure 2-5: Surface visualization of STL-file produced by the CT-scanner

Referring to Figure 2-5, it can be seen that the CT process results in a model with feature reproduction in some areas. This geometrical distortion is most apparent near the mounting holes of the stator wheel, but is also visible on most of the blades.

11

The software of a CT-scanner uses the physical properties of the object material in translating the input signal from its X-ray detector into meaningful geometries. Therefore a possible reason for the lack in model quality is the presence of foreign material deposits on the turbine stator wheel during the scanning process. Such deposits are likely to have accumulated, due the present stator wheel operating in a working micro gas turbine engine. During high temperature operation both the locking compound used on the mounting holes and the incomplete combustion process close to the blades leave a residue. For the present case the areas affected by geometric distortion coincide with the areas where contaminant residue is found. Therefore the presence of the residue is deemed a plausible explanation for the geometric distortion.

Fortunately one of the stator blades is unaffected by the geometrical distortion along most of its span. This undistorted blade enables the extraction of the stator blade profile data from the CT-scanner generated point-cloud. Furthermore, the badly distorted mounting hole geometry is not critical to the performance analysis of the turbine. Therefore the CT-scanner produced usable data for the reverse engineering process.

2.3.   Processing raw point coordinate data

2.3.1. Curve smoothing

The CMM yields the coordinates of discrete points on the surfaces of the turbine rotor blade wheel hub. Due to the small size of these features and the roughness of these surfaces the resulting collections of points contain a certain amount of noise. Therefore, non-uniform rational B-spline (NURBS) curves are fitted through each collection of points in order to obtain smooth profile curves for both the rotor blades and rotor wheel hub. These NURBS curves provide a curve that is an appropriate average of the measured points.

Similarly, the point cloud model of the stator wheel generated by the CT-scanner is also geometrically noisy. Parametric surfaces are therefore fitted through the points in the vicinity of the surface of the least distorted blade portion. These surfaces are constrained to be continuous in curvature and wrap all the way around the central part of the blade span. Slices are then made through the surfaces to obtain smooth blade profile curves.

2.3.2. Blade profile extrapolation

During measurement operations, it is not possible to obtain accurate measurements of points on the edges of an object (Chivate & Jablokow, 1995). Therefore, for both the turbine rotor and the stator, smoothed blade profile curves

only cover the central portion of the blade span. However, the complete three-dimensional reconstructions of the blades require blade profiles that include the root and tip sections. Since these additional profile curves could not be measured, linear extrapolations of the blade profiles are performed.

The blade profile curves are each divided into four curve sections according to local radius of curvature. These sections relate to the blade leading edge (LE), trailing edge (TE), pressure surface (PS) and suction surface (SS) respectively. Dividing the turbine profile into these functional regions strongly improves the accuracy with which the geometry can be recreated (Mohaghegh, et al., 2006). Figure 2-6 shows one such blade section division where the four different sections are identified. The leading and trailing edge curves can be seen to have small curvature radii compared to those of the pressure and suction surface curves.
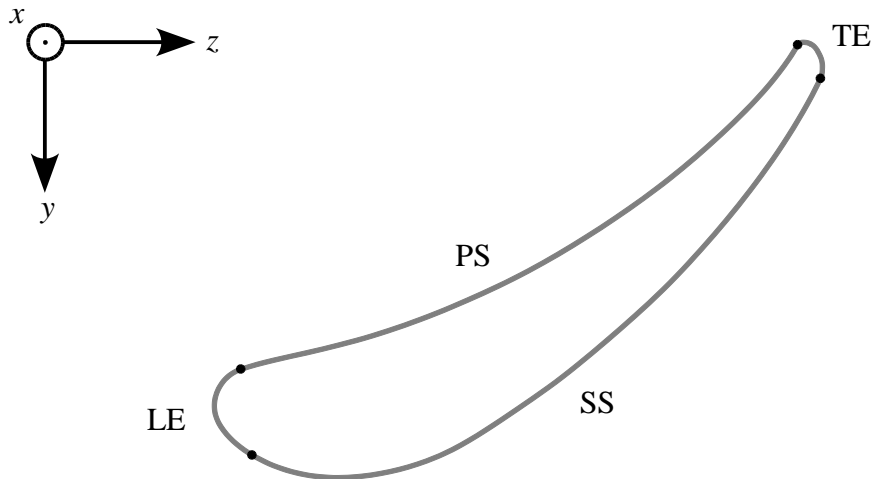
Figure 2-6: Blade profile curve section divisions

The leading edge curve section of each blade profile curve is sampled at a fixed number of evenly distributed points as shown in Figure 2-7. This is done to relate each point on the leading edge curve of one blade profile curve to a corresponding point on the leading edge curve of every other profile curve. This process is repeated for the remaining three curve sections of each blade profile curve to yield a set of consistently sampled profile curves.

13
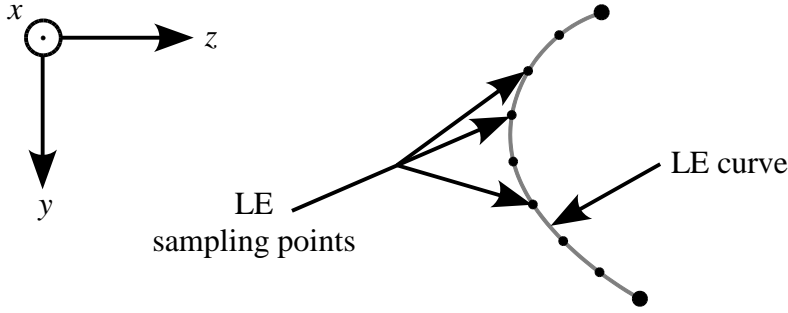
Figure 2-7: LE curve section point sampling

Given that the each of the n profile curves has k consistently sampled points, the point data can now be represented as point i on profile j, or symbolically as

$$\boldsymbol{p}_{i,j} = \begin{Bmatrix} x_i \\ y_i \\ z_i \end{Bmatrix}_j, \qquad i \in [1,k], \qquad j \in [1,n]. \tag{2.1}$$

A linear regression can now be done for each set of n corresponding points on the different blade profile curves. The linear trend line is calculated using the least squares criterion and using the radius about the turbine rotational axis as the independent variable. The radius of each point is given by

$$r_{i,j} = \sqrt{x_{i,j}^2 + y_{i,j}^2}. \tag{2.2}$$

The three-dimensional line is represented by three parametric equations: one for the x-direction, one for the y-direction, and one for the z-direction. These parametric equations are of the form:

$$\boldsymbol{p}_i(r) = \boldsymbol{m}_i r + \boldsymbol{c}_i, \qquad \boldsymbol{m}_i = \begin{Bmatrix} m_x \\ m_y \\ m_z \end{Bmatrix}_i, \qquad \boldsymbol{c}_i = \begin{Bmatrix} c_x \\ c_y \\ c_z \end{Bmatrix}_i. \tag{2.3}$$

The total squared error of each linear approximation, $\boldsymbol{E}_i$, is

$$\boldsymbol{E}_i = \begin{Bmatrix} E_x \\ E_y \\ E_z \end{Bmatrix}_i = \sum_{j=1}^{n} \begin{Bmatrix} [(m_{x,i} r_{i,j} + c_{x,i}) - x_{i,j}]^2 \\ [(m_{y,i} r_{i,j} + c_{y,i}) - y_{i,j}]^2 \\ [(m_{z,i} r_{i,j} + c_{z,i}) - z_{i,j}]^2 \end{Bmatrix}. \tag{2.4}$$

The values of the parametric equation coefficients, $\boldsymbol{m}_i$ and $\boldsymbol{c}_i$, are found by first partially differentiating the error function with respect to each coefficient. The procedure is only shown for the x-component of the parametric equation, but the formulation is identical for the y-component and z-component.

14

$$\frac{\partial E_{x,i}}{\partial m_{x,i}} = \sum_{j=1}^{n}\left(2m_{x,i}r_{i,j}^2 + 2c_{x,i}r_{i,j} - 2x_{i,j}r_{i,j}\right) \tag{2.5}$$

$$\frac{\partial E_{x,i}}{\partial m_{x,i}} = \sum_{j=1}^{n}\left(2m_{x,i}r_{i,j} + 2c_{x,i} - 2x_{i,j}\right) \tag{2.6}$$

These derivatives are then equated to zero, thus resulting in a system of linear equations. The system is written in matrix form and solved by inversion:

$$\begin{bmatrix} \sum r_{i,j}^2 & \sum r_{i,j} \\ \sum r_{i,j} & n \end{bmatrix}\begin{Bmatrix} m_{x,i} \\ c_{x,i} \end{Bmatrix} = \begin{Bmatrix} \sum r_{i,j}x_{i,j} \\ \sum x_{i,j} \end{Bmatrix} \tag{2.7}$$

$$\begin{Bmatrix} m_{x,i} \\ c_{x,i} \end{Bmatrix} = \begin{bmatrix} \sum r_{i,j}^2 & \sum r_{i,j} \\ \sum r_{i,j} & n \end{bmatrix}^{-1}\begin{Bmatrix} \sum r_{i,j}x_{i,j} \\ \sum x_{i,j} \end{Bmatrix} \tag{2.8}$$

Therefore there exist three linear systems for each of the k consistently sampled profile points. Once all the systems are solved the blade can be defined as a function of radius, using the resulting parametric equations. These equations are then used to generate blade profile points that range from the blade root to the blade tip.

2.4.   Three-dimensional model reconstruction

Once the blade profiles are available for the whole length of the blades, these profiles are imported into a CAD package. In the CAD package a surface loft is performed on the profiles, yielding the blade surfaces. These blade surfaces provide sufficient geometrical data to perform CFD and empirical model based performance analyses.

The aim is however to generate full three-dimensional models of the two turbine components. To achieve this, the hubs of the turbine rotor and the stator, and the shroud of the latter must be modelled. The hub profile of the rotor wheel is available, since it was digitised along with its blade profiles. The hub and shroud profiles of the stator wheel are much simpler geometries and easily obtained using a vernier calliper. These profiles are then revolved around the turbine axis of rotation to obtain solid models of the rotor hub and the stator hub and shroud.

Finally, the blade surfaces are mated to their respective hub and shroud surfaces to complete the three-dimensional component models. Fillet radii are applied where the blades meet the hub or shroud surfaces and the blades are patterned circularly around the axis of the turbine for the correct number of blades. Figure 2-8 shows

the resulting three-dimensional models of the turbine stator (left) and the rotor (right).
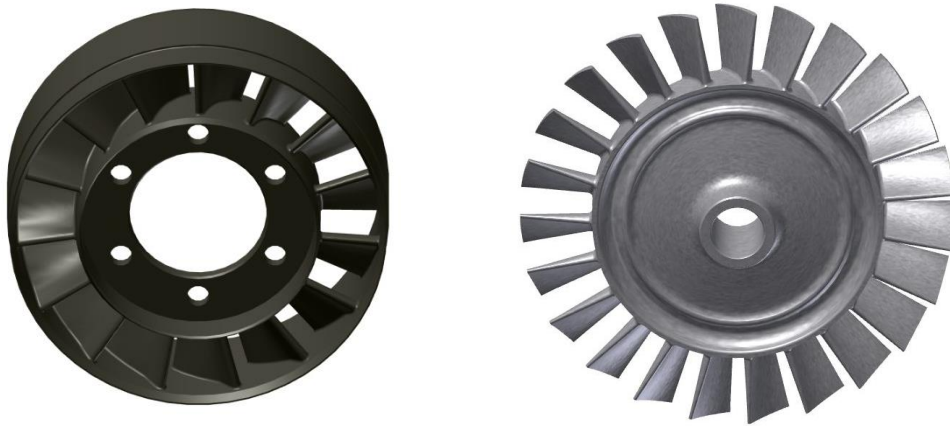
Figure 2-8: Three-dimensional turbine stator and rotor wheel reconstructions

2.5. Conclusion

This section presented the process followed in reverse engineering the turbine components found in the BMT 120 KS micro jet engine. The turbine rotor was digitised using a CMM and the turbine stator was digitised using a CT-scanner. The raw point cloud data generated by the two measurement devices was processes to allow for the reconstruction of full three-dimensional models of the two turbine components.

3.   Performance analysis using an empirical loss model

3.1.   Introduction

Turbine performance analyses are required during the design process to ensure the viability of any given combination of design parameters. Clearly, the most accurate method for analysing a turbine design is to build a prototype and perform a full experimental test. Such a method is essential in the final design stage, but its high cost and long lead times make it impractical during the early design stage. An alternative performance analysis method that can yield highly accurate results is a full three-dimensional computational fluid dynamics (CFD) analysis. These analyses are less expensive and less time consuming than experimental testing. However, the set-up and run time of such an analysis is too long for the rapid evaluation of many different designs. Therefore a low-cost and less time consuming analysis method is required. An empirical loss model can be incorporated into a one-dimensional mean-radius performance analysis system that is both low-cost and has a negligible run time.

In a one-dimensional mean-radius performance analysis system the gas states and velocities are calculated throughout the turbine stage using isentropic thermodynamic relationships. The entropy generation losses in the turbine stage are then accounted for by means of empirical correlations.

3.2.   Empirical loss model

The use of an empirical loss model is an attempt to assess the performance of a turbine blade row without actually testing or simulating it. In the absence of actual test data for a given design, the effects of different design parameters on the performance of previously tested turbine designs are correlated. These empirical correlations are then used to estimate the effects of each design parameter on the untested design.

In an adiabatic blade row, the entropy generation is linearly dependent on the total pressure loss through the blade row (De la Calzada, 2011). Therefore, the empirical loss model proposed by Ainley and Matthieson (1951) predicts the effect different design parameters have on the total pressure loss across a given blade row. This loss in total pressure is accounted for by a total pressure loss coefficient. The total pressure loss coefficient of a blade row, $Y,$ is defined as the ratio of the loss of relative total pressure across the blade row to the dynamic pressure at the exit of the blade row. This definition is shown symbolically in equation (3.1).

$$Y = \frac{p'_{t0} - p'_{t1}}{p'_{t1} - p_1} \tag{3.1}$$

The present loss model calculates the value of Y by estimating and summing the effects of five different sources of irreversibility present in the blade row. These sources are the blade profile loss (Y_p), secondary flow loss (Y_s), tip clearance loss (Y_{CL}), the non-zero blade trailing edge thickness loss (Y_{TE}), and the loss caused by the formation of shock waves (Y_{SH}). Therefore the present total pressure loss model can be expressed as:

$$Y = Y_{TE} + Y_p + Y_s + Y_{CL} + Y_{SH}. \tag{3.2}$$

3.2.1. Loss model parameters

The loss model predicts the performance by estimating the contribution of different design parameters to the overall total pressure loss of a blade row. These parameters are listed in Table 3-1.

Table 3-1: Empirical performance model inlet parameters

Blade parameters		Flow field parameters	
β_{b0}	Inlet blade angle	α'_{b0}	Relative inlet angle
β_g	Gauge angle	α'_{b1}	Relative exit angle
b_z	Axial chord	W_1	Relative exit velocity
c	Chord	M'_0	Relative inlet Mach number
s	Mean radius blade pitch	M'_1	Relative exit Mach number
s/c	Pitch-to-chord ratio	ρ_1	Exit density
R_c	Uncovered turning radius	μ_1	Exit dynamic viscosity
t_{max}	Maximum thickness		
t_{TE}	Trailing edge thickness		
e	Surface roughness height		
H	Height		
δ	Tip clearance		

The blade height, tip clearance and surface roughness height all have unambiguous meanings, and so do the relative Mach numbers and thermodynamic properties of the flow field. The rest of the parameters are defined in Figure 3-1 where the profiles of two neighbouring blades are shown. As can be seen in Figure 3-1, the blade gauge angle is the angle measured from the tangent to the suction side of the blade between its trailing edge and the throat to the circumferential direction. This angle can fairly easily be measured by hand using an appropriately sized mitre gauge.

18
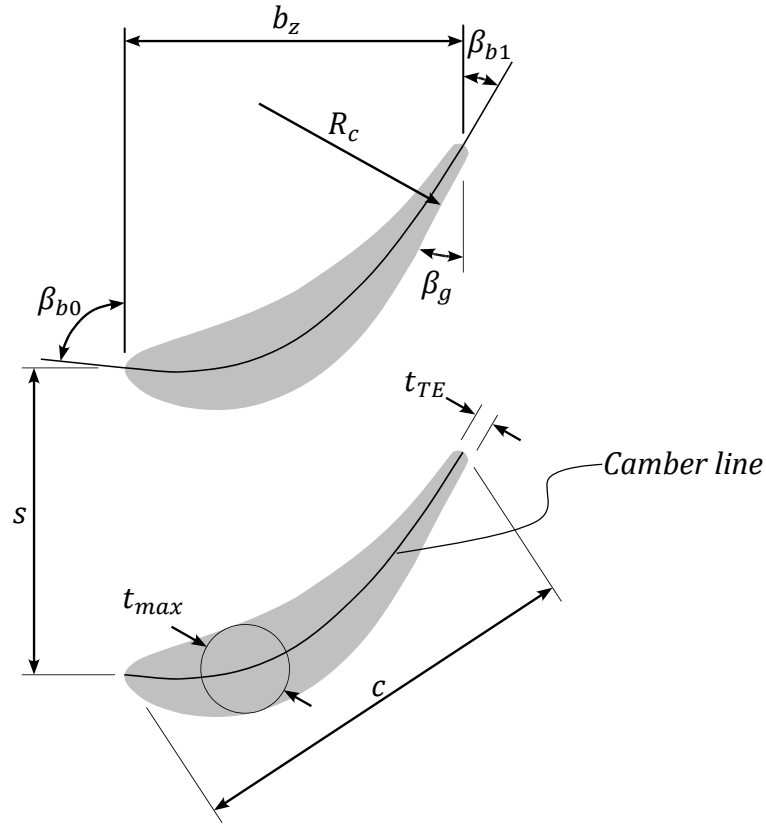
Figure 3-1: Blade and flow field parameters

3.2.2. Trailing edge loss coefficient

The finite trailing edge thicknesses of turbine blades cause the flow to separate from the blade at two separate points: one on each side of the blade. The present model proposed by Aungier (2006) treats the effects of this flow separation as a sudden flow area enlargement, resulting in the expression for the trailing edge loss coefficient shown in equation (3.3).

$$Y_{TE} = \left(\frac{t_{TE}}{s \sin \beta_g - t_{TE}} \right)^2 \tag{3.3}$$

3.2.3. Profile loss coefficient

The profile loss coefficient is influenced by a number of different factors and defined by Equation (4-21) on page 69 in Aungier (2006),

$$Y_p = K_{mod} K_{inc} K_M K_p K_{RE} \left(\left(Y_{p1} + \xi^2 \left(Y_{p2} - Y_{p1} \right) \right) \left(5 \frac{t_{max}}{c} \right)^\xi - \Delta Y_{TE} \right). \tag{3.4}$$

19

This expression consists of a base profile loss coefficient, $Y_{p1} + \xi^2(Y_{p2} - Y_{p1})$, and a number of modification factors and terms. The different factors in the profile loss coefficient expression are now identified and defined.

Nozzle blade and impulse blade profile loss coefficients, Y_{p1} and Y_{p2}

The base profile loss coefficient of an airfoil is calculated by interpolating between the coefficients for a pure nozzle blade and an impulse blade of the same exit angle. The term "pure nozzle blade" used here refers to a blade with an inlet angle of $\beta_{0b} = 90°$. The gas deflection ratio, ξ, is used in the interpolation calculation and defined as the ratio of the inlet blade angle to the exit flow angle:

$$\xi = \frac{90° - \beta_{b0}}{90° - \alpha'_{b1}}. \tag{3.5}$$

Both the nozzle blade and the impulse blade profile loss coefficients are functions of the relative outlet flow angle and the difference between the actual and optimum pitch-to-chord ratios. The optimum pitch-to-chord ratios for nozzle blades and impulse blades according to Aungier (2006) are shown in Figure 3-2 for a range of possible relative exit flow angles. The equations for calculating the optimum nozzle blade and impulse blade pitch-to-chord ratios are shown in Appendix A.1.2 as equations (A-5) and (A-6) respectively.
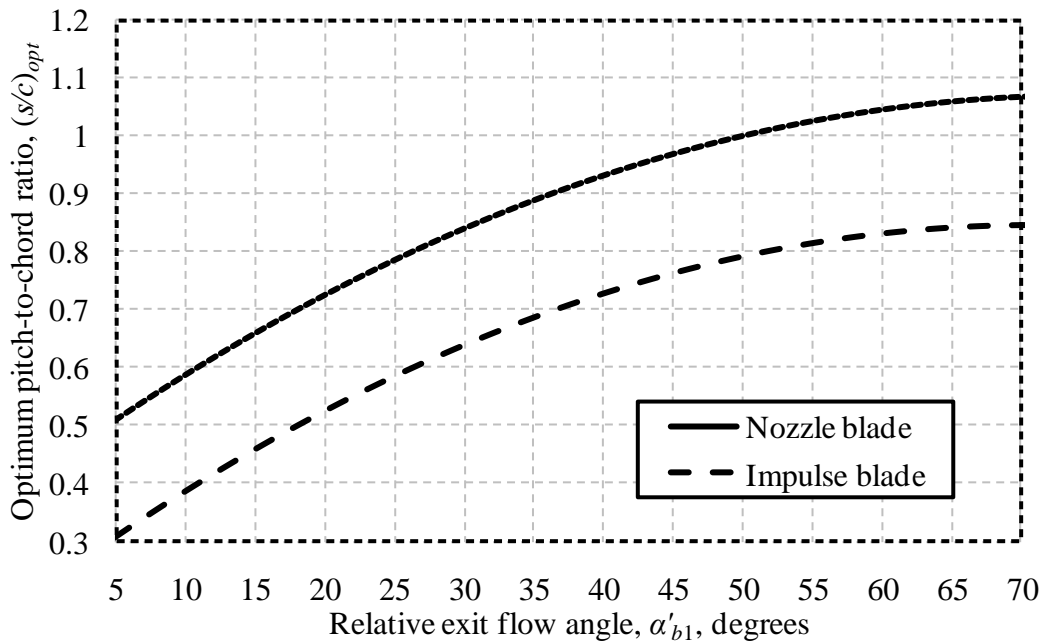
Figure 3-2: Optimum pitch-to-chord ratios for nozzle and impulse blades according to Aungier's (2006) correlation

20

The nozzle blade profile loss coefficient, Y_{p1}, is a function of the exit blade angle and the difference between the actual and the optimal nozzle blade pitch-to-chord ratios. Y_{p1} is calculated using equations (A-7) to (A-12) in Appendix A.1.2. Similarly, the impulse blade profile loss coefficient, Y_{p2}, is a function of the exit blade angle and the difference between the actual and the optimal impulse blade pitch-to-chord ratios. Y_{p2} is calculated using equations (A-13) to (A-17) in Appendix A.1.2. These nozzle blade and impulse blade profile loss coefficients according to Aungier (2006) are shown in Figure 3-3 and Figure 3-4 respectively for different pitch-to-chord ratios and different relative exit flow angles.
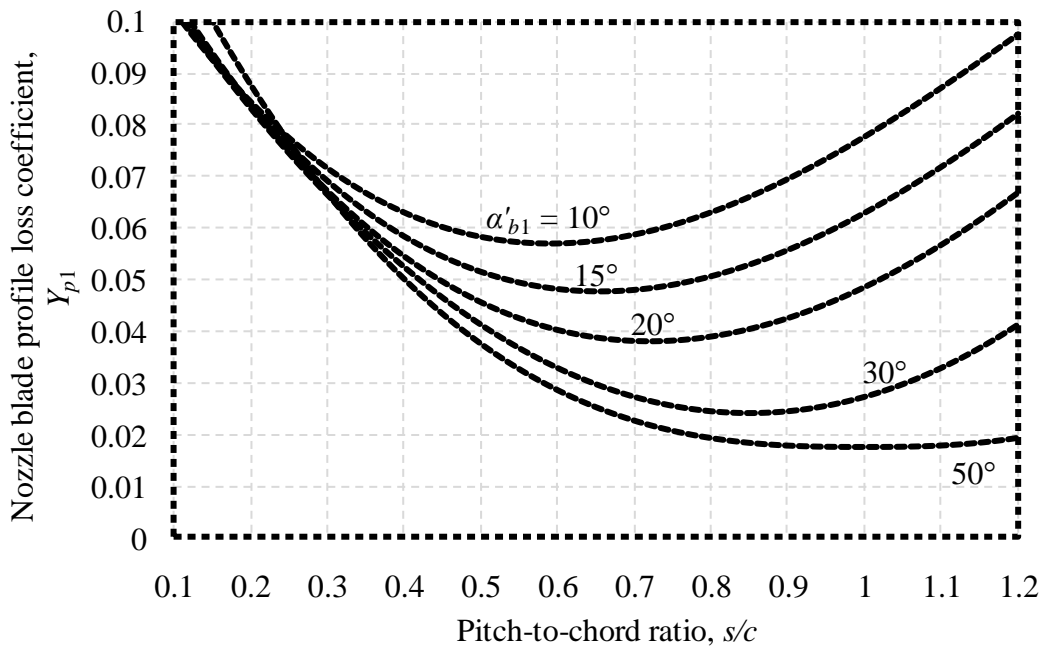
Figure 3-3: Profile loss coefficient for nozzle blades, adapted from Aungier (2006)

Modification factor for modern blade designs

The modification factor for modern blade designs, K_{mod}, is suggested by Kacker and Okapuu (1982) to take the advances in modern blade design into account when predicting the profile loss coefficient of a blade row. It assumes a reduction in profile loss ranging from 33 % for highly optimized designs to 0 % for old non-optimised designs. For the present case the blade design is not formally optimised. Consequently it is treated as an older design and the modification factor assumes a value of unity.

$$K_{mod} = 1. \tag{3.6}$$

21
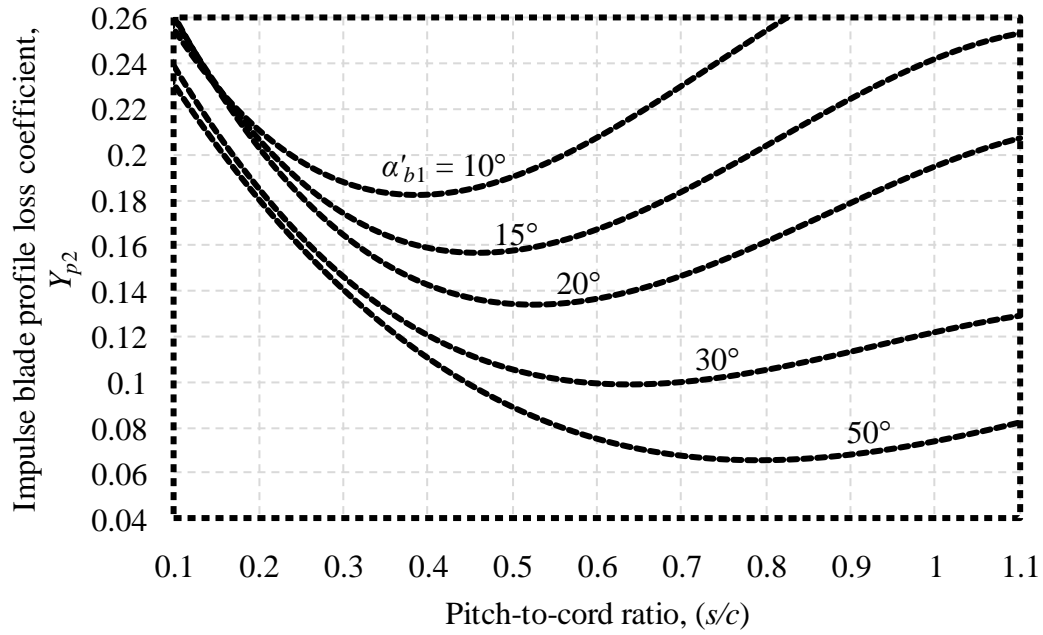
Figure 3-4: Profile loss coefficient for impulse blades, adapted from Aungier (2006)Off-design incidence correction factor

The off-design incidence correction factor, K_{inc}, takes account of the difference between the inlet blade angle and the relative inlet flow angle, or incidence angle, during off-design operation. The incidence angle at any operating condition is given by

$$i = \beta_{b0} - \alpha'_{b0}. \tag{3.7}$$

The amount of correction required depends on the ratio of the actual incidence angle to the incidence angle that would induce blade stall. An empirical correlation is employed to predict the stalling incidence angle. The stalling incidence angle correlation is built up from a gas deflection ratio dependent part, i_{sr}, and a blade pitch-to-chord ratio dependent stalling incidence angle correction, Δi_s.

$$i_s = i_{sr} + \Delta i_s \tag{3.8}$$

The gas deflection ratio dependent part of the stalling incidence angle is also a function of the relative gas exit angle. The interrelationship between these three variables as modelled by Aungier (2006) is shown in Figure 3-5. In Figure 3-5 the gas deflection ratio dependent part of the stalling incidence angle is shown for six different relative exit flow angles. The equations used to model the gas deflection ratio dependent part of the stalling incidence angle are shown in Appendix A.1.2 as equations (A-19) to (A-24).
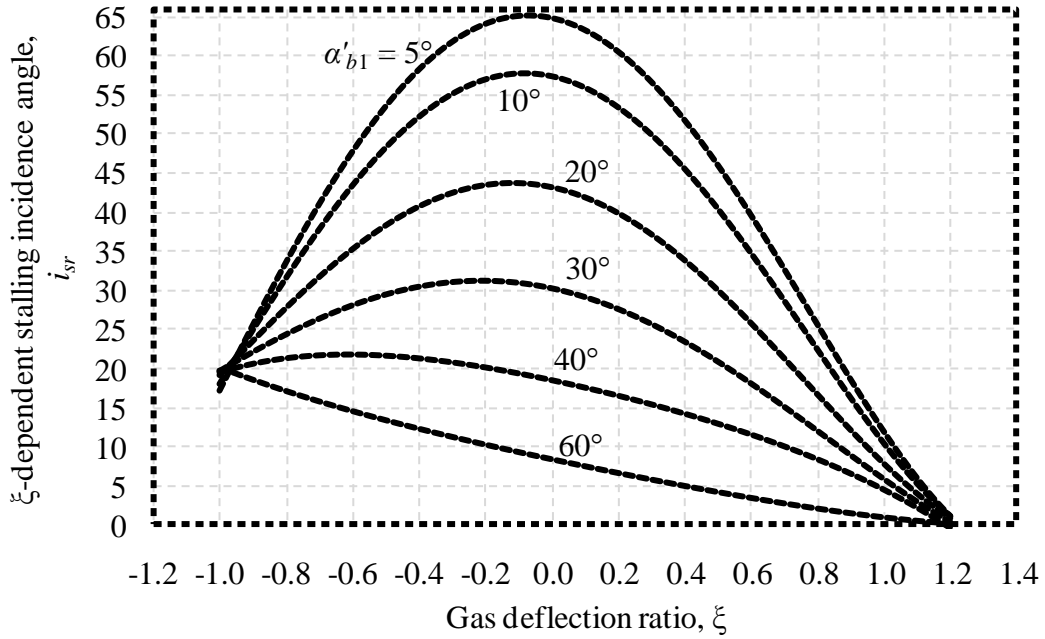
Figure 3-5: Gas deflection ratio dependent stalling incidence angle term, adapted from Aungier (2006)

The pitch-to-chord ratio dependent stalling incidence angle correction is calculated using equations (3.9) and (3.10), and is shown in Figure 3-6 for three different relative exit flow angles. (Aungier, 2006)

$$X_{is} = s/c - 0.75 \tag{3.9}$$

$$\Delta i_s = \begin{cases} -38°X_{is} - 53.5°X_{is}^2 - 29°X_{is}^3, & s/c \leq 0.8 \\ -2.0374° - (s/c - 0.8)\left[69.58° - 1°\left(\dfrac{\alpha'_{b1}}{14.48°}\right)^{3.1}\right], & s/c > 0.8 \end{cases} \tag{3.10}$$

Finally, the off-design incidence correction factor is calculated using equation (3.11)**Error! Reference source not found.** and is shown in Figure 3-7 for a range of different actual-to-stalling incidence angle ratios.

$$K_{inc} = \begin{cases} -1.39214 - 1.90738(i/i_s), & (i/i_s) < -3 \\ 1 + 0.52(i/i_s)^{1.7}, & -3 \leq (i/i_s) < 0 \\ 1 + (i/i_s)^{2.3+0.5(i/i_s)}, & 0 \leq (i/i_s) < 1.7 \\ 6.23 - 9.8577[(i/i_s) - 1.7], & 1.7 \leq (i/i_s) \end{cases} \tag{3.11}$$

23
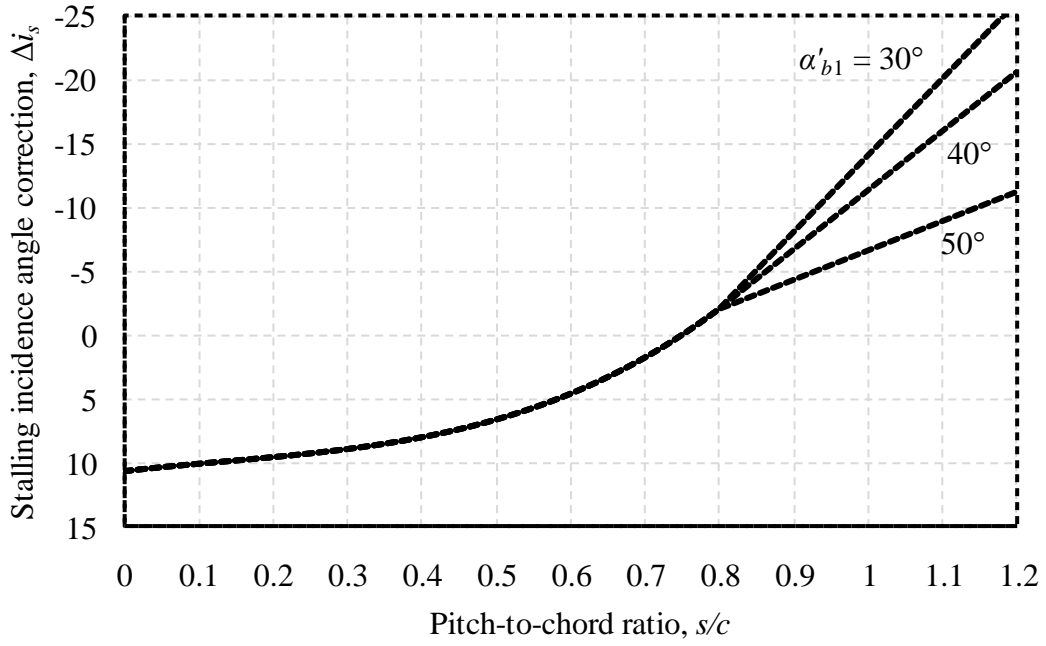
Figure 3-6: Pitch-to-chord ratio dependent stalling incidence angle correction, adapted from Aungier (2006)
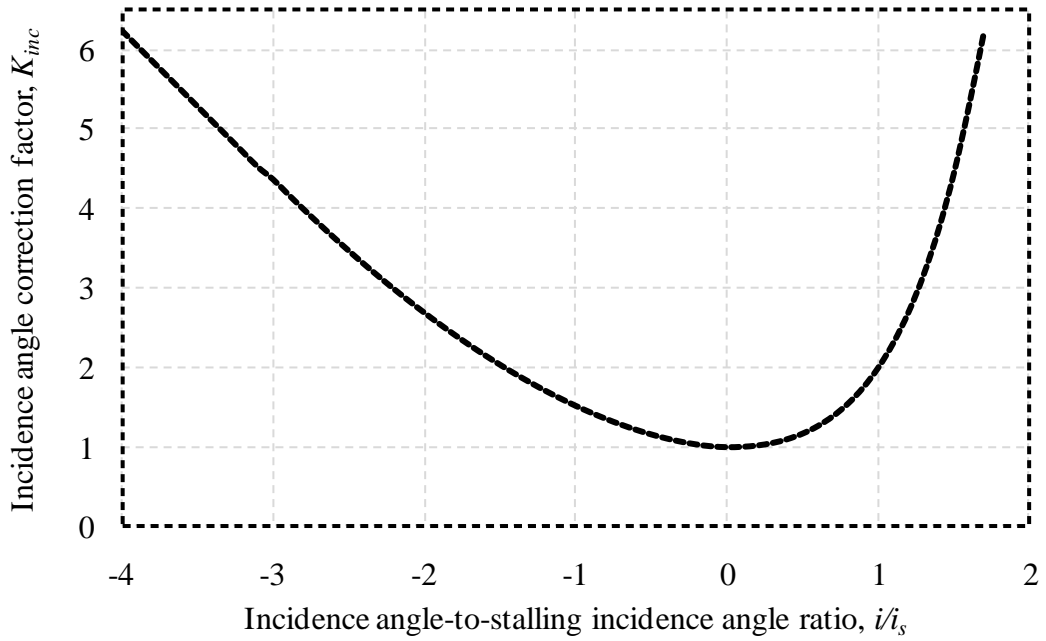
Figure 3-7: Off-design incidence angle correction factor, adapted from Aungier (2006)

24

Mach number correction factor

K_M is a correction factor that is dependent on the relative exit flow Mach number of the blade row. It is based on the graphical data published by Ainley and Mathieson (1951) and takes the form of an empirical correlation. The correlation, proposed by Aungier (2006), closely approximates the graphical data and is shown in symbolic form in equation (3.12).

$$K_M = 1 + [1.65(M_1' - 0.6) + 240(M_1' - 0.6)^4]\left(\frac{s}{R_c}\right)^{3M_1'-0.6} \tag{3.12}$$

Equation (3.12) is applicable when the relative exit flow Mach number is between 0.6 and 1. For Mach number values outside of this range K_M assumes a value of unity. For Mach numbers of 0.6 or less no correction factor is required; and for Mach numbers of 1 or more the correction is made with a different factor.

Compressibility correction factor, K_p

Turbines experience higher Mach number flows during operation than can be obtained in low speed cascade testing. The compressibility accompanying these higher Mach numbers lead to thinner boundary layers and a decreased likelihood of flow separation (Japikse & Baines, 1994). These two effects serve to decrease the profile loss below the value predicted by a loss model based solely on cascade testing. Therefore K_p is included in this loss model to take account of these benefits of the higher Mach number flow conditions present in actual turbine operation.

Kacker and Okapuu (1982) originally suggested a correction factor based on the relative inlet and outlet Mach numbers of a blade row. This formulation can however result in negative profile loss coefficients for certain unlikely relative inlet and outlet Mach number combinations. Therefore Aungier (2006) proposes a revision of the Kacker and Okapuu formulation that limits K_p to values greater than about 0.5. The revised formulation used in the present loss model is (Aungier, 2006):

$$\widetilde{M}_0' = 0.5(M_0' + 0.566 - |0.566 - M_0'|) \tag{3.13}$$

$$\widetilde{M}_1' = 0.5(M_1' + 1 - |M_1' - 1|) \tag{3.14}$$

$$X_p = \frac{2\widetilde{M}_0'}{\widetilde{M}_0' + \widetilde{M}_1' + |\widetilde{M}_1' - \widetilde{M}_0'|} \tag{3.15}$$

$$K_1 = 1 - 0.625\left(\widetilde{M}_1' - 0.2 + |\widetilde{M}_1' - 0.2|\right) \tag{3.16}$$

$$K_p = 1 - (1 - K_1)X_p^2. \tag{3.17}$$

Reynolds number correction factor, K_{RE}

The data from which the loss model is deduced is obtained from cascade tests at a certain flow Reynolds number. K_{RE} is used to adjust the profile loss coefficient for the higher Reynolds numbers encountered in turbine operation. The correction depends on the flow regime and is therefore treated differently for laminar, transition and turbulent flows. The present model, proposed by Aungier (2006), also takes blade surface roughness into account. Figure 3-8 shows how the K_{RE} of this model varies with the chord based Reynolds number, Re_c, for different values of chord length-to-surface roughness height ratio, c/e. The equations used to model the Reynolds numbers correction factor are shown in Appendix A.1.2 as equations (A-36) to (A-40).
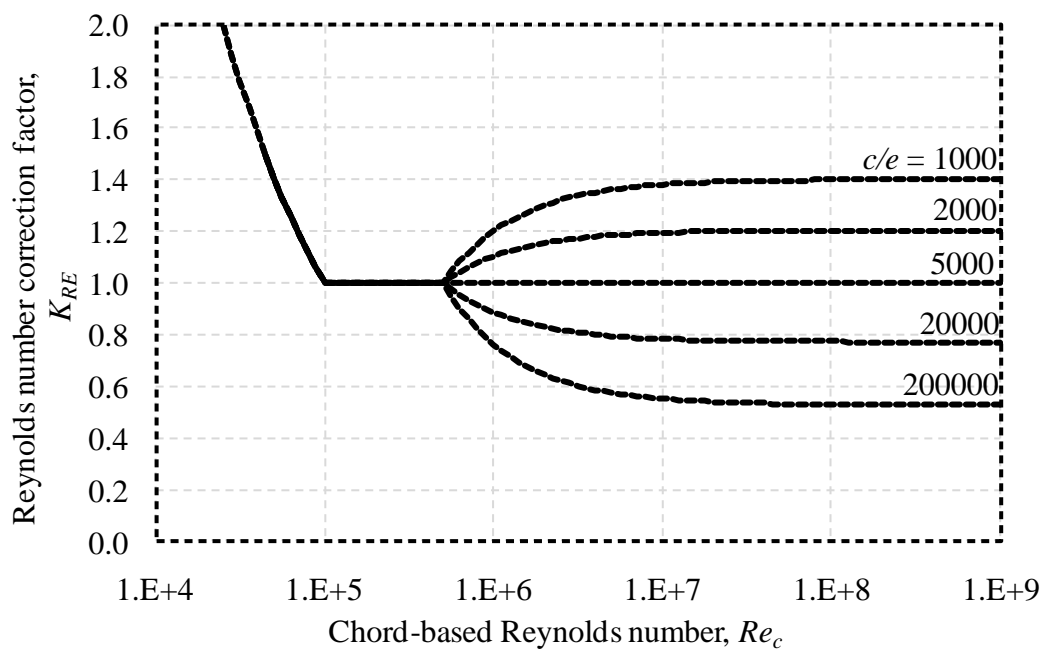
Figure 3-8: Reynolds number correction factor, adapted from Aungier (2006)

Trailing edge loss correction factor, ΔY_{TE}

Ainley and Mathieson (1951) included a trailing edge loss in their model, specifically assuming a trailing edge thickness of 2 % of a pitch, or $s/50$. This present model accounts for the trailing edge loss separately, so therefore the loss accounted for in the Ainley Mathieson model must be subtracted. ΔY_{TE} assumes the value calculated by the present trailing edge loss model for a trailing edge thickness of $s/50$.

$$\Delta Y_{TE} = Y_{TE}(t_{TE} = 0.02s) \tag{3.18}$$

$$\Delta Y_{TE} = \left(\frac{0.02s}{s \sin \beta_g - 0.02s}\right)^2 \tag{3.19}$$

3.2.4. Secondary flow loss coefficient

The secondary flow loss coefficient, Y_s, is modelled as a preliminary estimate, $\widetilde{Y}_s$, adjusted to take account of the Reynolds number and compressibility effects:

$$Y_s = K_{RE} K_s \sqrt{\frac{\widetilde{Y}_s^2}{1 + 7.5 \widetilde{Y}_s^2}} \quad . \tag{3.20}$$

K_{RE} is the Reynolds correction number shown in Figure 3-8 and K_s is a modified form of the compressibility correction factor expressed in equation (3.17). K_s is defined as

$$K_s = 1 - \left(1 - K_p\right)\left[\frac{(b_z/H)^2}{1 + (b_z/H)^2}\right] \quad . \tag{3.21}$$

The preliminary secondary flow loss coefficient is given by:

$$\widetilde{Y}_s = 0.0334 F_{AR} Z \frac{\sin \alpha'_{b1}}{\sin \beta_{b0}}, \tag{3.22}$$

where F_{AR} is the aspect ratio correction factor and Z is the Ainley loading parameter. These are respectively defined as

$$F_{AR} = \begin{cases} 0.5 \left(\frac{2c}{H}\right)^{0.7}, & H/c < 2 \\ c/H, & H/c \geq 2 \end{cases} \tag{3.23}$$

and

$$Z = \left(\frac{C_L}{(s/c)}\right)^2 \frac{\sin^2 \alpha'_{b1}}{\sin^3 \alpha'_m} \quad . \tag{3.24}$$

The mean relative flow angle, α'_m, and the lift coefficient, C_L, are respectively defined as (Aungier, 2006)

$$\alpha'_m = 90° - \text{atan}\left(\frac{\cot \alpha'_{b0} + \cot \alpha'_{b1}}{2}\right)\frac{180°}{\pi} \tag{3.25}$$

and

$$C_L = 2|\cot \alpha'_{b1} - \cot \alpha'_{b0}| \sin \alpha'_m \, (s/c) \quad . \tag{3.26}$$

3.2.5. Blade clearance loss coefficient

For unshrouded blades a leakage flow is driven across the blade tip by the pressure difference between the pressure and suction sides of the blade. This leakage flow rolls into a vortex as it exits the tip gap on the suction side, causing

further secondary flow losses (Japikse & Baines, 1994). These losses are taken into account by a loss coefficient that is dependent on the aspect ratio, relative tip gap size, and loading of the blade. The blade clearance loss coefficient, Y_{CL}, used in the present model is defined as (Aungier, 2006):

$$Y_{CL} = 0.47Z(c/H)(\delta/c)^{0.78}. \tag{3.27}$$

3.2.6. Shock loss coefficient

Kacker and Okapuu (1982) suggest including a shock loss coefficient, K_{SH}, for taking account of the shock waves that form near the hub stream sheet in turbine blades when performing a mean radius performance analysis. This coefficient is modified by Aungier (2006) to include the adverse effect of flow diffusion across a blade row. The shock loss coefficient of the present model is therefore dependent on a shock loss contribution parameter,

$$X_1 = \begin{cases} 0, & M_0' \le 0.4 \\ M_0' - 0.4, & M_0' > 0.4 \end{cases}, \tag{3.28}$$

and a diffusion loss contribution parameter,

$$X_2 = \begin{cases} 0, & M_0' <= M_1' \\ \dfrac{M_0'}{M_1'} - 1, & M_0' > M_1' \end{cases}. \tag{3.29}$$

A preliminary estimate of the shock loss coefficient is made using the contributing parameters of the shock and diffusion losses as shown in equation (3.30). This estimate is then constrained to the asymptotic upper limit of 1 in equation (3.31). (Aungier, 2006)

$$\tilde{Y}_{SH} = 0.8X_1^2 + X_2^2 \tag{3.30}$$

$$Y_{SH} = \sqrt{\frac{\tilde{Y}_{SH}^2}{1 + \tilde{Y}_{SH}^2}} \tag{3.31}$$

A sample calculation of the proposed total pressure loss coefficient model applied to the stator blade of the reverse engineered BMT 120 turbine is shown in Appendix A.1.

3.3.   Performance analysis procedure

The purpose of the performance analysis procedure is to calculate the important turbine performance parameters for a turbine rotating at a specified speed over a range of pressure ratios. The pressure ratio is varied by keeping the turbine stage inlet total temperature and total pressure constant and varying the outlet static pressure, as is preferable for turbine analysis (Mitchell, 1982). For each value of the exit static pressure the mass flow through the stage and the mean radius gas

states throughout the stage are calculated. These states are then used in calculating the turbine performance parameters. Figure 3-9 is a flow chart of the process followed to calculate the turbine performance parameters for each outlet static pressure value. With the outlet static pressure specified, estimates are made for the intermediate static pressure in the turbine stage. These estimates are then modified until the mass flow through the engine is constant across all sections. Once the mass flow through the four turbine sections has converged to a single value, the turbine performance parameters are calculated.
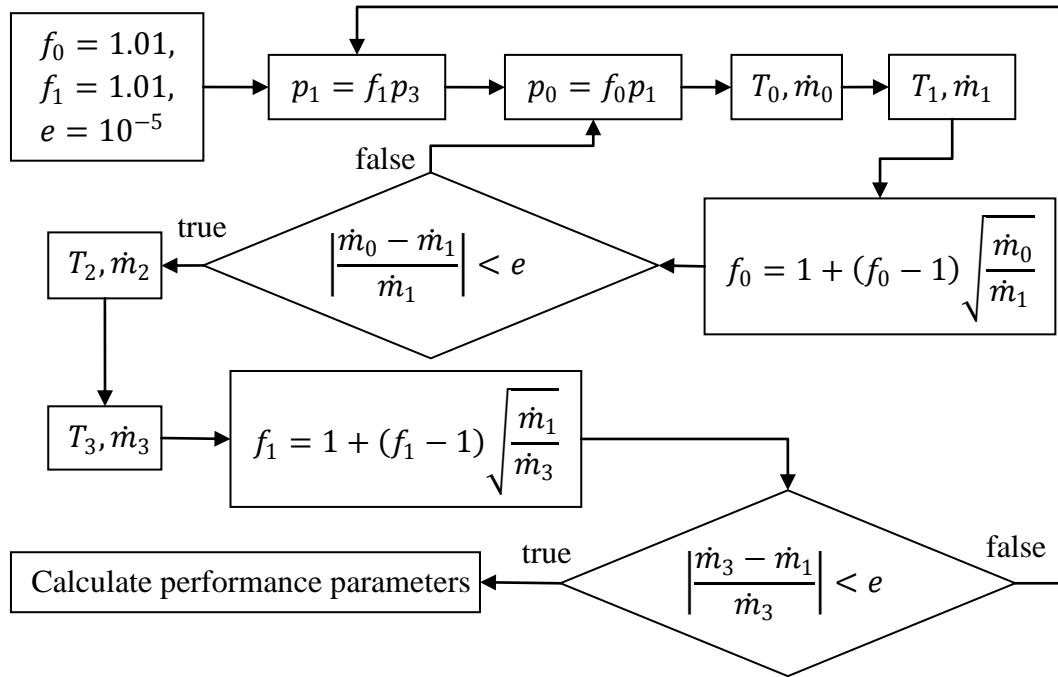
Figure 3-9: Turbine stage exit static pressure based gas state calculation procedure

3.3.1. Solving state 0: Stator inlet state

The combustion gases enter the turbine stage with a purely axial velocity and known total temperature and total pressure. For a stage outlet static pressure based state solution, an estimate of the inlet static pressure is made. Therefore, for the purposes of state calculations at the stator inlet, the inlet static pressure is also treated as a known quantity. Obtaining the mass flow rate at the stator inlet is done by first applying isentropic relations to determine the static properties. The difference between the total and static enthalpies is then used to obtain the flow velocity at the mean radius. This velocity is then multiplied by the mean radius static density and the inlet flow area to yield the mass flow at the stator inlet. A sample calculation of the final iteration of this procedure is shown in Appendix A.2.1.

29

3.3.2. Solving state 1: Stator exit state

In solving the stator exit state it is assumed that the flow conforms to the blade angle as it leaves the trailing edge. Additionally, since the stator blades impart no work to the flow and there is no heat loss, total enthalpy is conserved across this blade row. Therefore the total temperature and enthalpy are known at the stator exit.

The total pressure does not remain constant across the stator blade row due to total pressure losses in the blade row. The relative total pressure loss coefficient, Y, is used to quantify these losses and is defined as the ratio of the relative total pressure loss across a blade row to the exhaust relative dynamic pressure of the blade row:

$$Y = \frac{p'_{t,in} - p'_{t,out}}{p'_{t,out} - p_{out}}.$$

(3.32)

Y is dependent on the blade geometry, the flow velocities and gas properties on either side of the blade row. Therefore, since the flow field and gas properties are also dependent on Y, an iterative procedure is required to solve the exit state. An initial guess of Y is made, facilitating the calculation of the exit state. The resulting gas properties and flow field are then used to calculate a new total pressure loss coefficient, and the process is repeated until the loss coefficient has converged.

For the stator blade the relative total pressure loss coefficient becomes the absolute total pressure loss coefficient, since the blade row is stationary. The definition of Y_S is rearranged with the exhaust total pressure as the independent variable.

$$Y_S = \frac{p_{t0} - p_{t1}}{p_{t1} - p_1} \; \rightarrow \; p_{t1} = \frac{p_{t0} + p_1 Y_S}{Y_S + 1}$$

(3.33)

The isentropic relation for an ideal gas with varying specific heats is used to relate the total-to-static specific temperature dependent entropy difference to the total-to-static pressure ratio at any given state.

$$0 = s^o_{t1} - s^o_1 - R_{air} \ln\left(\frac{p_{t1}}{p_1}\right)$$

(3.34)

Combining equations (3.33) and (3.34) yields the following expression for the static specific temperature dependent entropy at the stator blade exit:

$$s^o_1 = s^o_{t1} - R_{air} \ln\left(\frac{p_{t0} + p_1 Y_S}{p_1 + p_1 Y_S}\right)$$

(3.35)

30

Since the resulting value is only dependent on temperature, the static temperature and the other static properties at state 1 can also be found. The static density and flow velocity magnitude are obtained as is done for the stator inlet state. However, unlike at the stator inlet state, the flow is not purely axial, since it conforms to the exit blade angle. Therefore, the axial projection of the stator exit velocity is multiplied by the corresponding gas density and flow area to yield the mass flow rate at this position. The final iteration of a sample calculation for this procedure is shown in Appendix A.2.2.

3.3.3. Solving state 2: Rotor inlet state

The blade height and mean radius may change between the stator exit state and the rotor inlet state. The change in mean radius has an effect on the circumferential velocity. This effect is modelled by enforcing conservation of angular momentum. The angular momentum of a fluid particle at the mean radius of state 1 is

$$L_1 = I_1\omega_1 = m_1 r_{m1}^2 \omega_1 = m_1 r_{m1} C_{\theta 1}. \qquad (3.36)$$

The conservation of angular momentum dictates that a fluid particle at the mean radius of state 2 should have the same angular momentum as of state 1. Assuming equal masses for the particles at the two states, the relationship between the two circumferential velocities can be shown to be

$$C_{\theta 2} = C_{\theta 1}\left(\frac{r_{m1}}{r_{m2}}\right). \qquad (3.37)$$

The changes in the annulus dimensions also yield a change in the annular cross-sectional area. This change in area is treated as either an isentropic nozzle or an isentropic diffuser, depending on the sign. The total temperature and pressure remain constant across such isentropic nozzles and diffusers. Therefore the total properties at the rotor inlet are known.

The static properties at the rotor inlet are calculated using an initial guess of the static gas density, and by assuming that the mass flow rate remains constant from state 1 to state 2. This guessed value is then used to calculate the static temperature and pressure at state 2, from which a new density is then calculated. This process is repeated until the value of the static density at the rotor inlet has converged, showing that the actual static properties have been calculated.

At state 2 the relative flow velocity and relative total gas properties become relevant. The relative circumferential velocity at state 2 is given by:

$$W_{\theta 2} = C_{\theta 2} - U_2. \qquad (3.38)$$

31

Since the motion of the blade is perpendicular to the axial direction, there is no difference between the absolute and relative axial-flow velocity. The relative flow velocity at state 2 is therefore given by

$$W_2 = \sqrt{C_{z2}^2 + W_{\theta 2}^2}. \tag{3.39}$$

This relative velocity is used to calculate the relative total gas enthalpy and pressure at state 2. A sample calculation of the final iteration in calculating state 2 is shown in Appendix A.2.3.

3.3.4. Solving state 3: Rotor exit state

The procedure for solving the rotor exit state is similar to the procedure for solving the stator exit state. The main difference between the two cases is that, since the rotor extracts work from the flow, the total enthalpy changes between state 2 and state 3. However, it can be shown that for a constant radius axial-flow blade row the relative total enthalpy remains constant across the blade row (Dixon, 1998). Therefore the same approach for determining the stator exit flow properties is used, with all the total properties being substituted by relative total properties. The mass flow rate is then calculated using the axial projection of the relative rotor exit velocity. The absolute velocity and total flow properties are then calculated from the static and relative properties and velocity. The final iteration of this procedure is shown in full as a sample calculation in Appendix A.2.4.

3.3.5. Calculating the turbine stage performance parameters

The performance parameters of a turbine stage operating at a specified total-to-static pressure ratio are the total-to-total pressure ratio, the mass flow rate and the total-to-total efficiency. The mass flow rate is calculated in the last state calculation iteration and the total-to-total pressure ratio can also be obtained directly from these calculated values. The total-to-total efficiency, however, is calculated from the equation:

$$\eta_{tt} = \frac{h_{t0} - h_{t3}}{h_{t0} - h_{t3,ideal}} \tag{3.40}$$

The ideal rotor exit total enthalpy is calculated using isentropic relations and assuming the total-to-total pressure ratio remains unchanged. A sample calculation of this procedure is shown in Appendix A.2.5.

3.4. Results of empirical performance analysis

The performance analysis procedure described in section 3.3 is applied to the reverse engineered turbine of the BMT 120 KS engine. The inlet total pressure and total temperature is taken to be 308,3 kPa and 1119 K respectively and performance curves are generated for four rotor speeds. These curves of total-to-

32

total efficiency and actual-to-design mass flow rate ratio are shown in Figure 3-10. It can be seen that the peak total-to-total efficiency moves from a lower to a higher pressure ratio as the rotational speed of the turbine is increased. The same trend is also visible for the peak mass flow rate through the turbine. These trends correspond well to those on a similar turbine performance map published by Cohen *et al.* (1996). However, it can also be seen that the mass flow rate predicted by the empirical performance analysis is substantially lower than the design mass flow rate of the BMT 120 KS turbine of 0,29 kg/s, given in Table 4-2. This discrepancy in the mass flow rate prediction suggests that assumptions made in the analysis procedure are inaccurate for the BMT 120 KS turbine. The assumption of the mean radius mass flux being equal to the average mass flux at a given cross section is a likely source of this inaccuracy, as suggested by Cohen *et al.* (1996).

3.5.   Conclusion

A mean radius performance analysis procedure using empirical loss correlations was developed. The empirical loss model was described and the analysis procedure for calculating the performance of a turbine under specified conditions was proposed. This procedure was applied to an existing turbine design and a turbine performance map was generated. This performance map compares well with the trends shown in similar charts in literature, even though the mass flow rate was substantially under predicted.
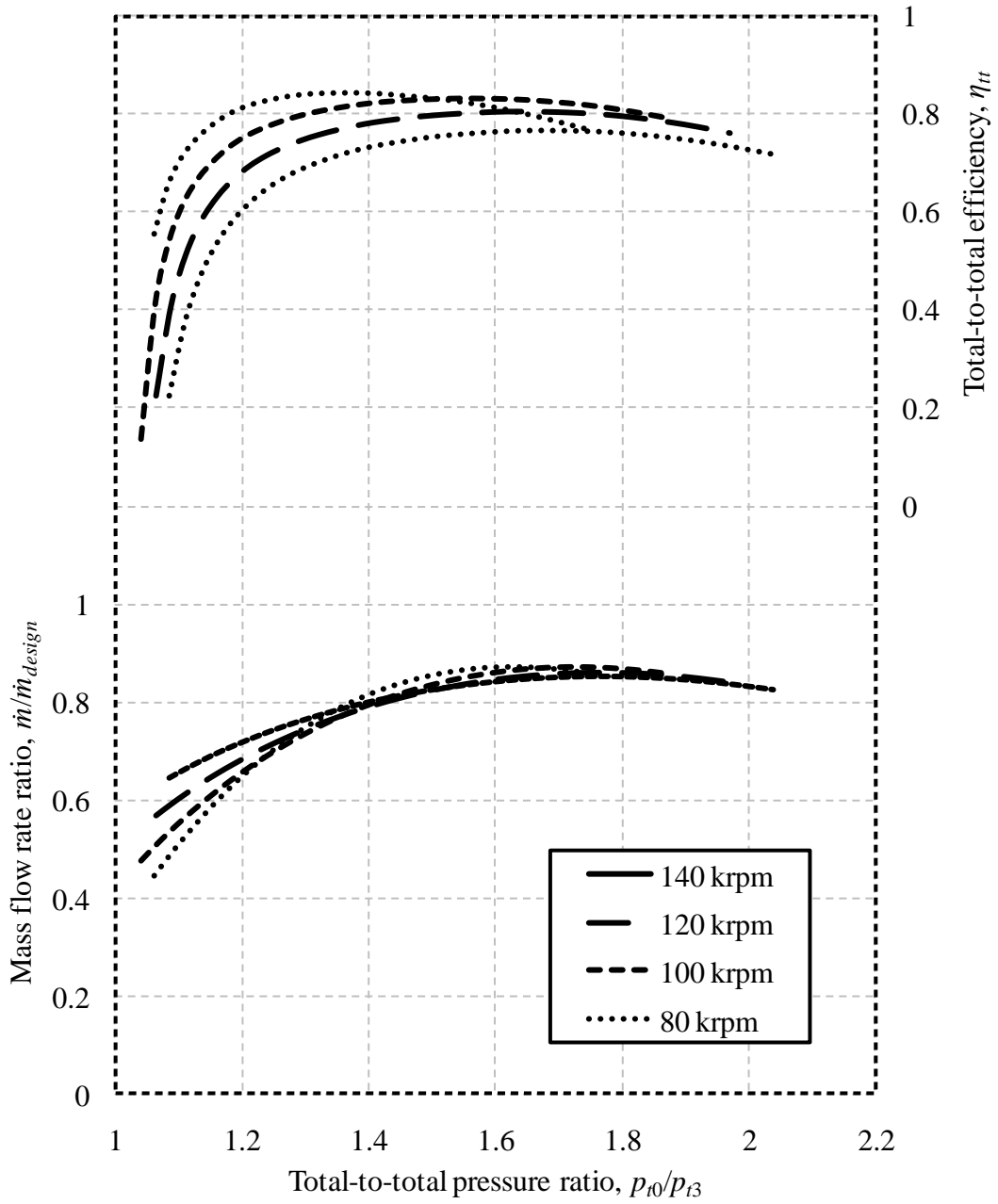
Figure 3-10: BMT 120 KS turbine empirical performance map at T_{t0} = 1119 K, p_{t0} = 308300 Pa

4. Turbine design process

4.1. Introduction

This section describes the procedure for designing an axial-flow turbine to match the requirements of an existing micro gas turbine engine. Designing a turbine for an existing engine simplifies the evaluation of the generated turbine design, since the existing turbine design provides a clear baseline to which any new design can be compared. Once the turbine performance requirements of the existing engine have been determined, the design process is identical to the case where a turbine for a new engine is designed.

Firstly the assumptions and primary design decisions are stated; whereafter the turbine design parameters are identified. The values of these parameters are deduced from measurements and test results of the existing engine. These parameters are then used to calculate the mean radius gas velocity vectors before and after each blade row and to make a preliminary stage efficiency estimate. The gas velocity magnitudes are then used along with the efficiency estimate to approximate the mean radius thermodynamic gas properties before and after each blade row. Once the gas properties, specifically the gas density, are known throughout the stage, the annular flow passage is sized to pass the design mass flow rate. The mean radius blade profiles are then also calculated, thus enabling the empirical loss model to predict the total pressure loss coefficient of each blade row. The properties of the gas throughout the turbine stage are then recalculated using these loss coefficients, instead of the preliminary efficiency estimates. These properties are then used to finalise the sizing of the annular flow passage. Once the geometry of the flow passage is finalised, the blade profiles from root to tip can be generated. This profile information is then converted to three-dimensional models of each blade row.

4.2. Assumptions and design decisions

4.2.1. Machine type and geometry

The existing micro gas turbine engine, for which the new turbine is to be designed, is fitted with a single stage axial-flow turbine. The stage consists of a shrouded stator blade row and an un-shrouded rotor blade row. This configuration is adopted for the new design to simplify integration into the existing engine. Figure 4-1 shows a turbine stage with the adopted configuration. Part of the shrouded stator is removed for clarity.

Figure 4-1: Turbine stage configuration

The mean radius of the turbine stage is chosen to remain constant throughout the turbine. Therefore, when the properties of the flow along the mean radius stream sheet are calculated, the radius of the flow remains constant before and after a blade row. This invariance in radii causes the mean radius relative stagnation enthalpy to be conserved across both stationary and rotating blade rows.

4.2.2. Swirl velocity distributions

A free vortex swirl velocity distribution is chosen for the exit to the stator blade row. This is the most common choice of swirl velocity vortex type for axial-flow gas turbines (Aungier, 2006), since it minimizes kinetic energy losses associated with vortical motion in the gas (Baskharone, 2006). This choice results in both the axial components of the gas velocities and the blade work per unit mass of flow being invariant with radius. The flow entering and leaving the turbine stage is chosen to be purely axial. The swirl velocity distribution of the entering flow comes from the combustion chamber and is therefore neither steady, nor uniform. Therefore, the assumption of a purely axial velocity is made to average out the fluctuating flow. The axial turbine exit flow velocity is chosen to minimise the total pressure lost due to the exit flow kinetic energy.

4.2.3. Streamwise constant axial velocity

The density of the gas passing through a turbine decreases from inlet to outlet. The accompanying increase in specific volume flow rate leaves the designer with two options. Firstly, the flow passage can have a constant cross-sectional area. The constant flow area would require continuity to be enforced by an increase in gas axial velocity from inlet to outlet. Such an increase in axial velocity may, however, cause unacceptably high relative Mach numbers on the trailing edge of the rotor row. Therefore the second option is to have the cross-sectional area of the flow passage increase from inlet to outlet. This configuration would allow the the specific volume flow rate to increase without the risk of excessively high axial velocities and the accompanying choking danger.

For the present design a constant axial velocity is specified throughout the turbine stage. This specification alleviates the danger of excessively high blade exit Mach numbers and simplifies the calculation of the mean radius gas properties throughout the turbine stage. The resulting diverging hub and shroud walls are shown in Figure 4-2 where the flow area increases from position 0 at the inlet to position 3 at the outlet.

4.3.   Design parameters

The parameters that dictate the design of the turbine can be divided into three categories. These categories are:

- the constraints placed on the geometry of the turbine stage,
- the thermo-physical properties of the gases exiting the combustion chamber,
- and the turbine performance required to drive the compressor at the design point.

In this section the variables relevant to each parameter category are identified, and the procedure for determining the values of these variables is explained.

4.3.1. Geometrical constraints

In a case where a turbine is designed to be retrofitted to an existing jet engine certain geometrical constraints must be met. These constrains consist of limits on the total external turbine stage dimensions and limitations placed on the stage inlet geometry. Figure 4-2 also shows these limiting dimensions.
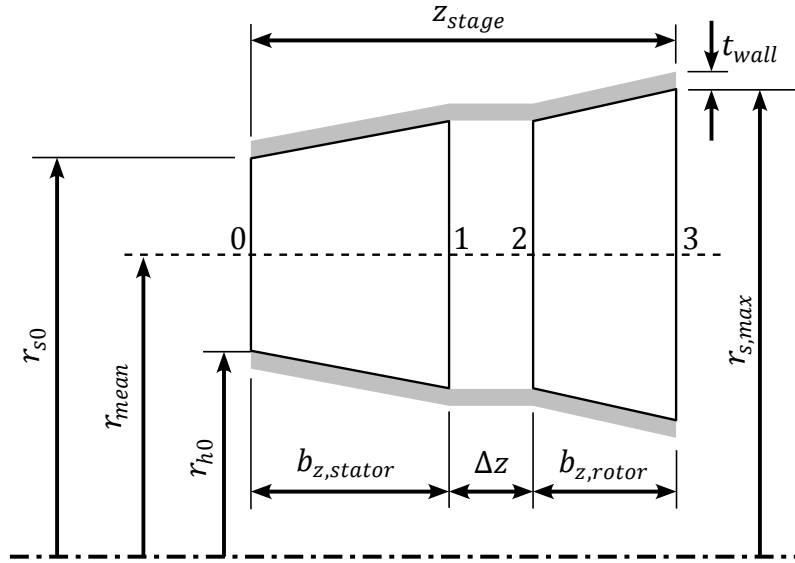
Figure 4-2: Geometrical constrains and turbine axial position definition

Total external stage dimensions

A limited amount of space within the housing of the engine is available for the turbine stage. Therefore, the maximum external diameter and stage length are limited. The limit on the external diameter, d_{max}, translates into a limit on the maximum shroud inner radius, $r_{s,max}$, and wall thickness, t_{wall}. This limitation can be expressed as:

$$\left(r_{s,max} + t_{wall}\right) \le d_{max}/2 .$$ (4.1)

The limit on the total stage length allows for the fixing of the stator and rotor blade axial chords. In accordance with accepted design practice, the axial gap between the two blade rows, $\Delta z,$ is then chosen to be 50% of the average of the two axial blade chords (Cohen, et al., 1996):

$$\Delta z = 0.5 \left(\frac{b_{z,stator} + b_{z,rotor}}{2}\right).$$ (4.2)

This then yields a total stage length of:

$$z_{stage} = b_{z,stator} + b_{z,rotor} + \Delta z.$$ (4.3)

Stage inlet geometry

The inlet geometry of the turbine stage must be compatible with the exit geometry of the preceding combustion chamber. Therefore the turbine stage inlet annular flow path section must fit within the annular exit flow path section of the combustion chamber. This limitation translates into a maximum allowable inlet shroud radius and a minimum allowable inlet hub radius.

Values for the geometrical design parameters are chosen to meet the aforementioned constraints. The values for the present design are shown in Table 4-1.

Table 4-1: Geometrical design parameter selections

Geometrical parameter name	Parameter value
Stage inlet hub radius, r_{h0}	23,5 mm
Stage inlet shroud radius, r_{s0}	31,5 mm
Stator blade axial chord, $b_{z,stator}$	9 mm
Rotor blade axial chord, $b_{z,rotor}$	7 mm

4.3.2. Inlet gas properties

The inlet gas properties of a turbine stage are obtained indirectly from compressor test results. Experimental work was done on the present engine by Krige (2012). The performance data obtained from this experimental work is shown in Table 4-2.

Table 4-2: Current engine experimental test data at 120 krpm. (Krige, 2012)

Parameter name	Parameter value
Air mass flow rate, $\dot{m}_{air}$	0,29 kg/s
Fuel mass flow rate, $\dot{m}_{fuel}$	0,0054 kg/s
Compressor inlet total temperature, $T_{C,t,in}$	289 K
Compressor inlet total pressure, $p_{C,t,in}$	101 kPa
Compressor exit total pressure, $p_{C,t,out}$	310 kPa
Compressor total-to-total efficiency, $\eta_{C,tt}$	85 %
Turbine exit total temperature, $T_{T,t,out}$	1009 K

The compressor inlet temperature, efficiency and pressure ratio are used to calculate the amount of work imparted to the flow by the compressor of the jet engine. This compressor work can then be multiplied by the air mass flow rate to obtain the mechanical power required to drive the compressor. Assuming negligible mechanical losses, the turbine is then required to extract the same amount of power from the flow to drive the compressor. The mass flow rate through the turbine includes both the compressor air mass flow rate and the fuel mass flow rate. Therefore, the turbine work per unit mass is found by dividing the compressor power by the turbine mass flow. Adding the turbine work per unit mass to the turbine outlet total enthalpy yields the turbine stage inlet total enthalpy, and hence the inlet total temperature. The turbine inlet total pressure is obtained by assuming a zero total pressure loss through the combustion chamber. Therefore, the total pressure at the turbine inlet equals the total pressure at the compressor exit. The turbine inlet gas properties are shown in Table 4-3. The procedure for calculating the turbine inlet total pressure and temperature is shown in Appendix B.1.

Table 4-3: Turbine inlet gas properties

Parameter name	Parameter value
Turbine inlet total temperature, T_{t0}	1119 K
Turbine inlet total pressure, p_{t0}	310 kPa

4.3.3. Turbine performance requirements

The performance requirements of the turbine at the design points consist of the power output, the rotational speed and mass flow rate. At the design point, the turbine must drive the compressor at 120,000 revolutions per minute. Therefore, the design point is at the same operating conditions as the test data of Table 4-2. Therefore, the mass flow rate and the turbine power output are required to equal the values used to calculate the turbine inlet total temperature.

Non-dimensional forms of the performance requirement are calculated at the mean radius for use during the design process. The non-dimensional flow coefficient, work coefficient and reaction ratio, as defined in Appendix B.3, are obtained from the turbine performance requirements and the chosen geometrical design parameters. The shapes of the turbine stage velocity triangles are determined by the values of these non-dimensional parameters (Wilson, 1987). The non-dimensional performance parameters and dimensional performance requirements are shown in Table 4-4. A numerical example of the procedure used

to calculate the non-dimensional performance parameters is shown in Appendix B.2.

Table 4-4: Turbine performance requirements

Parameter name	Parameter value
Turbine power output, P_T	37 kW
Turbine mass flow rate, $\dot{m}_T$	0,29 kg/s
Turbine rotational speed, N_T or ω_T	120 krpm or 12 600 rad/s
Turbine flow coefficient, ϕ_{mean}	0,69
Turbine work coefficient, ψ_{mean}	1,06
Turbine reaction ratio, R_{mean}	0,47

4.4. Mean radius gas velocity triangles and efficiency estimate

4.4.1. Calculating the mean radius gas velocity triangles

The mean radius gas velocity vectors are dependent on the specified stage work and flow coefficients, as well as the absolute stage inlet and exit flow angles. The unknown absolute and relative gas angles are calculated using equations (4.4) and (4.5) and equations (4.6) and (4.7) respectively.

$$\alpha_{1,mean} = \text{atan}\left(\frac{1 - R_{mean} + \frac{\psi_{mean}}{2}}{\phi_{mean}}\right) \tag{4.4}$$

$$\alpha_{2,mean} = \alpha_{1,mean} \tag{4.5}$$

$$\alpha'_{2,mean} = \text{atan}\left(-\frac{R_{mean} - \frac{\psi_{mean}}{2}}{\phi_{mean}}\right) \tag{4.6}$$

$$\alpha'_{3,mean} = \text{atan}\left(-\frac{R_{mean} + \frac{\psi_{mean}}{2}}{\phi_{mean}}\right) \tag{4.7}$$

The constant mean radius axial gas velocity component is calculated from the flow coefficient and the blade speed in equation (4.8).

$$C_{z,mean} = \phi_{mean} U_{mean} \tag{4.8}$$

The absolute and relative gas velocity magnitudes at any position, i, along the turbine stage are given by equations (4.9) and (4.10) respectively. The derivation of equations (4.4) to (4.7) is explained and the resulting numerical values of the stage mean radius gas velocities are shown in Appendix B.3.

$$C_{i,mean} = C_{z,mean}/\cos \alpha_{i,mean} \tag{4.9}$$

$$W_{i,mean} = C_{z,mean}/\cos \alpha'_{i,mean} \tag{4.10}$$

4.4.2. Preliminary efficiency estimate
The purpose of the preliminary design process is to produce candidate designs for the detail design process. Therefore, it would be helpful to determine whether or not a preliminary design is likely to yield acceptable performance. This is accomplished by obtaining a stage efficiency estimate from a standardised efficiency chart.

The Smith chart (Smith, 1965) is a standardised efficiency chart that is widely accepted as feasible for use during preliminary turbine design. It is a plot of total-to-total efficiency contours on axes of flow coefficient and work coefficient. Aungier (2006) made an empirical correlation from the Kacker and Okapuu (1981) data that shows good agreement with the Smith chart. It yields an expression for the total-to-total efficiency of a stage as a function of its flow and work coefficients as shown in equations (4.11) to (4.14).

$$\phi_{opt} = 0.375 + 0.25\psi_{mean} \tag{4.11}$$

$$\eta_{opt} = \begin{cases} 0.913 + 0.103\psi_{mean} - 0.0854\psi_{mean}^2 + 0.0154\psi_{mean}^3, & \psi_{mean} \leq 2.8 \\ 1.01 - 0.05\psi_{mean}, & \psi_{mean} > 2.8 \end{cases} \tag{4.12}$$

$$K_1 = \begin{cases} 0.375 - 0.125\psi_{mean}, & \psi_{mean} \leq 2.2 \\ \dfrac{0.22}{\psi_{mean}}, & \psi_{mean} > 2.2 \end{cases} \tag{4.13}$$

$$\eta_0 = \eta_{opt} - K_1(\phi_{mean} - \phi_{opt}) \tag{4.14}$$

This correlation assumes a reaction ratio of 50%, no tip clearance and moderate to high blade aspect ratios. Aungier (2006), however, corrects for these assumptions by using a standard tip clearance approximation,

42

$$K_2 = \frac{\delta}{r_{mean} + H_0/2},\tag{4.15}$$

and an aspect ratio correction that is also dependent on the reaction ratio,

$$X = H_0(0.4 + 0.5R_{mean}).\tag{4.16}$$

Therefore, the corrected total-to-total efficiency is given by

$$\eta_{tt} = \eta_0 \left[1 + 0.93K_2 \left(\frac{r_{mean}}{H_0}\right)\left(1 + \frac{0.5H_0}{r_{mean}}\right)^2\right] X^{0.05+0.04R_{mean}}.\tag{4.17}$$

This initial efficiency estimate is to be used in the preliminary calculation of the gas states along the mean radius throughout the turbine stage. In addition to the turbine stage total-to-total efficiency, the nozzle efficiency of the stator blade row is also required for a gas states calculation. A stator blade row nozzle efficiency of 94 % is assumed for the preliminary state calculations of the following section.

4.5.   Gas states calculation

The thermodynamic states of the gases passing through the engine are calculated at four locations along the mean radius of the turbine stage. These locations correspond to the inlet and outlet planes of the stator and rotor blades rows. The knowledge of the gas states enables the sizing of the flow path at the different locations and is also necessary for the empirical performance analysis of each blade row. It also enables the mean radius flow Mach numbers to be calculated.

The gas states are calculated using two independent procedures. Initially, the states are calculated using the preliminary turbine stator blade row nozzle efficiency and turbine stage total-to-total efficiency estimates to account for the entropy increase through the stage. These calculations are used to generate the Mollier diagram of the turbine stage shown in Figure 4-3. In Figure 4-3 the points denoted by 1*s* and 3*s* are respectively the stator exit and rotor exit ideal states. The points denoted 3*ss* refer to the ideal stage exit states.

The results of this initial state calculation are used as an input into the empirical loss model of Section 3. The empirical loss model yields relative total pressure loss coefficients that are then used in the gas states calculations of all subsequent design iterations. A numerical example of the gas states calculation, using the converged values of the relative total pressure loss coefficients of the two blade rows, is shown in Appendix B.4.
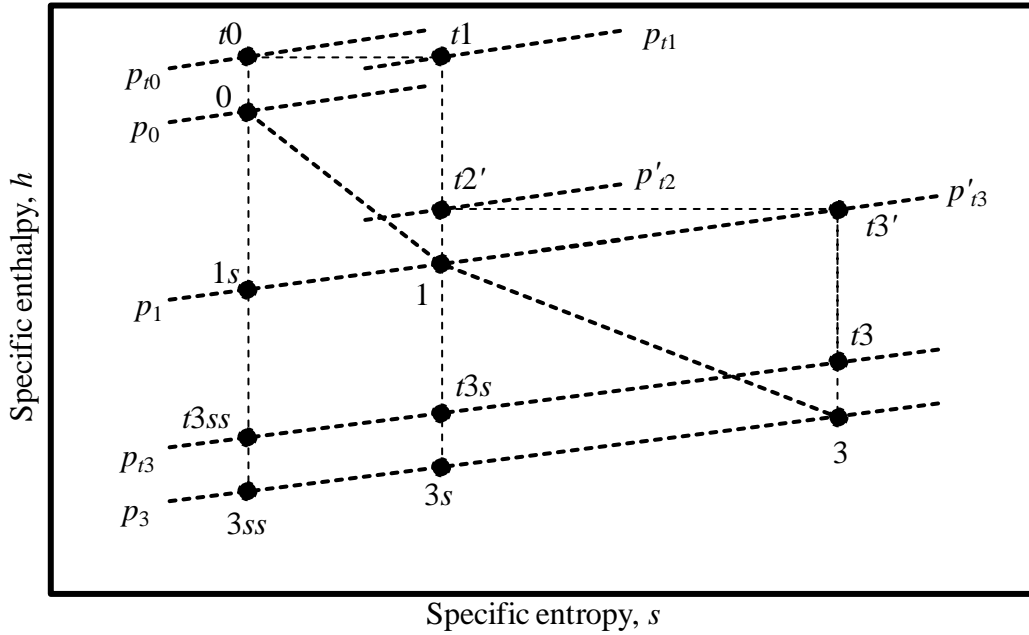
Figure 4-3: Mollier diagram of a turbine stage

4.6. Flow path annulus sizing

The hub and shroud profiles of the turbine stage must be specified to allow the design mass flow rate to pass through the stage. The mass flow rate through a section, i, of the turbine stage is given by

$$\dot{m}_i = \int_A \rho_i (C_z)_i dA = 2\pi \int_{r_h}^{r_s} \rho_i C_{z,i} r \, dr. \tag{4.18}$$

The present turbine stage has axial inlet and exit velocities and a free-vortex swirl velocity distribution between the stator and rotor blade rows. Therefore, at the four positions where the mean radius gas states are known, the axial gas velocities are invariant with radius. For annuli with a free-vortex swirl velocity distribution the gas density varies radially. However, Cohen *et al.* (1996) proposes the use of the mass flux mean radius as the mean mass flux. Therefore equation (4.18) can be simplified to yield equation (4.19).

$$\dot{m}_i = 2\pi \rho_i C_{z,i} \int_{r_h}^{r_s} r \, dr \tag{4.19}$$

44

The axial velocity and mean radius are chosen to remain constant throughout the stage. These assumptions also simplify equation (4.19), allowing it to be re-ordered to yield the expression for the blade height in equation (4.20).

$$H_i = \frac{\dot{m}_i}{2\pi r_{mean} C_z \rho_i} \qquad (4.20)$$

The stage inlet hub and shroud radii are already specified in Table 4-1. The hub and shroud radii at the three remaining positions are then obtained from the mean radius and the blade heights calculated using equation (4.20). These radii describe the hub and shroud contours at four sections along the length of the stage. The radii at these points are interpolated to yield piece-wise linear hub and shroud contours, similar to the contours shown in Figure 4-2.

4.7.   Blade profile construction

The gas velocity triangles have been calculated to yield the desired turbine stage performance. However, turbine blades are needed to produce a flow field that conforms to these velocity triangles. These blades require cross-sectional profiles that impart the appropriate amount of swirl to the moving gases, whilst causing minimal flow obstruction and entropy generation. The blade cross sections are designed by first evaluating several general geometric blade row parameters using empirical correlations. A thickness-camber scheme to describe the blade profiles is chosen because of the low number of variables required to define an airfoil shape (Wesssels, et al., 2012). The geometric parameters are then used to generate blade camber line curves with inlet and outlet angles that conform to the desired flow field. A distribution of the blade thickness along the camber line is then chosen. These thickness distributions are then added perpendicularly to both the pressure and suction sides of the camber line curves. The resulting curves form the edges of the suction and pressure surfaces on the blade profile.

4.7.1. Blade row geometric parameters
Different parameters are used to characterise the geometry of a blade row. By adjusting these parameters and the ratios between pairs of these parameters the shape of a blade profile can be controlled. Therefore, an attempt is made to find near-optimal values of the blade parameters for the specified design parameters.

Determining the optimal pitch-to-chord ratio
The pitch-to-chord ratio of a blade row is a measure of the size and number of blades in the blade row. When large flow deflections are required, lower pitch-to-

chord ratios are required than when smaller flow deflections are required. The size and number of the blades can however not increase indefinitely due to the blockage caused in the flow passage and other geometrical and material constraints. Therefore an optimal pitch-to-chord ratio is required to ensure that a blade row is capable of achieving the required flow deflection, whilst not causing undue flow passage blockage.

The optimal pitch-to-chord ratio is determined by applying an empirical correlation that uses the generic blade angle convention (Ainley & Mathieson, 1951). This correlation works from the assumption that any turbine blade can be reconstructed as a weighted combination of a pure nozzle blade and an impulse blade. The weighting is done using the gas deflection ratio, ξ, as defined in equation (3.5). Ainley and Mathiesson (1951) published correlations for the optimal pitch-to-chord ratios for pure nozzle blades and impulse blades. These correlations are used in the empirical performance analysis of Section 3 and shown in Figure 3-2. The resulting optimal pitch-to-chord ratios for a range of turbine blade inlet and outlet angles are shown in Figure 4-4.

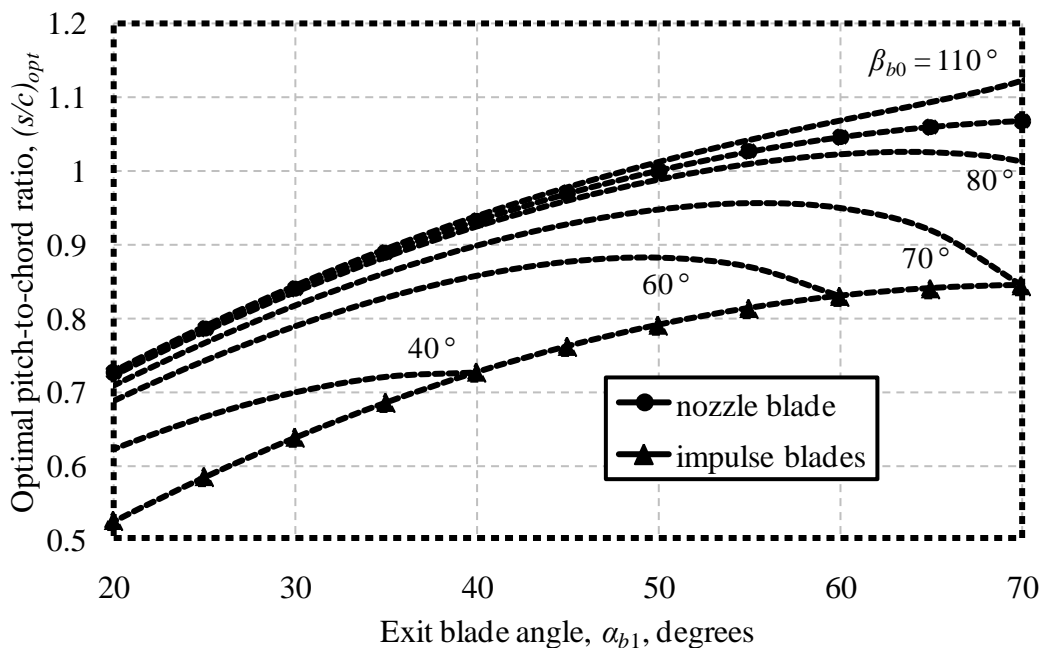Figure 4-4: Optimal pitch to chord ratio for different combinations of blade inlet and exit angles

Determining the blade pitch, chord and stagger angle
The next step in designing turbine blades is to determine the values of various geometric blade parameters. These parameters are primarily the blade stagger angle, the blade pitch and chord length. These primary blade parameters are also

46

related to the blade gauge angle, deviation angle and the number of blades. An empirical correlation from Aungier (2006) is used to estimate the optimal values of these three parameters. The throat-pitch ratio is given as:

$$\left(\frac{o}{s}\right) = F_{AR} \sin(\beta_1 - \delta).$$
(4.21)

The stream sheet area ratio correction is given by:

$$F_{AR} = 0.8 + 0.2 \left(\frac{\rho_0 C_{z0}}{\rho_1 C_{z1}}\right).$$
(4.22)

The deviation angle, defined in equation (4.23), is a function of the zero relative exit Mach number deviation angle, given by equation (4.24), and the relative exit Mach number.

$$\delta = \begin{cases} \delta_0, & M_1' \leq 0.5 \\ \delta_0[1 - 10(2M_1' - 1)^3 + 15(2M_1' - 1)^4 - 6(2M_1' - 1)^5], & M_1' > 0.5 \end{cases}$$
(4.23)

$$\delta_0 = \sin^{-1}\left\{\left(\frac{o}{s}\right)\left[1 + \left(1 - \frac{o}{s}\right)\left(\frac{\beta_g}{90°}\right)^2\right]\right\} - \beta_g$$
(4.24)

The gauge angle and stagger angle are given by equations (4.25) and (4.26) respectively.

$$\beta_g = \sin^{-1}(o/s)$$
(4.25)

$$\gamma = \frac{\left(180° - \beta_0 + 1.5\beta_g\right)}{2.5}$$
(4.26)

The blade chord is then calculated from the specified axial chord and the calculated stagger angle. This allows the blade pitch to be calculated by also using the pitch to chord ratio. Finally the number of blades is calculated from the blade pitch and the mean radius. The resulting value is rounded to the nearest prime integer or prime integer double. The use of a prime number of blades minimises the number of cyclic disturbance frequencies a blade would be subjected to during operation. These profile geometrical parameters are highly interrelated. Therefore an iterative procedure is used to satisfy all the relationships. A numerical example of calculating the rotor blade row geometrical parameters is shown in Appendix B.5.

4.7.2. Blade camber line
The known values of the blade chord length and the stagger angle yield the relative positions of the leading and trailing edge points of the blade profile. These

relative coordinates, along with the known blade angles allow for the design of a Bézier curve to describe the blade camber line. Figure 4-5 shows the inlet and outlet blade angles and the relative positions of the leading and trailing edge points. A quadratic Bézier curve and its control polygon are also shown. The positions of the end points of the curve coincide with the leading and trailing edge points of the blade. The Bézier curve is also tangential to the respective blade angles at its end points.
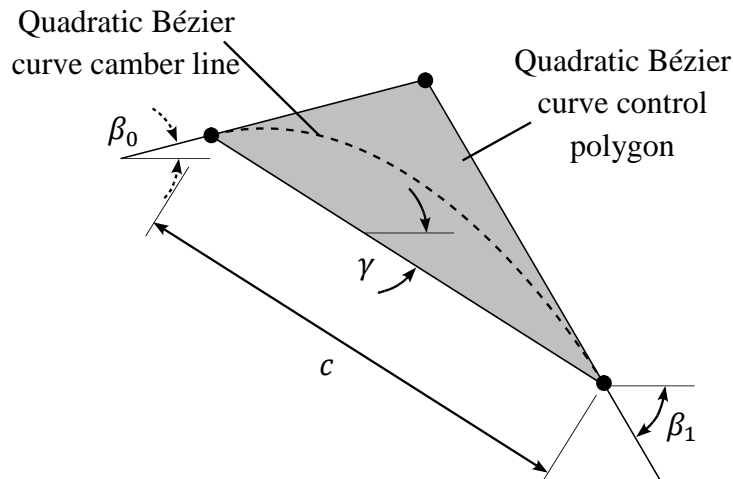
Figure 4-5: Quadratic Bézier curve camber line

The use of a quadratic Bézier curve does yield a smooth and continuous camber line curve, but no control of the position or abruptness of the curvature is possible. For a more flexible design approach, the use of a higher order Bézier curve is required. A cubic Bézier curve has an additional control point, and therefore the control polygon is not fully described by the positions and slopes of the curve at its end points. The position of each of the two central control points can be varied in two different ways to provide flexibility in the shape of the curve. Figure 4-6 shows four different cubic Bézier curve camber lines and their respective control polygons. The corresponding quadratic Bézier curve camber line and control polygon are also shown for comparison.

Firstly, the two points can both be moved further from or nearer to the central control point of the corresponding quadratic Bézier curve. This has the effect of making the curvature of the resulting camber line more or less abrupt. This variation in the abruptness of curvature can be seen in Figure 4-6(a). Secondly, two points can be moved either forwards or backwards to move the location of the

48

camber line curvature towards either the leading or trailing edge points. This movement of the curvature position is shown in Figure 4-6(b).
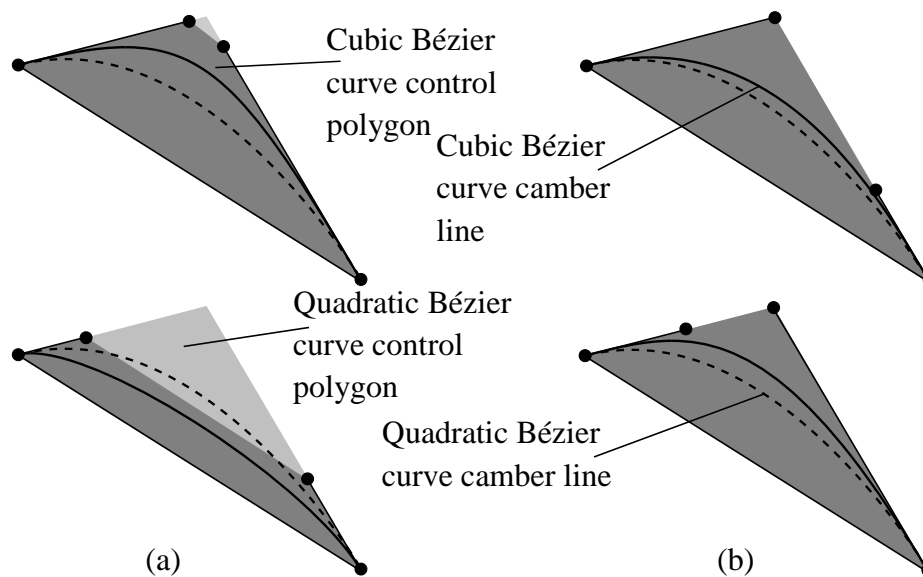
Figure 4-6: Variation of cubic Bézier curve camber line shapes

4.7.3. Blade thickness profile

A blade thickness profile is added to the existing camber line curve. A T6 profile, a thickness profile commonly used for gas turbine blades (Cohen, et al., 1996), is used as a starting point for the thickness distribution. A fifth-degree Bézier curve is then used to create a curve that approximates the T6 profile definition points. The use of higher-order Bezier curves enforces the third-order continuity that keeps the Mach number distribution smooth, resulting in lower trailing edge losses (Korakianitis & Papagiannidis, 1993). The Bézier curve and its control polygon, together with the T6 profile definition points are shown in Figure 4-7. The central four control points of the Bézier curve can be moved around to modify the blade thickness distribution. The first and fourth control points can only be moved transversely, enabling control of the leading and trailing edge thickness. In Figure 4-7 it can be seen that the fourth control point is moved to yield a trailing edge that is thicker than what the T6 defining points describe.

Once the blade profile camber line and thickness distribution have been determined, the thickness distribution is applied to the camber line. The resulting blade profile conforms to the flow field for which it was designed.
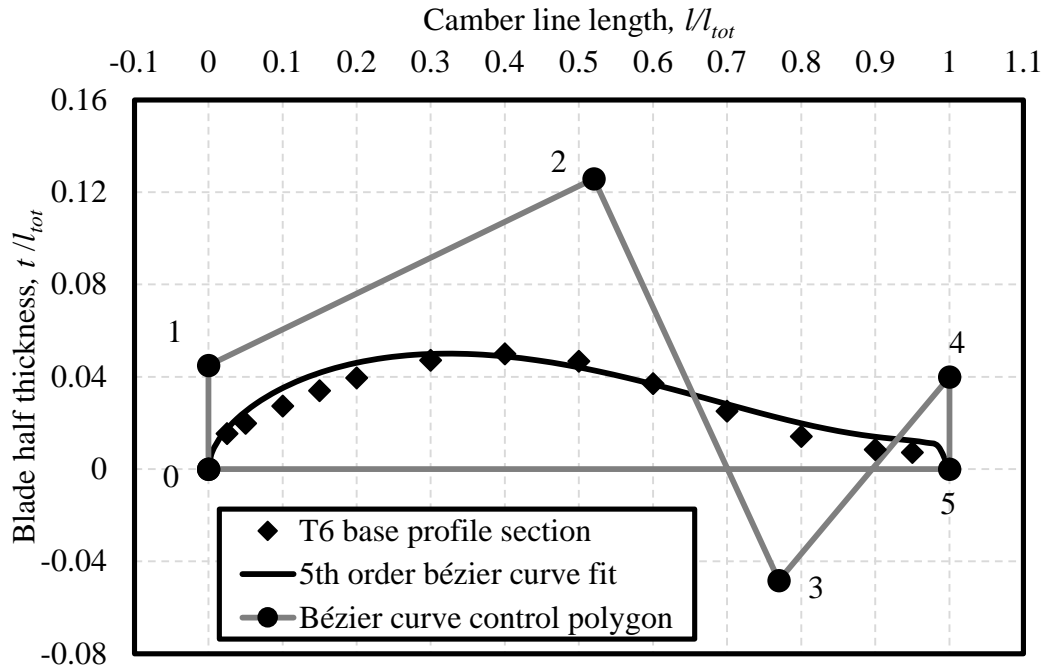
Figure 4-7: Blade thickness profile curve

4.8.   Empirical performance analysis

Three new turbine designs are analysed using the empirical performance analysis procedure of Section 3. The three designs are all designed to the parameters of Table 4-1, Table 4-3 and Table 4-4, with the only exception being the mean radius work coefficient. The target mean radius work coefficients of the three designs are respectively 95 %, 100 % and 105 % of the tabulated value. The empirical performance analyses are carried out at the design speed of 120,000 revolutions per minute. Figure 4-8 shows the results of the performance analyses for the three new designs. As can be seen in Figure 4-8, the three new designs can achieve the design mass flow rate according to the empirical performance analysis. The total-to-total efficiencies of the three designs are close to 90 % at the design mass flow rate. This is enough evidence to justify further investigation into the performance of these three designs.
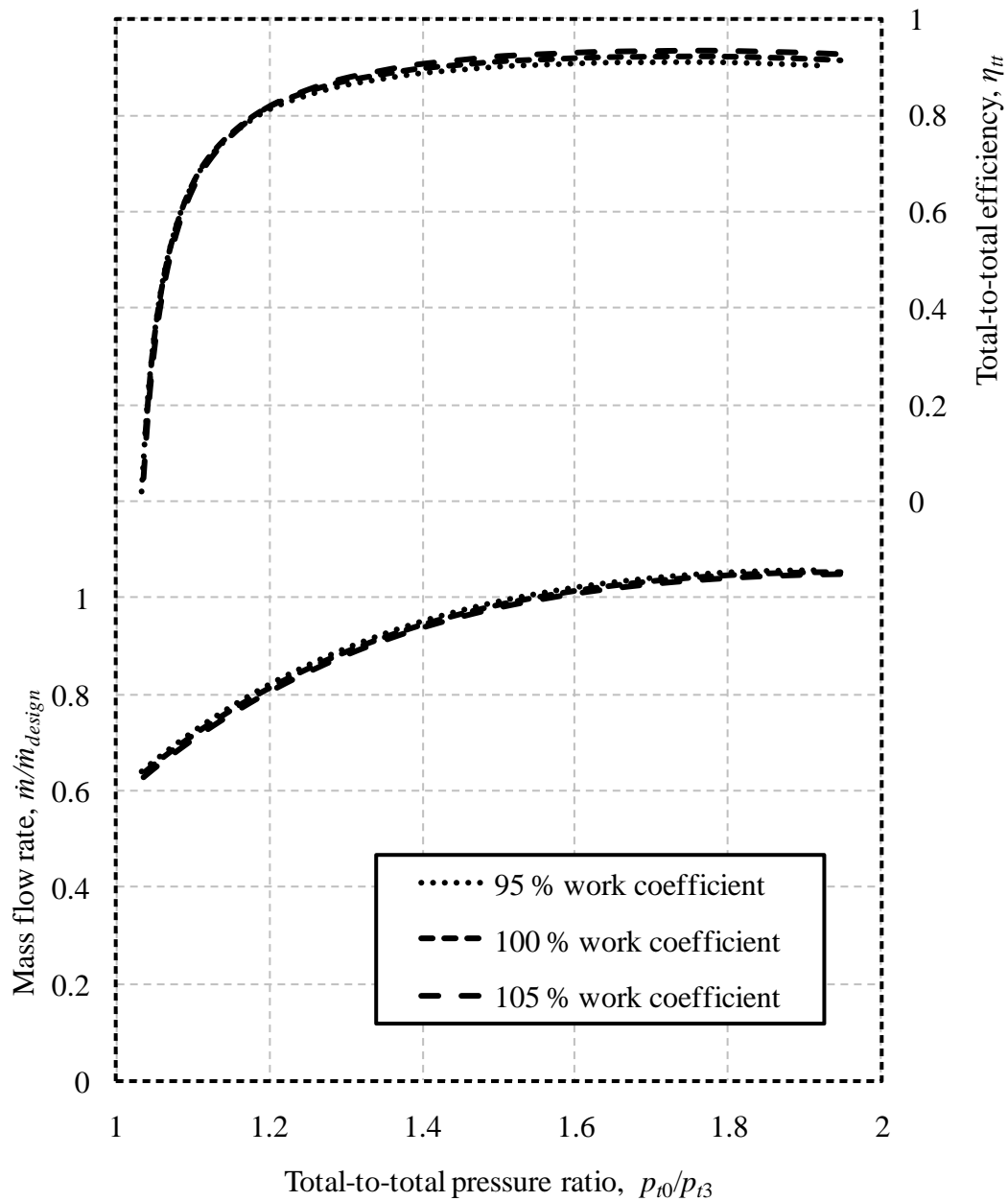
Figure 4-8: New turbine design empirical performance analysis results

4.9.   Root-to-tip blade design

In some cases, the mean radius blade profiles are used for the whole span of the blade for geometric simplicity. However, for free-vortex swirl velocity distributions, a large amount of blade twist is required. Therefore, the blade profiles must be individually defined at a number of radial stations from root to

tip. This is done by first calculating the flow angles at each radial station and then calculating the profile geometrical parameters. The blade profile for each radial station is then calculated. These profiles can then be stacked along an appropriate stacking axis to generate a three-dimensional blade model.

4.9.1. Free-vortex velocity triangles

The gas velocity triangles for the stream sheet of each radial station are calculated using free-vortex theory. For a free-vortex stator design the circumferential component of the absolute flow velocity between the two blade rows is inversely proportional to the radius of the radial station. Since the mean radius gas velocity triangles have been fixed, the free-vortex constant is already available. Free-vortex theory also dictates that the axial velocity remains constant with radius. Therefore, since the mean radius velocity vectors are known, the velocity vectors at the other radial station can be readily calculated.

4.9.2. Radial station blade profiles

With the flow velocity triangles at a radial station known, the blade profile parameters can be calculated. The same procedure used to calculate the mean radius profile can be used. However, the blade pitch is determined by the radius of the radial station, since the number of blades has already been specified.

The blade profile camber lines are calculated as before from the blade inlet and outlet angles, stagger angles and chords for each radial station. The pressure and suction surface edges are also calculated as a combination of the camber line curves and the thickness distribution as before. The thickness distribution calculations, however, differ in that a blade taper factor dependent on the radius is introduced. This factor enables the thickness of the blade to be reduced from root to tip. Such a reduction in thickness, or taper, can be used to decrease the amount of stress in the root of the blade during operation. For the present designs, the blade taper factor is chosen to result in the blade roots and tips being respectively 25% thicker and 25% thinner than the mean radius profiles.

4.9.3. Blade profile stacking axis

The blade profile of each radial station must somehow be stacked to form a three-dimensional blade surface. To minimise bending stresses on the rotating blade, the blade sections are stacked on a radial line through the sectional centre of gravity of each profile. Figure 4-9 on the next page shows how the profiles at five radial stations of a rotor blade have been stacked to create a three dimensional blade surface.
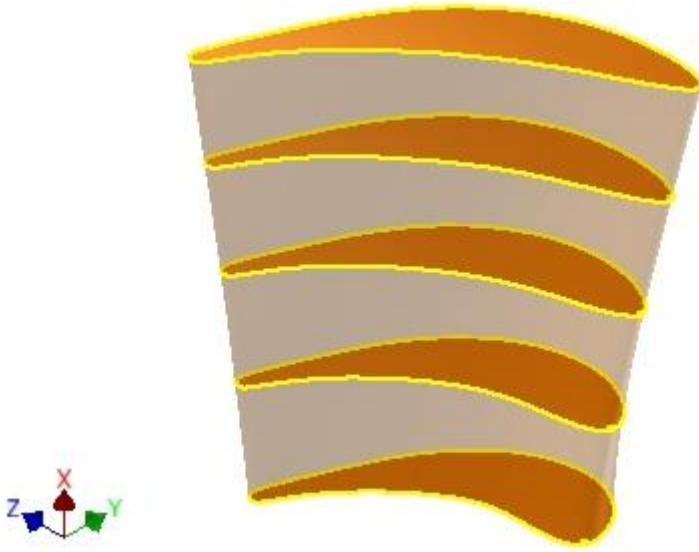
Figure 4-9: Rotor blade profile stacking

4.10.   Conclusion

This section describes the design process of a replacement turbine for an existing micro jet engine. The process for obtaining the design parameters is shown and a method for designing a turbine to meet those design parameters is presented. The method is used to generate three candidate design and these designs are subjected to an empirical performance analysis. The results of the analysis are encouraging, thus justifying further analysis of the designs.

5. CFD performance analysis of turbine stage

5.1. Introduction

The purpose of this section is to detail the CFD performance analysis employed during the turbine stage design process. A CFD analysis is used to test the feasibility of different turbine designs by generating a performance map. This map shows a prediction of the mass flow and efficiency of a turbine deign for a range of pressure ratios. Once a design is shown to be feasible, structural analysis, prototyping and experimental testing of the design can commence.

This section starts by defining the physical conditions to be simulated numerically. The parameters of the flow simulations are then discussed, detailing the computational domains, the boundary conditions, the computational mesh and the solver control parameters. Thereafter, the results of the simulations and their processing are shown and explained. Finally a conclusion regarding the simulation results is made.

5.2. Physical conditions simulated

The conditions to be simulated computationally is that of a turbine stage maintained at a constant rotational speed and being subjected to fixed inlet total conditions for different outlet static pressures. The mass flow and total-to-total efficiency resulting from the pressure difference must then be obtained. These conditions are chosen to resemble the flow conditions modelled by the empirical performance model in Section 3.

5.3. CFD methodology

5.3.1. Computational domain

Simulation of the flow conditions of an entire turbine stage is simplified by only simulating the region around one stator blade and one rotor blade. The region around each blade serves as a sub-domain of which the size is dependent on the number of blades in the particular blade row. Inlet and outlet sub-domains are also included. These additional domains allow the flow properties to gradually change from the constant value boundary conditions at the inlet and outlet planes to where interactions with the blades happen. The independence of the simulation results on the inlet and outlet domain lengths is discussed in Appendix C.1. The rotor and outlet domains rotate at the turbine rotor speed and the stator and inlet domains remain stationary. Figure 5-1 shows the computational domain for the turbine simulations. The inlet, stator, rotor and outlet domains can respectively be seen from right to left.
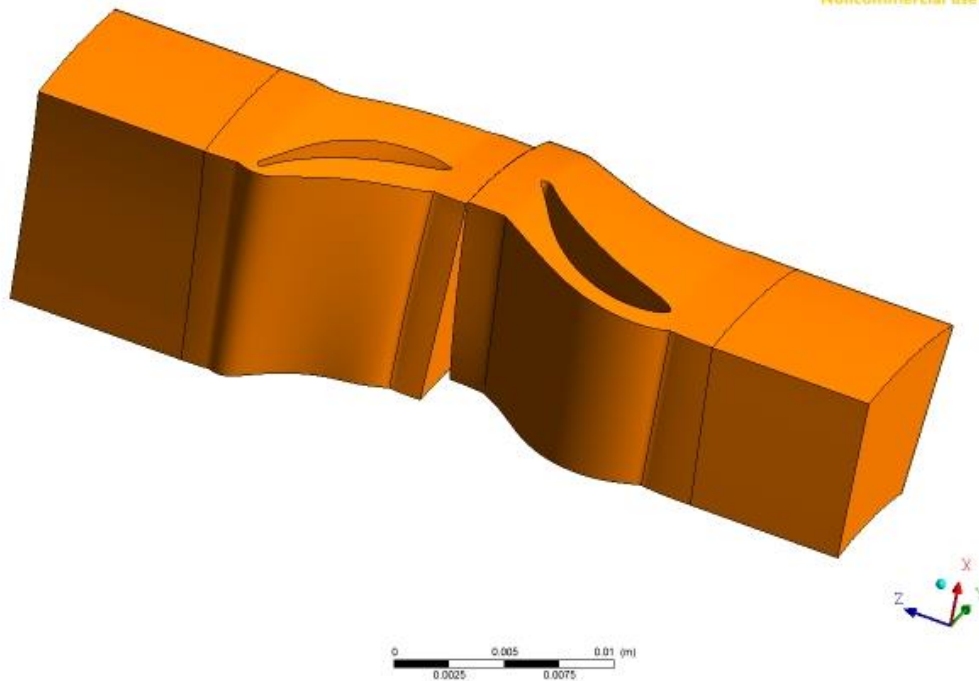
Figure 5-1: Computational domain for a turbine simulation

5.3.2. Properties of the fluid

Air, as an ideal gas, is used as the fluid occupying the computational domains in the simulations. This has also been the case for the state calculations during the empirical performance modelling and design processes.

5.3.3. Boundary conditions

The hub and shroud surfaces of the inlet and outlet domains are modelled as free-slip walls to avoid viscous losses in these sections. The surfaces of the blades, the stator hub and shroud surfaces and the rotor hub surface are all modelled as no-slip walls. The rotor shroud is modelled as a counter rotating wall, to take account of the effect of the stationary shroud in the rotating domain. The interface between the stationary and rotational domains is modelled using circumferential averaging of the total properties, otherwise known as a stage interface. However, no circumferential averaging is required at the interfaces between the inlet and stator domains or between the rotor and outlet domains. Therefore, frozen rotor interfaces are used between these domains. The inlet surface is set as a pressure inlet with the total pressure and total temperature specified. The outlet is set as a pressure outlet with the static pressure specified. These boundary conditions for the computational domain are indicated on two views of the domain in Figure 5-2.
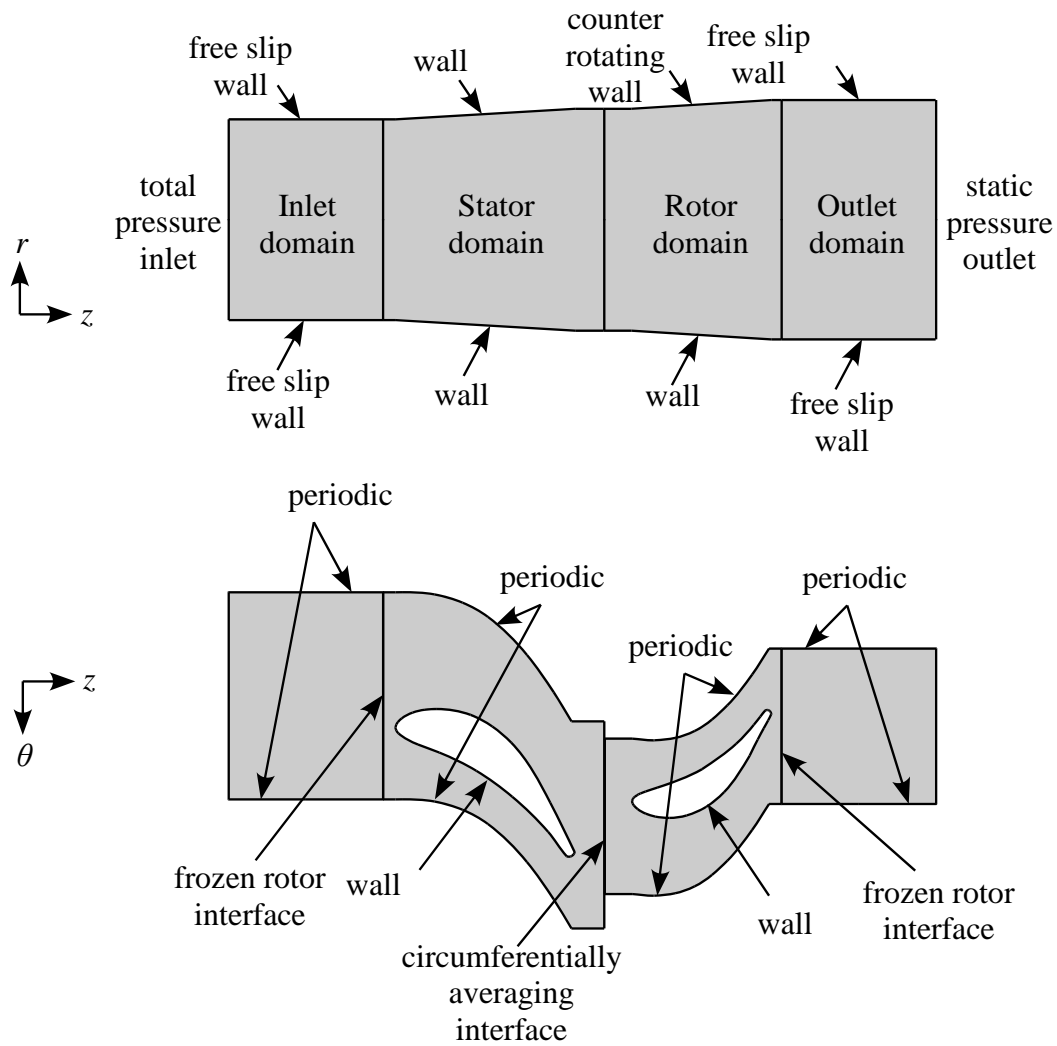
Figure 5-2: CFD boundary conditions

5.3.4. Spatial discretisation

ANSYS CFX Turbogrid is used to discretise the different computational domains into cells. The built-in optimised Automatic Topology and Meshing (ATM optimised) feature creates a structured hexahedral cell mesh that follows the geometry of the blade surfaces and is aligned with the flow direction. For each blade model the design blade Reynolds number is used to ensure acceptable wall y+ values. The blade Reynolds number for each design is obtained from the results of the empirical performance analysis at the design point. The target number of elements in the mesh is also set. The mesh independence of the flow solutions is checked and the particulars of the mesh independence study are shown in Appendix C.2. Figure 5-3 shows the mesh generated for the 105% work coefficient design stator and inlet domains. The structured nature of the mesh is clearly visible.
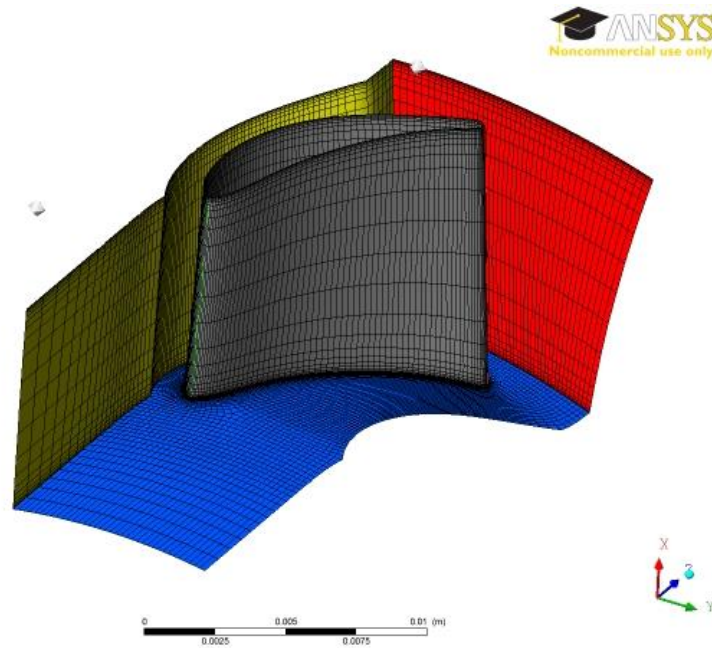
Figure 5-3: Computational mesh of the stator and inlet domains

5.3.5. Solver control parameters

The flow being modelled is steady, three-dimensional, compressible, adiabatic and turbulent. It is modelled using the ANSYS CFX turbomachinery simulation tool and solved using the ANSYS CFX solver manager. The turbulence is modelled using the k-ω shear stress transport turbulence model, since it is widely used for turbomachinery (Djouimaa, et al., 2007). The CFX high resolution scheme, a second order interpolation scheme, is used to interpolate the advection of flow properties. This is the scheme recommended by the turbomachinery simulation tool.

Convergence is controlled by firstly ensuring mesh and domain size independence as detailed in Appendix C.2. Secondly target root mean square residual values for the mass, momentum and energy conservations equations and turbulence transport equations are set to 10^{-10}.

5.4. CFD performance analysis

5.4.1. Analysis procedure

The goal of performing a CFD performance analysis on a prospective turbine design is to generate points on a turbine performance map. These points can then be compared to the corresponding curve generated by the empirical model performance analysis.

The empirical model performance analysis of Section 3 predicts the performance of a turbine design by solving the one-dimensional mean radius flow in a turbine stage for a range of total-to-static pressure ratios. The total-to-static pressure ratio is varied by keeping the inlet total pressure and total temperature constant and altering the outlet static pressure. The results of such an analysis are used to create curves of mass flow and total-to-total efficiency against total-to-total pressure ratio for a given turbine design.

The CFD performance analysis simulates the full three-dimensional flow in a turbine stage for a given set of inlet total conditions and outlet static pressure. As with the empirical performance analysis, the inlet total conditions are kept constant across multiple flow field solutions, whilst the outlet static pressure is varied between solutions. This procedure can also be used to produce performance curves similar to those generated during the empirical performance analysis. However, the solutions to full three-dimensional flow simulations take much longer to obtain than one-dimensional mean radius flow solutions. Therefore, the three-dimensional flow field is solved for only three simulations for each turbine design. These three simulations of each turbine design are labelled A, B and C; and each have a different outlet static pressure. The solution to each of these three simulations corresponds to a point on the performance maps of that specific turbine design. These points can then be compared to the curve generated by the empirical performance analysis.

A CFD performance analysis is conducted on the existing turbine design and the three new designs. The same values for the inlet total pressure and total temperature are used for all three simulations of all four designs. These values correspond to the design parameters identified in Table 4-3. Since the results of the analysis are to be plotted against total-to-total pressure ratio, similar values of this parameter are chosen for the simulations of each design. The results of the empirical performance analysis conducted in Section 4 are used to choose the outlet static pressures that result in approximate total-to-total pressure ratios of 1.4, 1.6 and 1.8 respectively. The inlet and outlet conditions for each simulation are shown in Table 5-1 on the next page.

5.4.2. CFD analysis results and discussion
The results of the CFD performance analysis of the BMT 120 KS turbine are used to create points on the turbine performance map in Figure 5-4 on the next page. The CFD results are shown as square markers against the curves resulting from the corresponding performance analysis using the empirical model (EM). The CFD analysis predicts both higher efficiencies and mass flow rates across the range of pressure ratios simulated than the empirical performance analysis.

Table 5-1: CFD performance analysis inlet and outlet conditions

Inlet total temperature, T_{t0}	1119 K		
Inlet total pressure, p_{t0}	308 kPa		
Outlet static pressure, p_3			
Turbine design	Simulation A	Simulation B	Simulation C
BMT 120 KS turbine	208 kPa	177 kPa	149 kPa
95 % work coefficient	204 kPa	174 kPa	146 kPa
100 % work coefficient	205 kPa	174 kPa	147 kPa
105 % work coefficient	205 kPa	175 kPa	149 kPa
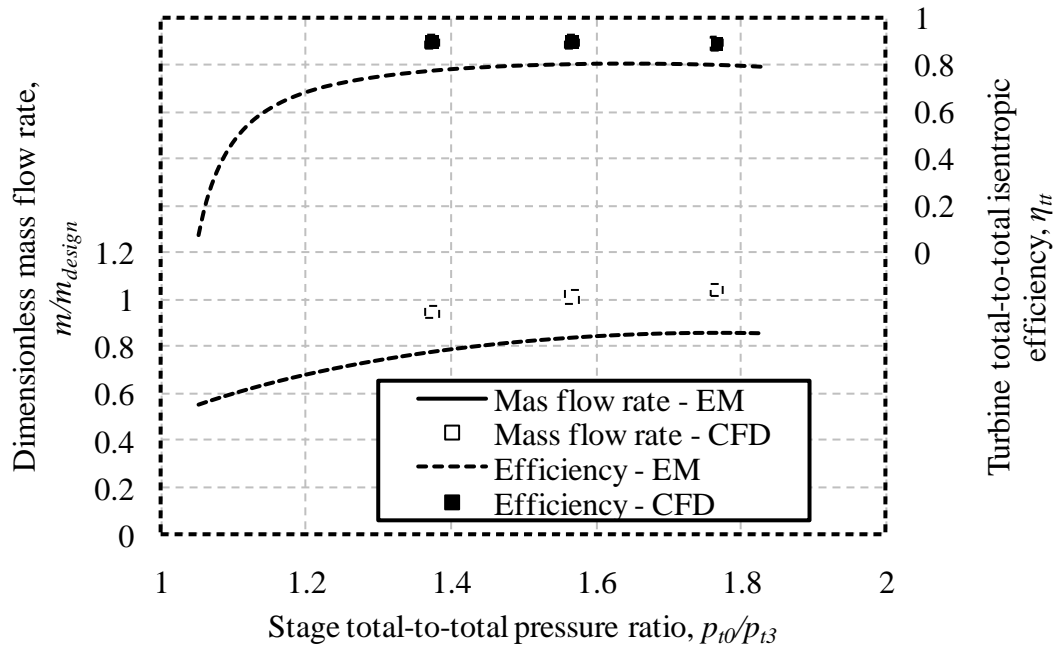
Figure 5-4: BMT 102 KS turbine

The results of the CFD performance analysis of the 95 % work coefficient turbine design are shown in Figure 5-5 on the next page. There is much better agreement between the results of the two analyses for this new design than for the BMT 120 KS turbine. The CFD performance analysis predicts very similar total-to-total stage efficiencies to those predicted by the empirical performance analysis.

However, slightly lower mass flow rates are predicted at higher total-to-total pressure ratios by the CFD analysis than the empirical performance analysis.
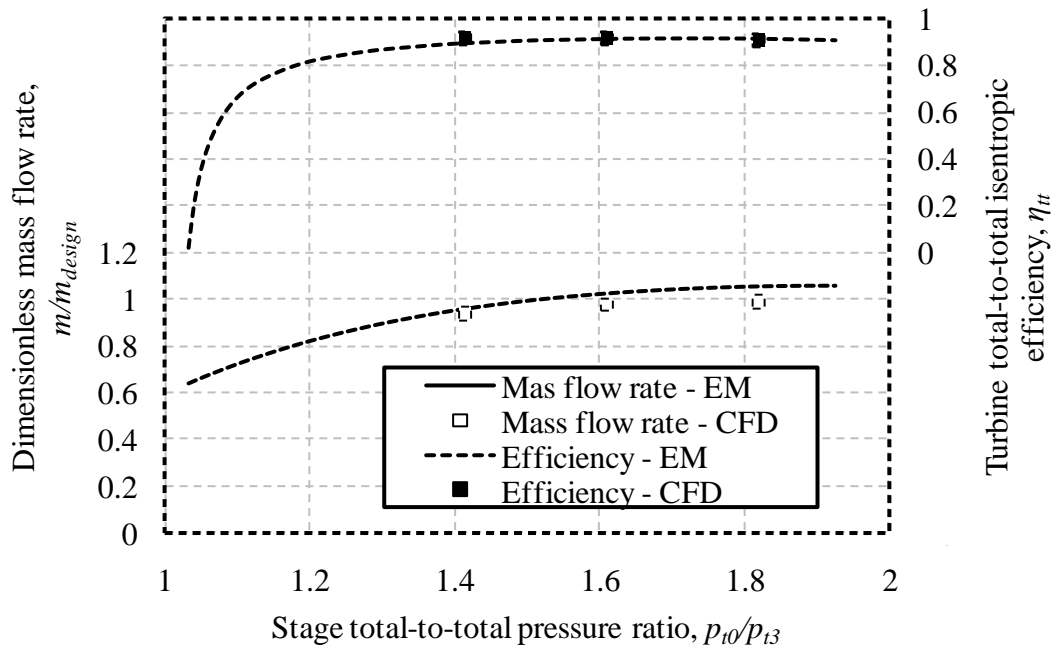
Figure 5-5: 95 % work coefficient design

Figure 5-6 on the next page shows the results of the CFD performance analysis of the 100 % work coefficient turbine design. The results of the two analyses correspond equally well to those of the 95 % work coefficient design. The CFD analysis of the 100 % work coefficient design also predicts lower mass flow rates at higher total-to-total pressure ratios than the corresponding empirical performance analysis.

Figure 5-7 on the next page provides a comparison of the results of the CFD and empirical performance analyses of the 105 % work coefficient turbine design. As with the other new designs, the results of the two analyses correspond better than for the BMT 120 KS turbine. In addition, like for the other new designs, the mass flow and the total-to-total efficiencies predicted by the CFD simulations are lower than those predicted by the empirical performance.

A general trend in the comparisons of the CFD and empirical model results for the different turbine designs can be observed. The CFD and empirical performance analyses predict quite similar results for the new turbine designs. However, the two analyses predict substantially different mass flow rates and total-to-total efficiencies for the BMT 120 KS turbine. Nevertheless, the CFD performance
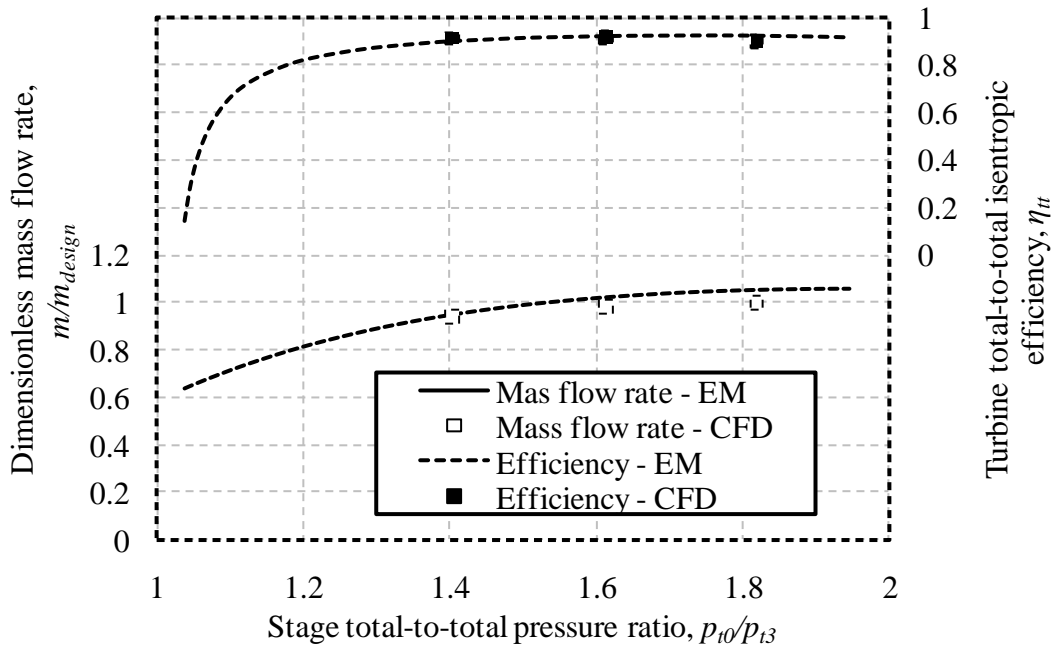
Figure 5-6: 100 % work coefficient design
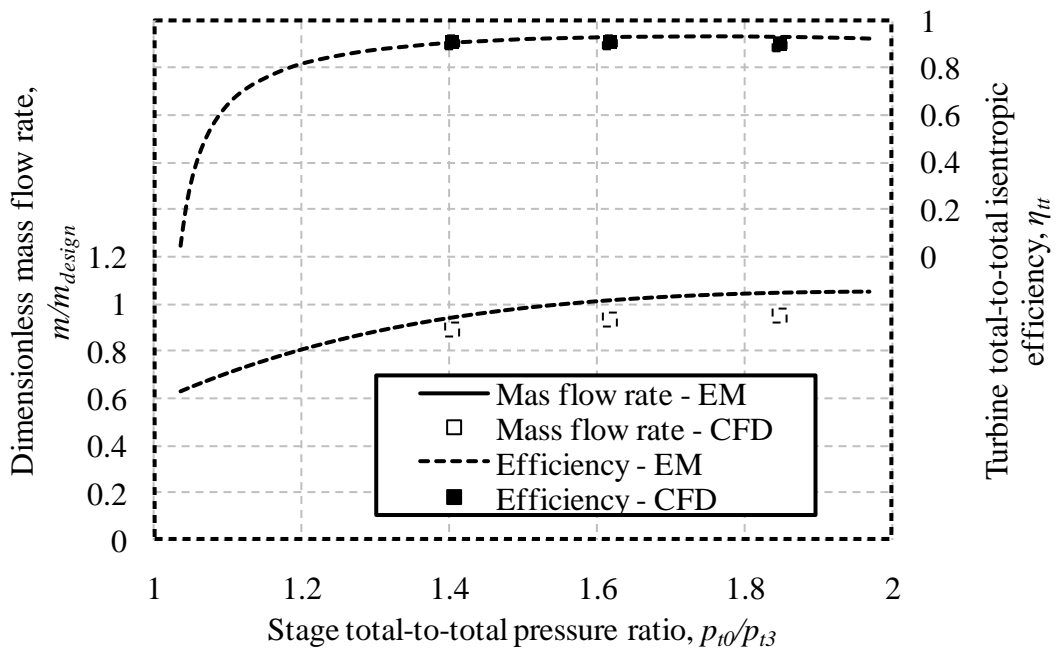
Figure 5-7: 105 % work coefficient design

analysis results of the BMT 120 KS turbine are very similar to those of the new designs. Such similarity in performance is expected, since the new designs are designed to work at either identical or very similar operating conditions to the existing turbine design. Therefore, since the convergence of the various CFD

61

simulations has also been established with some confidence, the CFD analysis is concluded to yield the more authoritative performance results. Conversely, it is then also concluded that the empirical performance analysis does not accurately predict the performance of the BMT 120 KS turbine. The empirical performance analysis procedure, however, appears to predict the performance of the new designs with more accuracy.

The empirical performance analysis procedure uses a free-vortex flow field assumption. The new turbine designs were designed to produce such a free-vortex flow field, but the BMT 120 KS turbine was not. Therefore, the difference in performance prediction accuracy suggests that the use of the empirical performance analysis procedure is limited to turbine designs with free-vortex blading.

5.5.   Conclusion

CFD performance analyses of the existing BMT 120 KS turbine and three new turbine designs are described. The CFD methodology is explained and the performance analysis procedure is described. The results of the CFD performance analysis are compared to the corresponding empirical performance analysis results for each turbine design. It is found that the two analyses yield very similar results for the new turbine designs. However, significant discrepancies between the performance results of the two analyses are found for the BMT 120 KS turbine. Since the results of the CFD performance analyses of both the existing turbine and the new designs yield the expected values, the CFD analysis procedure is concluded to be more accurate. It is also concluded that the performance analysis procedure based on empirical data only yields accurate results for turbines designed to produce free-vortex flow fields.

6.   FEM structural analysis of turbine rotor

6.1.   Introduction

A finite element method (FEM) analysis is performed on the BMT 120 KS turbine rotor and the rotors of the 95 %, 100 % and 105 % turbine designs. The purpose of the FEM structural analysis of a rotor is to determine whether it would survive the mechanical and thermal loads experienced during turbine operation.

The physical conditions to be simulated during the FEM analyses are described, along with the finite element model. A static structural analysis is conducted and a conclusion is made on the structural integrity of each rotor design. Furthermore, a modal analysis of each design is conducted. This allows the reaction of each design to cyclic excitations during operation to be evaluated.

6.2.   Physical conditions simulated

The high temperature gas flow field within the turbine stage induces a static pressures difference across the rotor blade surface. The resulting torque acts to drive the rotating engine components at a constant rotational speed. The turbine blades are therefore subjected to a bending moment due to the aerodynamic surface loading. The entire turbine rotor disc is also subject to stresses caused by the centrifugal force generated by its rotational speed. The turbine rotor disc also experiences thermal loading due to the high temperatures of the gas in the surrounding flow field. These three loading effects cause significant stresses within the turbine rotor disc and displacement of the rotor blade tips.

6.3.   FE modelling of the physical problem

6.3.1.   Geometry of the structural model

The influence of the operating conditions of a turbine can be simulated by creating a structural model of the entire turbine rotor disc. The effects of the loads experienced during operation would then be calculated for the entire turbine rotor disc structural model. However, such a structural model of the full rotor disc would consist of a number of identical sectors equal to the number of blades. Each of these sectors would experience identical loading and, therefore, identical stresses and displacements. Therefore, with the addition of the appropriate structural constraints, only one sector has to be modelled. The resulting reduction in structural model size would result in a less computationally intensive analysis. The geometry of the turbine rotor sector can be seen in Figure 6-1.

6.3.2. Material properties

The material properties given to the structural model are those of Inconel IN 713 LC, the material used in the BMT 120 KS turbine. The material properties relevant to the structural analysis are the density, the modulus of elasticity, the Poisson's ratio, the thermal expansion coefficient and the yield strength. These properties are shown in Table D-1 in Appendix D.

6.3.3. Structural constraints

The turbine rotor sector model is supported by frictionless surface supports on the two sliced surfaces. These supports constrain the blade sector circumferentially, but allow free movement in the radial direction. This configuration accurately simulates the supporting effect that the adjacent blade sectors would have in a full geometrical model simulation. To constrain any axial rigid body motion, a frictionless support is also applied to the forward-most hub surface. One of the circumferential constraints and the axial constraint can be seen in Figure 6-1 as blue surfaces.
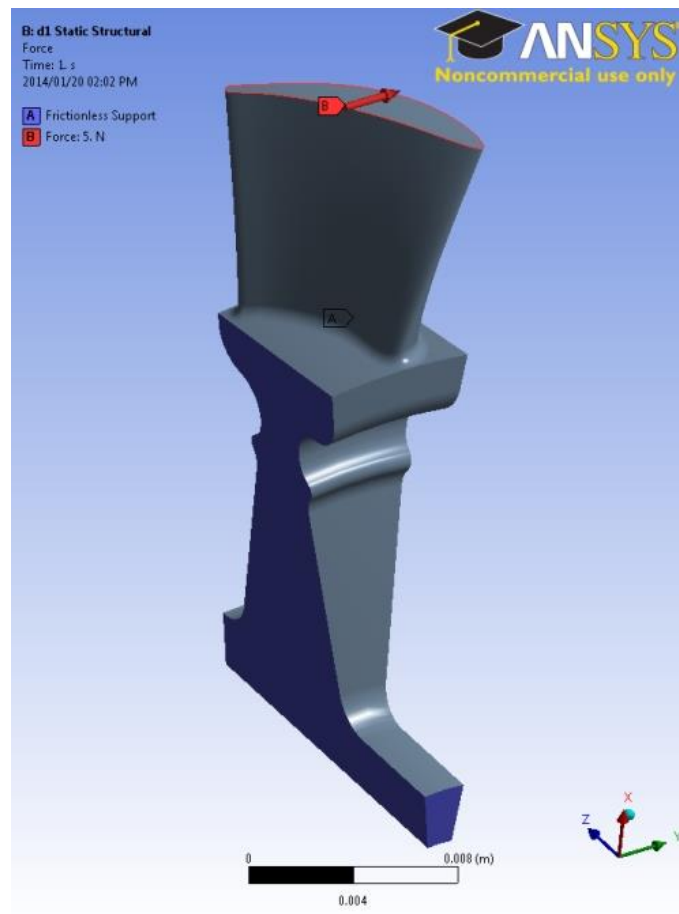
Figure 6-1: FEM model structural constraints

6.3.4. Structural loads

The turbine rotor is subjected to centrifugal, thermal and pressure loads during operation. The centrifugal load is modelled as an inertial load caused by the rotational velocity. The thermal load is modelled as constant temperature increase across the entire model. The average turbine inlet temperature at the design point as calculated by the CFD analysis is used to determine the magnitude of the temperature increase. This increase in temperature causes thermal expansion of the structural model and also influences some of the material mechanical properties. The force caused by the difference in aerodynamic pressure across the blade is modelled as a circumferential force acting on the blade tip. The magnitude of the force is specified to result in an equivalent torque to that obtained from the CFD analysis. In reality, the aerodynamic load is distributed across the length of the blade. However, applying an equivalent load at the tip of the blade results in higher bending moments at the root of the blade. Therefore, this simplification is deemed to be conservative. The circumferential tip force is shown as an arrow in Figure 6-1.

6.3.5. Structural model discretisation

The geometry of the rotor model is divided into elements using the ANSYS Workbench mechanical meshing tool. The predominantly hexahedral elements are sized to be smaller on the blade than on the hub. A mesh independence study is done to verify the mesh independence of both the static structural and the modal solutions. These studies are shown in Appendix D. The computational mesh of the 95 % work coefficient turbine design structural model is shown in Figure 6-2. The illustrated mesh has approximately 45,000 elements.
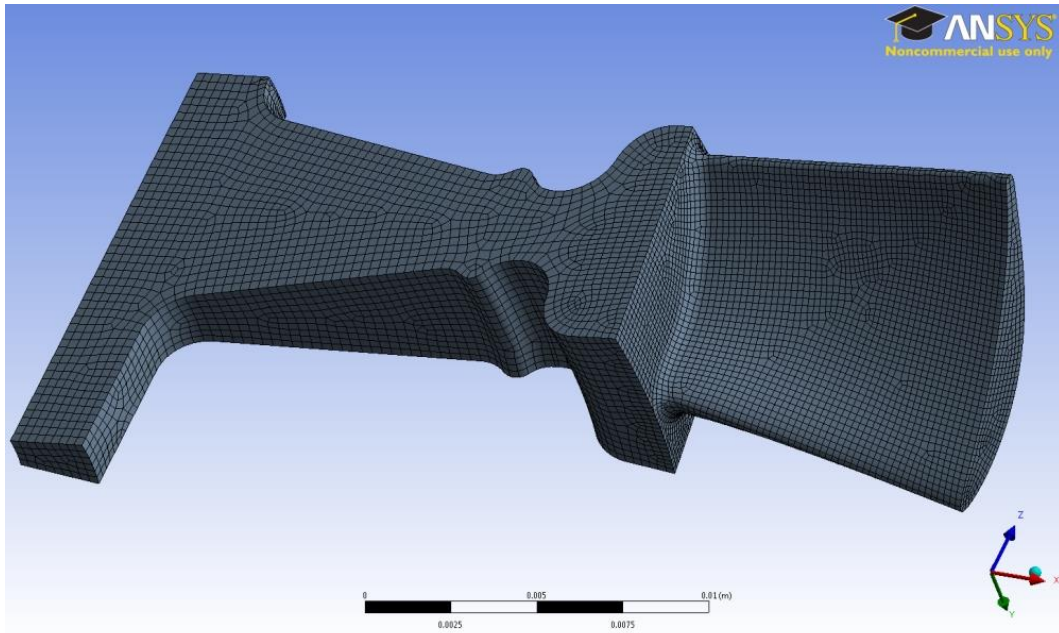
Figure 6-2: Computational mesh of the 95 % work coefficient turbine design model

6.4.   Static structural analysis

The purpose of the static structural analysis of the turbine rotor model is to determine whether the displacement of the blade tip and the blade root stresses are within allowable limits. The rotational velocity is set to match the design rotational speed of 120,000 revolutions per minute, the temperature increase is set to 707 °C and the circumferential tip force is set to 5 N. The resulting maximum tip deflections and Von-Mises blade root stresses for each design are shown in Table 6-1.

At the approximate turbine inlet temperature of 980 K the yield strength is found by linear interpolation to be 772 MPa. The simulated maximum Von-Mises blade root stresses of all the turbine designs are comfortably below this yield stress. Therefore, all the designs are deemed to satisfy the static structural strength requirements.

Table 6-1: Static structural analysis results

Turbine design	Maximum total tip deflection, mm	Maximum Von-Mises root stress, MPa
MBT 120 KS turbine	0.394	675

95 % work coefficient	0.393	702
100 % work coefficient	0.389	670
105 % work coefficient	0.391	679

6.5. Modal analysis

Excessive structural vibrations induced by unsteady wake flow are a major concern for axial-flow turbine designers (Lau, et al., 2007). This modal analysis of the turbine rotor determines whether any of the dominant excitation frequencies approach any of the turbine rotor natural frequencies as the engine is spun up to its design speed of 120,000 revolutions per minute. This analysis is conducted at the same temperature as the static structural analysis. The dominant excitation frequencies considered in the analysis are the stator blade passing frequencies encountered in one rotation and the rotational frequency. The 95 %, 100 % and 105 % turbine designs all have a prime number of stator blades. These stator blade counts are seventeen, seventeen and nineteen respectively. Therefore, only one stator passing frequency is encountered during one rotation. However, the BMT 120 KS has fifteen stator blades and therefore three passing frequencies are encountered in one rotation. The two additional frequencies are excited by every third and every fifth stator blade.

The results of the modal analyses are used to construct Campbell diagrams of the four turbine rotor designs. The results of the modal analysis of the BMT 120 KS turbine rotor are shown in Figure 6-3. The natural frequencies of the first six vibration modes are shown as markers and the dominant stator blade passing frequencies are shown as solid and dotted lines. It can be seen that the passing frequency of every third and fifth stator blade are very close to respectively the first and second natural frequencies at the design speed.
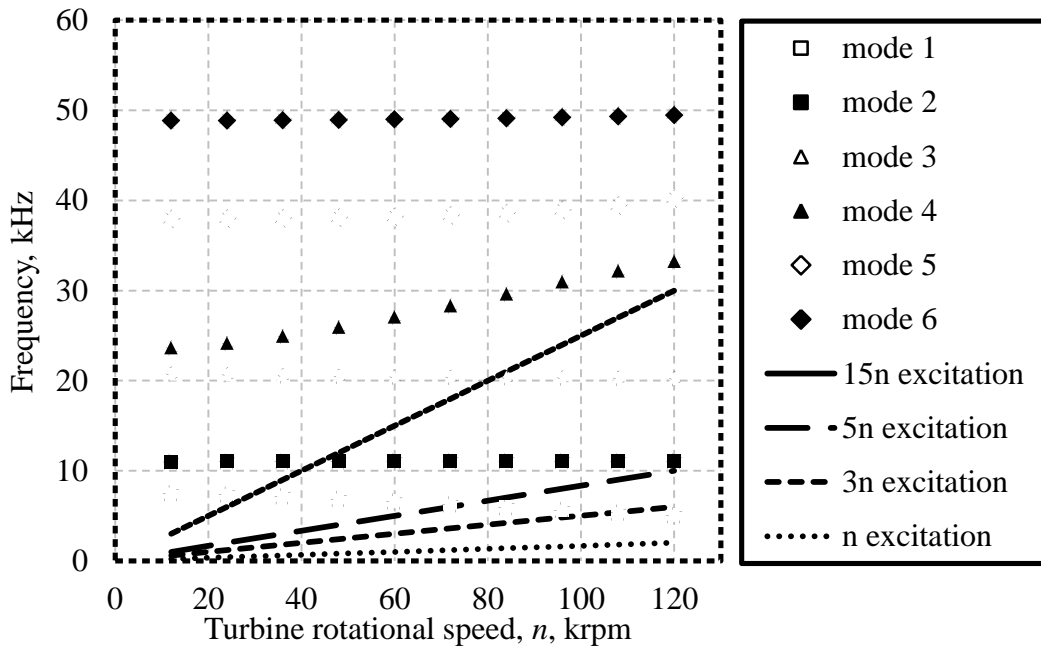
Figure 6-3: Campbell diagram of the BMT 120 KS turbine rotor

Figure 6-4 and Figure 6-5 on the next two pages show the Campbell diagrams for the 95 % and 100 % work coefficient designs respectively. The modal analysis results of these two designs are quite similar. The stator blade passing frequencies are comfortably far from all the turbine rotor blade natural frequencies at the design speed of 120,000 revolutions per minute.
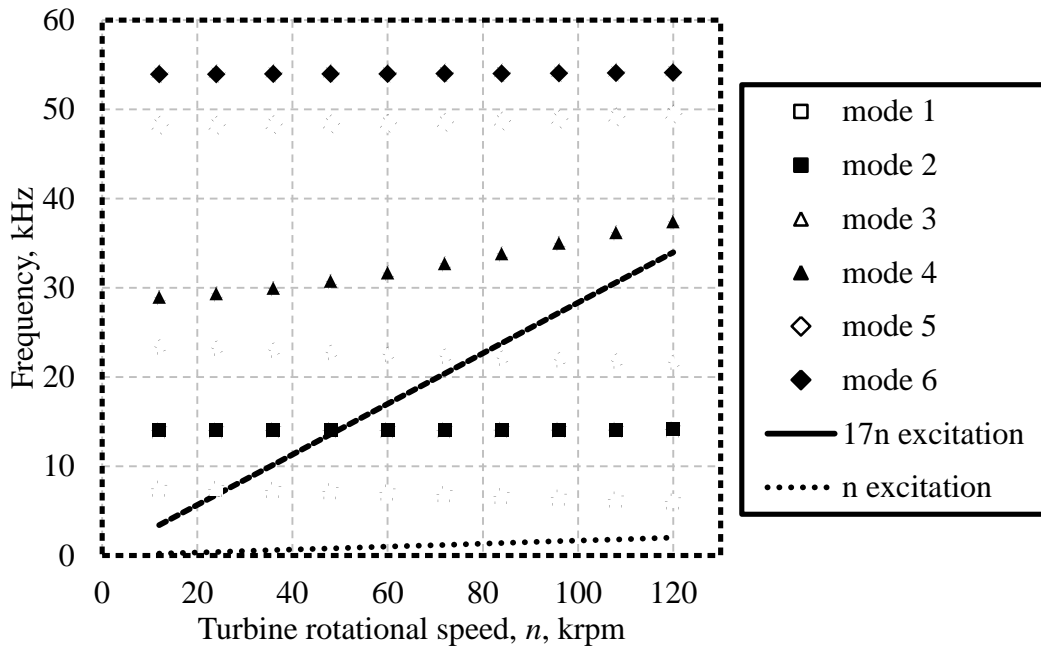
Figure 6-4: Campbell diagram of the 95 % work coefficient turbine rotor
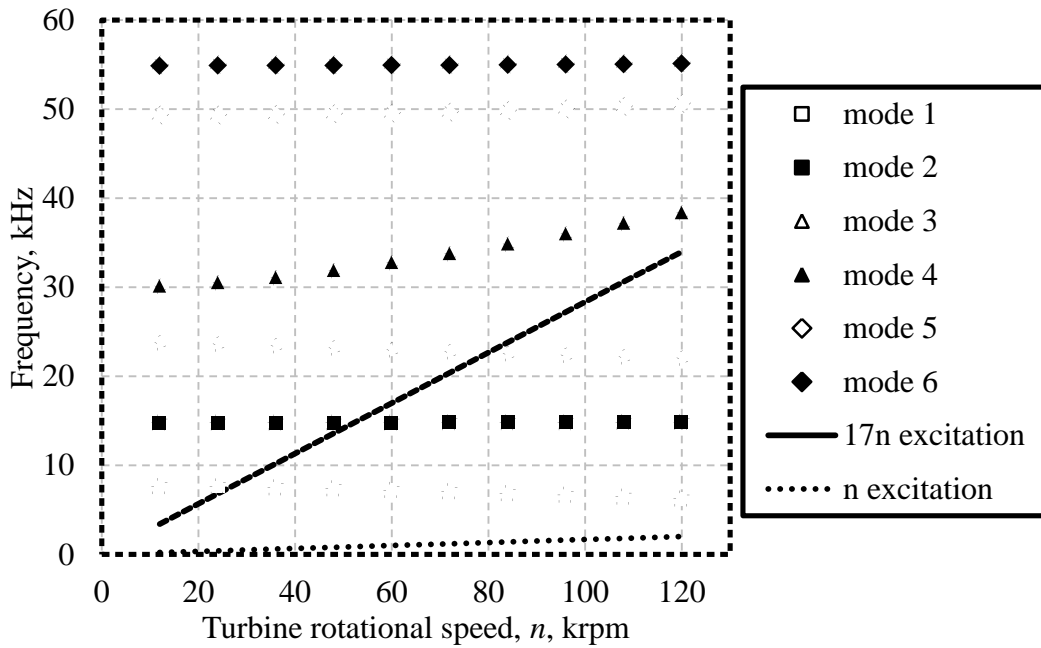
Figure 6-5: Campbell diagram of the 100 % work coefficient turbine rotor

The Campbell diagram for the 105 % work coefficient design is shown in Figure 6-6. The natural frequencies of this rotor design are very similar to those of the other two new designs. However, the larger stator blade count causes the stator blade passing frequency to be slightly higher. This increase brings the stator blade

69

passing frequency close to the natural frequency of the fourth mode at the design speed. This might cause structural resonance, resulting in higher than normal displacements during operation at the design speed.
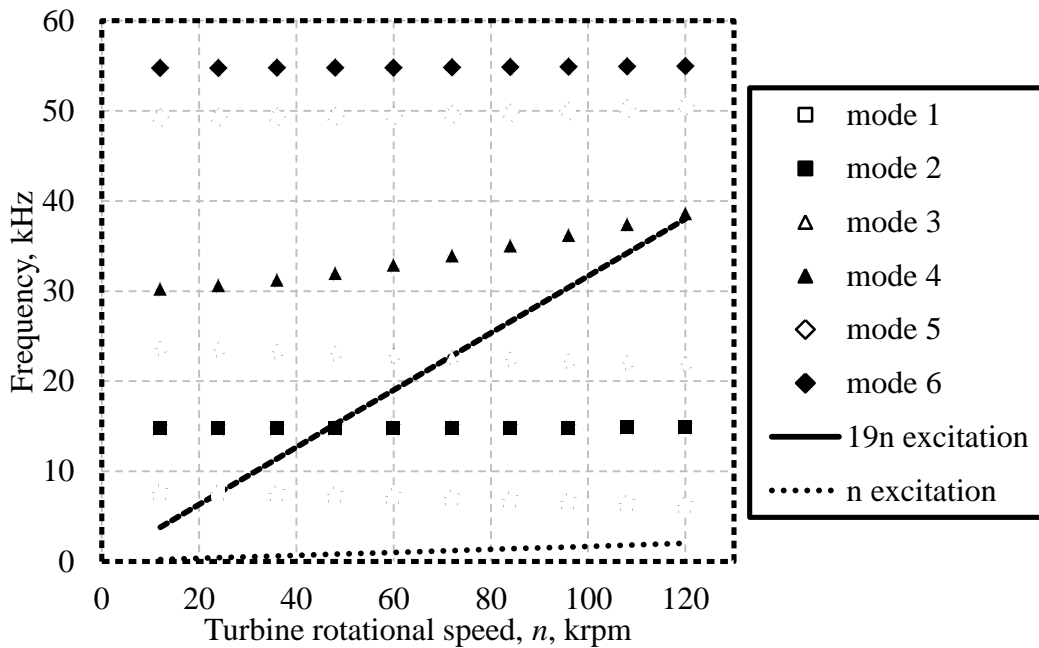
Figure 6-6: Campbell diagram of the 105 % work coefficient turbine rotor

6.6.   Conclusion

The static structural and modal analyses of the BMT 120 KS turbine rotor and the rotors of the three new designs are described. The FEM methodology is detailed and the analysis methods are described. It is found that none of the rotors experience excessively high root stresses during static loading. The results of the modal analysis, however, suggest that both the BMT 120 KS turbine rotor and the rotor of the 105 % work coefficient design would encounter structural resonance when operating at or near the design speed. However, since only the fourth most prominent natural frequency of the 105 % work coefficient design is excited, the resulting displacements would likely not be unacceptably high.

7. Turbine prototype manufacturing process

7.1. Introduction

New turbine designs were generated using the turbine design procedure and analysed using numerical and empirical procedures. Prototypes of these new designs are required for use in experimental testing. An investment casting process is utilised for manufacturing these prototypes. This process is chosen because it allows each turbine component to be created as a single casting that is close to the desired final shape. Additionally, when using an investment casting process, the geometries of the turbine blades are not limited by the machinability of the material or constricted by tooling access.

This section describes the process followed to create the prototypes of the turbine components. Firstly, the appropriate material for the prototypes is selected and three-dimensional models of the desired final geometries are generated. The final geometries are then modified for the casting process by taking account of shrinkage and by adding machining allowances. These modified component geometries are used to create the sacrificial patterns and the investment casting process is performed. The results of the investment casting process are discussed and some concluding remarks are made.

7.2. Material selection

The high operating temperatures and mechanical stresses encountered in turbine blades necessitate the use of high temperature super-alloys. The BMT 120 KS turbine is manufactured from Inconel IN713LC, a nickel-based super-alloy. As is shown in Table D-1 in Appendix D.1, the yield strength and modulus of elasticity of IN713LC are sufficiently high at the temperatures encountered in the turbine stage. IN713LC also has the added benefit of not requiring heat treatment after the casting process. Therefore, IN713LC is selected to be the material for the new turbine.

7.3. Required final component geometries

The prototypes of the new turbine rotor and stator components are to be used in an un-modified BMT 120 KS jet engine. Therefore, the mounting surfaces of the new components must be identical to those on the existing BMT 120 KS turbine components. The turbine rotor hub has a central hole that slips over the jet engine shaft. It is secured to the shaft by a nut tightened against the back of the hub to press an extended front shoulder against the shaft bearing. The turbine stator is attached to the tunnel of the engine by six machine screws through holes in a

flange. The axial position of both the stator flange and the rotor hub shoulder relative to the leading edge of the stator blades also correspond to the distances in the BMT 120 KS turbine. The outer surface of the stator shroud is also shaped to fit inside the combustion chamber exhaust at the front and the engine housing at the back.

7.4. Modification of desired final component geometries

The required final component geometries are modified for the manufacturing process. These modifications are used to provide machining allowances and facilitate the flow of the molten nickel alloy through the mould during the investment casting process. Due to the shrinkages of solidifying metal, a casting is smaller than its associated wax pattern (Dong, et al., 2011). Therefore, the modified geometries are scaled up volumetrically by 1.5 % to take account of the shrinkage of the molten nickel alloy upon solidification. Figure 7-1 shows the desired stator geometry (left) and the modified stator geometry (right). The volumetric size increase can't be clearly seen on this scale, but the machining allowance added to the outer surface of the shroud can be seen. In the modified model, the flange is extended to the centre, where it connects to a shoulder. This shoulder is used for the connection of the component patterns to the casting risers.

Figure 7-1: Stator final (left) and casting (right) geometries

7.5. Pattern creation

Three-dimensional printers are used to grow the investment casting patterns one layer of material at a time. Two different printing systems, each characterised by the use of a distinct material, are used for growing the patterns. The one system employs an EOSINT P380 that grows three-dimensional geometries by laser-sintering powdered layers of PrimeCast 101, a polystyrene material. The other system uses a Solidscape 3Z Pro printer to grow parts by expelling a jet of micro droplets of a Solidscape 3Z Model, a wax-like organic compound.

7.5.1. PrimeCast 101 system

The EOSINT P380 creates three-dimensional models by selectively laser-sintering multiple layers of PrimeCast 101 powder. The powder is low cost, with the bulk of the production cost being related to the production duration. Therefore, since the EOSINT P380 has the capacity to grow multiple parts simultaneously, the patterns of multiple different turbine designs could be grown inexpensively.

An example of a turbine rotor pattern generated using the PrimeCast 101 system is shown in Figure 7-2. The part can be seen to have a rough surface finish, with a significant stepping effect on the hub surface being visible. Furthermore, the feature creation resolution appears to be coarse, as is visible on the blade jagged trailing edges. The PrimeCast 101 model is also fairly brittle, resulting in the chipping of the blade tips during transportation.
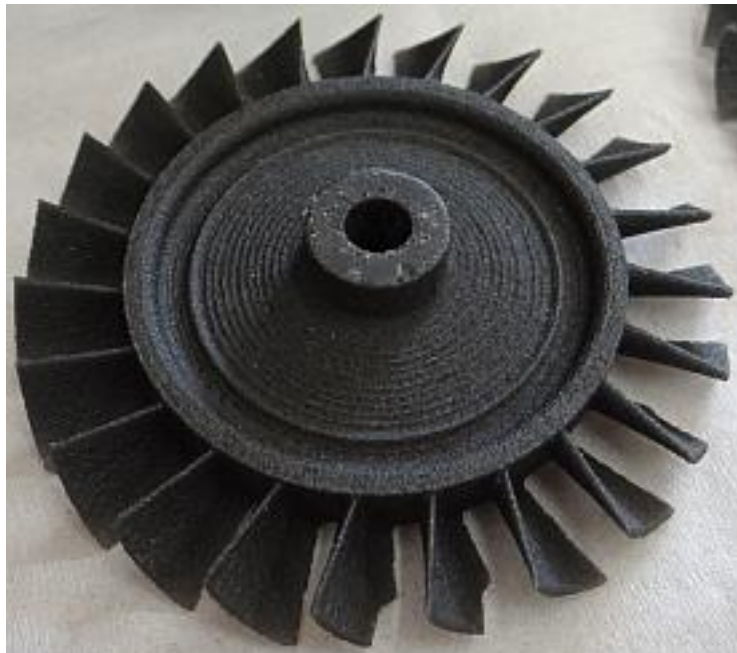
Figure 7-2: PrimeCast 101 rotor pattern

7.5.2. Solidscape 3Z Model system

The Solidscape 3Z Pro creates three-dimensional models by expelling a high frequency jet of Solidscape 3Z Model micro droplets. The jet is precision controlled and can be used to reproduce intricate geometries and smooth surfaces. The Solidscape 3Z Model material is more expensive than the PrimeCast 101 material and the Solidscape 3Z Pro has the capacity to grown only one part at a time. Due to these two factors, a Solidscape 3Z Model part is about seventy times more expensive to produce than an equivalent PrimeCast 101 part.

An example of a turbine rotor pattern generated using the Solidscape 3Z Model system is shown in Figure 7-3. The part can be seen to have a much smoother surface finish than the comparable PrimeCast 101 pattern, with a no visible stepping effect on the smooth surfaces. The printing resolution is also suitably high for accurately producing the thin blade trailing edges.

Figure 7-3: Solidscape 3Z Model rotor pattern

7.6.   Investment casting process

The sacrificial component patterns are assembled using sections of wax rod. These assemblies are then repeatedly dipped in ceramic slurry and dried, thus building a substantial ceramic shell. The patterns with the encasing ceramic shell are then placed in an oven where the patterns are burned out, thus leaving only the ceramic shell mould.

During this mould firing process, the two different pattern materials behave differently. The Solidscape 3Z Model melts upon firing, whereas the PrimeCast 101 vaporises. This vaporisation of the PrimeCast 101 causes a pressure build-up in the constricted passages present in the stator shroud moulds. Consequently, the stator shell moulds that are created around PrimeCast 101 patterns break apart during the mould firing process. Figure 7-4 shows one such a broken shell mould. It is therefore found that the more expensive Solidscape 3Z Model patterns are required for casting the shrouded turbine stator components.

Figure 7-4: Ceramic mould destroyed by firing PrimeCast 101 stator patterns

Once the ceramic moulds have been fired, the molten IN713LC is poured into the mould under vacuum conditions. The vacuum conditions prevent oxides and other impurities from being included in the molten metal alloy. Once poured, the alloy is allowed to cool, where after the ceramic mould is broken and cleaned off.

7.7.   Investment casting results

The investment casting process is performed using two different pattern materials, PrimeCast 101 and Solidscape 3Z Model. Both model materials proved capable of producing the unshrouded turbine rotor castings. Examples of the rotor castings produced using these PrimeCast 101 and Solidscape 3Z Model are shown in Figure 7-5 and Figure 7-6 respectively. The superior surface finish and feature reproduction of the Solidscape 3Z Model castings is clearly visible.

Figure 7-5: Rotor casting made using a PrimeCast 101 pattern

Figure 7-6: Rotor casting made using a Solidscape 3Z Model pattern

Only the Solidscape 3Z Model patterns resulted in usable shrouded stator moulds. An example of a turbine stator, cast using a Solidscape 3Z Model pattern, is shown in Figure 7-7. The surface finish and feature reproduction are similar to those of the turbine rotor castings that used the same pattern material.

76

Figure 7-7: Stator casting made using a Solidscape 3Z Model pattern

7.8.   Conclusion

This section describes the investment casting procedure used to created functional prototypes of the new turbine designs. The material and geometry of the final components are chosen and these geometries are modified for the casting process.

Two pattern materials, PrimeCast 101 and Solidscape 3Z Model, were used in making the ceramic shell moulds. It was found that the PrimeCast 101 patterns resulted in inferior turbine rotor castings. The turbine stator patterns grown from PrimeCast 101 were also found to be completely unsuitable for the mould making process.

The casting process was completed using all the viable moulds and some examples or the resulting castings are shown. It is clear from the photographs that the castings resulting from Solidscape 3Z Model patterns are vastly superior to those resulting from PrimeCast 101 patterns. This improvement in casting quality does, however, come at a substantial increase in pattern cost.

8.   Conclusion

The purpose of this thesis is to document the proposed methodology for designing axial-flow turbines for use in small jet engines. The resulting methodology would complement similar research done on the development of centrifugal compressors.

8.1.   Development and implementation of the design methodology

At the outset of this project the design methodology was divided up into six sections, each meant to address one of the project objectives. The following paragraphs present a summary of the methods used and the results obtained in each section. Reference is also made to how each section addresses a particular project objective.

In Section 2 the geometries of existing turbine components are reverse engineered to allow for a comparative analysis with new turbine designs. The shapes of the turbine stator and rotor are digitised using a CT-scanner and a CMM respectively. The procedure for processing the raw point cloud data obtained from the two measurement devices is described and renderings of the resulting reconstructed three-dimensional models are shown. These three-dimensional models can be used in a CFD analysis of the existing turbine and can also be readily parameterised for use in an empirical performance analysis procedure. The models of the existing turbine can therefore be used as a baseline design and serve to meet the first project objective.

Section 3 details a mean radius performance analysis procedure using empirical loss correlations. The empirical loss model is described and a proposal for an analysis procedure for calculating the performance of a turbine under specified conditions is made. This procedure is applied to an existing turbine design and a turbine performance map is generated. This performance map compares well with the trends shown in similar charts in literature, even though the mass flow rate is under predicted. This empirical loss model performance analysis procedure serves as one of independent performance analysis procedures required to partially meet the third project objective.

In Section 4 the design process of a replacement turbine for an existing micro jet engine is described. The process for obtaining the design parameters is shown and a method for designing a turbine to meet those design parameters is presented. The method is used to generate three candidate designs, which are then subjected to the empirical performance analysis detailed in Section 3. The results of the analysis are encouraging, suggesting suitably high efficiencies and mass flow rates for the new designs. Therefore, further analysis of the new designs is

deemed justified. Since this design process is shown to be able to generate viable turbine designs, the second project objective is deemed to be met.

CFD performance analyses of the existing BMT 120 KS turbine and three new turbine designs are described in Section 5. The CFD methodology is detailed and the performance analysis procedure is described. The results of the CFD performance analysis are compared to the corresponding empirical performance analysis results for each turbine design. It is found that the two analyses yield very similar results for the new turbine designs. However, significant discrepancies between the performance results of the two analyses are found for the BMT 120 KS turbine. Since the results of the CFD performance analyses of both the existing turbine and the new designs yield the expected values, the CFD analysis procedure is concluded to be more accurate. This CFD performance analysis procedure serves as a second independent procedure, and therefore the third objective is fully met.

The static structural and modal analyses of the BMT 120 KS turbine rotor and the rotors of the three new designs are described in Section 6. The FEM methodology is detailed and the analysis methods are described. It is found that none of the rotors experience excessively high root stresses during static loading. The results of the modal analysis suggest that the BMT 120 KS turbine rotor and the rotor of the 105 % work coefficient design would have natural frequencies excited at or near the design speed. These are, however, not the primary natural frequencies, so excessive blade deflections are not expected. This structural analysis procedure serves to meet the fourth project objective.

Section 7 describes the investment casting procedure used to create functional prototypes of the new turbine designs. IN 713 LC is chosen as the material for the prototypes, and the geometries of the different components are modified to make provisions for the casting process. Two pattern materials, PrimeCast 101 and Solidscape 3Z Model, are used in making the ceramic shell moulds. It was found that the PrimeCast 101 patterns result in inferior turbine rotor castings. The turbine stator patterns grown from PrimeCast 101 are also found to be unsuitable for the mould making process. The casting process is completed using all the viable moulds and some examples or the resulting castings are shown. It is clear from the photographs that the castings resulting from Solidscape 3Z Model patterns feature substantially better surface finish and thin edge reproduction compared to those resulting from PrimeCast 101 patterns. Future experimental analysis of the different castings may indicate whether the additional cost of using Solidscape 3Z Model patterns is justified. Since this manufacturing process

successfully produced turbine prototype castings, the fifth project objective is deemed as met.

8.2.   Suggestions for future research

The present project focussed on the design process as a whole. Consequently, in depth studies of each of the design steps were not possible. Therefore, there is an opportunity for research into each of the design steps individually. A CFD investigation into the effect of different turbine stage work coefficients on the flow field would be especially helpful.

Since this project excluded the final machining of the cast turbine prototypes, and also the experimental testing of the new designs, these tasks remain as scope for a future project. An experimental investigation into the difference in the performance of turbine castings made using PrimeCast 101 patterns and castings made using Solidscape 3Z Model patterns would also shed light on the necessity of using expensive pattern materials.

When the results of the present project are seen in the context of the greater Ballast project, an important perspective is gained. Clearly an opportunity exists for developing a new turbine and a new centrifugal compressor to be used together in a micro jet engine.

Appendix A: Empirical performance model calculations

A.1. BMT 120 KS turbine stator blade row total pressure loss coefficient sample calculation

The total pressure loss coefficient of the BMT 120 KS turbine stator blade row is dependent on the parameters listed in Table A-1 and is calculated using equation (3.2) (Aungier, 2006):

$$Y = Y_{TE} + Y_p + Y_s + Y_{CL} + Y_{SH} = 0{,}131 \tag{A-1}$$

Table A-1: BMT 120 KS turbine stator blade row empirical performance model inlet parameters

Blade parameters		Flow field parameters	
β_{b0}	96,81°	α'_{b0}	90°
β_g	28,34°	α'_{b1}	32,1°
b_z	10,8 mm	W_1	321 m/s
c	14,0 mm	M'_0	0,23
s	11,6 mm	M'_1	0,49
s/c	0,825	ρ_1	0,833 kg/m^3
R_c	33,1 mm	μ_1	4,4(10)$^{-5}$ kg/m/s
t_{max}	2 mm		
t_{TE}	0,9 mm		
e	0,05 mm		
h	10,1 mm		
δ	0 mm		

The calculations for the different loss coefficients in equation (A-1) are now shown.

A.1.1. Trailing edge loss coefficient calculation

The trailing edge loss coefficient is calculated using equation (3.3):

$$Y_{TE} = \left(\frac{t_{TE}}{s \sin \beta_g - t_{TE}} \right)^2 = 0{,}0376 \tag{A-2}$$

A.1.2. Profile loss coefficient calculation

The profile loss coefficient is calculated using equation (3.4) (Aungier, 2006):

$$Y_p = K_{mod} \, K_{inc} \, K_M \, K_p \, K_{RE} \left(\left(Y_{p1} + \xi^2 \left(Y_{p2} - Y_{p1} \right) \right) \left(5 \frac{t_{max}}{c} \right)^\xi - \Delta Y_{TE} \right)$$
$$= 0{,}0246 \tag{A-3}$$

The calculation of the different factors and terms used in equation (A-3) are now shown.

Nozzle blade and impulse blade profile loss coefficient calculation

The gas deflection ratio is calculated using equation (3.5):

$$\xi = \frac{90° - \beta_{b0}}{90° - \alpha'_{b1}} = -0,118 \tag{A-4}$$

The ideal nozzle blade and impulse blade pitch-to-chord ratios are given by equation (A-5) and equation (A-6) respectively (Aungier, 2006):

$$(s/c)_{min,1} = 0,427 + \frac{\alpha'_{b1}}{58°} - \left(\frac{\alpha'_{b1}}{93°}\right)^2 = 0,862 \tag{A-5}$$

$$(s/c)_{min,2} = 0,224 + \left(1,575 - \frac{\alpha'_{b1}}{90°}\right)\left(\frac{\alpha'_{b1}}{90°}\right) = 0,659 \tag{A-6}$$

The nozzle blade and impulse blade profile loss coefficients are given by equations (A-7) to (A-12) and equation (A-13) to (A-17) respectively (Aungier, 2006):

$$X_{p1} = (s/c) - (s/c)_{min1} = -0,0365 \tag{A-7}$$

$$A_{p1} = \begin{cases} 0,025 + \dfrac{27° - \alpha'_{b1}}{530°}, & \alpha'_{b1} \leq 27° \\ 0,025 + \dfrac{27° - \alpha'_{b1}}{3085°}, & \alpha'_{b1} > 27° \end{cases} = 0,0233 \tag{A-8}$$

$$B_{p1} = 0,1583 - \frac{\alpha'_{b1}}{1640°} = 0,139 \tag{A-9}$$

$$C_{p1} = 0,08\left[\left(\frac{\alpha'_{b1}}{30°}\right)^2 - 1\right], \qquad \alpha'_{b1} \leq 30° \tag{A-10}$$

$$n_{p1} = 1 + \frac{\alpha'_{b1}}{30°}, \qquad \alpha'_{b1} > 30° = 2,07 \tag{A-11}$$

$$Y_{p1} = \begin{cases} A_{p1} + B_{p1} X_{p1}^2 + C_{p1} X_{p1}^3, & \alpha'_{b1} \leq 30° \\ A_{p1} + B_{p1}|X_{p1}|^{n_{p1}}, & \alpha'_{b1} > 30° \end{cases} = 0,0235 \tag{A-12}$$

$$X_{p2} = (s/c) - (s/c)_{min2} = 0,166 \tag{A-13}$$

$$A_{p2} = 0,242 - \frac{\alpha'_{b1}}{151°} + \left(\frac{\alpha'_{b1}}{127°}\right)^2 = 0,0932 \tag{A-14}$$

$$B_{p2} = \begin{cases} 0{,}3 + \dfrac{(30° - \alpha'_{b1})}{50°}, & \alpha'_{b1} \leq 30° \\[2mm] 0{,}3 + \dfrac{(30° - \alpha'_{b1})}{275°}, & \alpha'_{b1} > 30° \end{cases} = 0{,}292 \tag{A-15}$$

$$C_{p2} = 0{,}88 - \frac{\alpha'_{b1}}{42{,}4°} + \left(\frac{\alpha'_{b1}}{72{,}8°}\right)^2 = 0{,}317 \tag{A-16}$$

$$Y_{p2} = A_{p2} + B_{p2}\, X_{p2}^2 - C_{p2}\, X_{p2}^3 = 0{,}0998 \tag{A-17}$$

Off-design incidence angle correction factor calculation

The incidence angle is calculated using equation (3.7):

$$i = \beta_{b0} - \alpha'_{b0} = 6.81° \tag{A-18}$$

The gas deflection ratio dependent part of the stalling incidence angle is calculated using equation (A-19) to equation (A-24) (Aungier, 2006):

$$i_{s0} = 20° - \left(\frac{\xi + 1}{0{,}11}\right)° = 12° \tag{A-19}$$

$$A_{sr} = A_{sr}(\alpha'_{b1}) = 61{,}8° - \left(1{,}6° - \frac{\alpha'_{b1}}{165°}\right)\alpha'_{b1} = 16{,}6° \tag{A-20}$$

$$B_{sr} = B_{sr}(\alpha'_{b1}) = 71{,}9° - 1{,}69\alpha'_{b1} = 17{,}6° \tag{A-21}$$

$$C_{sr} = C_{sr}(\alpha'_{b1}) = 7{,}8° - \left(0.28 - \frac{\alpha'_{b1}}{320°}\right)\alpha'_{b1} = 2{,}03° \tag{A-22}$$

$$D_{sr} = D_{sr}(\alpha'_{b1}) = 14{,}2° - \left(0{,}16 + \frac{\alpha'_{b1}}{160°}\right)\alpha'_{b1} = 2{,}6° \tag{A-23}$$

$$i_{sr}(\alpha'_{b1}, \xi) = \begin{cases} i_{s0} + A_{sr} - B_{sr}\,\xi^2 + C_{sr}\,\xi^3 + D_{sr}\,\xi^4, & \alpha'_{b1} \leq 40° \\[2mm] i_{s0} + \left|\dfrac{55° - \alpha'_{b1}}{15°}\right| |i_{sr}(40°, \xi) - i_{s0}|, & \alpha'_{b1} > 40° \\[2mm] = 28{,}4° \end{cases} \tag{A-24}$$

The pitch-to-chord ratio stalling incidence angle correction is calculated using equation (3.9) and (3.10):

$$X_{is} = s/c - 0{,}75 = 0{,}0752 \tag{A-25}$$

$$\Delta i_s = \begin{cases} -38° \, X_{is} - 53,5° \, X_{is}^2 - 29° \, X_{is}^3, & s/c \le 0,8 \\ -2,0374° - (s/c - 0,8)\left[69,58° - 1°\left(\dfrac{\alpha'_{b1}}{14,48°}\right)^{3,1}\right], & s/c > 0,8 \end{cases} \quad \text{(A-26)}$$
$$= -3,49°$$

The stalling incidence angle is calculated using equation (3.8) and the incidence angle-to-stalling incidence angle ratio is given by equation (A-28):

$$i_s = i_{sr} + \Delta i_s = 24,9° \tag{A-27}$$

$$(i/i_s) = i/i_s = 0,274 \tag{A-28}$$

The off-design incidence correction factor is calculated using equation (3.11**Error! Reference source not found.**):

$$K_{inc} = \begin{cases} -1,39214 - 1,90738(i/i_s), & (i/i_s) < -3 \\ 1 + 0,52(i/i_s)^{1,7}, & -3 \le (i/i_s) < 0 \\ 1 + (i/i_s)^{2,3+0,5(i/i_s)}, & 0 \le (i/i_s) < 1,7 \\ 6,23 - 9,8577[(i/i_s) - 1,7], & 1,7 \le (i/i_s) \end{cases} = 1,04 \tag{A-29}$$

Mach number correction factor calculation
The Mach number correction factor is calculated using equation (3.12) (Aungier, 2006):

$$K_M$$
$$= \begin{cases} 1, & M'_1 \le 0,6 \\ 1 + [1,65(M'_1 - 0,6) + 240(M'_1 - 0,6)^4]\left(\dfrac{s}{R_c}\right)^{3M'_1 - 0,6}, & 0,6 < M'_1 < 1 \\ 1, & 1 \le M'_1 \end{cases} \tag{A-30}$$
$$= 1$$

Compressibility correction factor calculation
The compressibility correction factor is calculated using equations (3.13) to (3.17) (Aungier, 2006):

$$\widetilde{M}'_0 = 0,5(M'_0 + 0,566 - |0,566 - M'_0|) = 0,23 \tag{A-31}$$

$$\widetilde{M}'_1 = 0,5(M'_1 + 1 - |M'_1 - 1|) = 0,493 \tag{A-32}$$

$$X_p = \frac{2\widetilde{M}'_0}{\widetilde{M}'_0 + \widetilde{M}'_1 + |\widetilde{M}'_1 - \widetilde{M}'_0|} = 0,467 \tag{A-33}$$

$$K_1 = 1 - 0,625(\widetilde{M}'_1 - 0,2 + |\widetilde{M}'_1 - 0,2|) = 0,633 \tag{A-34}$$

$$K_p = 1 - (1 - K_1)X_p^2 = 0,92 \tag{A-35}$$

Reynolds number correction factor calculation

The chord-based, roughness height based, laminar and transition Reynolds numbers are calculated using equations (A-36) to (A-39) respectively (Aungier, 2006):

$$Re_c = \frac{\rho_2 W_2 c}{\mu_2} = 85\ 300 \quad \text{(A-36)} \qquad Re_{lam} = 1(10)^5 \tag{A-37}$$

$$Re_r = 100\frac{c}{e} = 28\ 000 \quad \text{(A-38)} \qquad Re_{tr} = 5(10)^5 \tag{A-39}$$

The Reynolds number correction factor is then calculated using equation (A-40) (Aungier, 2006):

$$K_{RE} = \begin{cases} \sqrt{Re_{lam}/Re_c}, & Re_c < Re_{lam} \\ 1, & Re_{lam} < Re_c < Re_{tr} \\ 1 + \left[\dfrac{\log(Re_{tr})}{\log(Re_r)}\right]^{2,58}\left(1 - \dfrac{Re_{tr}}{Re_c}\right), & Re_r < Re_{tr} < Re_c \\ \left[\dfrac{\log(Re_{tr})}{\log(Re_r)}\right]^{2,58}, & Re_{tr} < Re_r < Re_c \\ \left[\dfrac{\log(Re_{tr})}{\log(Re_c)}\right]^{2,58}, & Re_{tr} < Re_c < Re_r \\ = 1,083 \end{cases} \tag{A-40}$$

Trailing edge loss correction factor calculation

The trailing edge loss correction factor is calculated using equation **Error! Reference source not found.**) (Aungier, 2006):

$$\Delta Y_{TE} = \left(\frac{0,02s}{s\sin\beta_g - 0,02s}\right)^2 = 0,00194 \tag{A-41}$$

A.1.3. Secondary flow loss coefficient calculation

The secondary flow loss coefficient is calculated using equations (3.20) to (3.26) (Aungier, 2006):

$$\alpha'_m = 90° - \operatorname{atan}\left(\frac{\cot\alpha'_{b0} + \cot\alpha'_{b1}}{2}\right)\frac{180°}{\pi} = 51,5° \tag{A-42}$$

$$C_L = 2|\cot\alpha'_{b1} - \cot\alpha'_{b0}|\sin\alpha'_m\,(s/c) = 2,06 \tag{A-43}$$

$$Z = \left(\frac{C_L}{(s/c)}\right)^2 \frac{\sin^2 \alpha'_{b1}}{\sin^3 \alpha'_m} = 3{,}67 \tag{A-44}$$

$$F_{AR} = \begin{cases} 0{,}5\left(\dfrac{2c}{H}\right)^{0.7}, & H/c < 2 \\ c/H, & H/c \geq 2 \end{cases} = 1{,}02 \tag{A-45}$$

$$\tilde{Y}_s = 0{,}0334 F_{AR} Z \frac{\sin \alpha'_{b1}}{\sin \beta_{b0}} = 0{,}672 \tag{A-46}$$

$$K_s = 1 - (1 - K_p)\left[\frac{(b_z/H)^2}{1 + (b_z/H)^2}\right] = 0{,}957 \tag{A-47}$$

$$Y_s = K_{RE} K_s \sqrt{\frac{\tilde{Y}_s^2}{1 + 7{,}5\tilde{Y}_s^2}} = 0{,}0685 \tag{A-48}$$

A.1.4. Blade clearance loss coefficient calculation

The blade clearance loss coefficient is calculated using equation (3.27) (Aungier, 2006):

$$Y_{CL} = 0{,}47 Z (c/H)(\delta/c)^{0,78} = 0 \tag{A-49}$$

A.1.5. Shock loss coefficient calculation

The shock loss coefficient is calculated using equations (3.28) to (3.31) (Aungier, 2006):

$$X_1 = \begin{cases} 0, & M'_0 \leq 0{,}4 \\ M'_0 - 0{,}4, & M'_0 > 0{,}4 \end{cases} = 0 \tag{A-50}$$

$$X_2 = \begin{cases} 0, & M'_0 <= M'_1 \\ \dfrac{M'_0}{M'_1} - 1, & M'_0 > M'_1 \end{cases} = 0 \tag{A-51}$$

$$\tilde{Y}_{SH} = 0{,}8 X_1^2 + X_2^2 = 0 \tag{A-52}$$

$$Y_{SH} = \sqrt{\frac{\tilde{Y}_{SH}^2}{1 + \tilde{Y}_{SH}^2}} = 0 \tag{A-53}$$

A.2. Exit static pressure based state solution sample calculations

Interpolations of an ideal gas property table (Cengel & Boles, 2004) are used for relating the intrinsic thermodynamic properties of air. These linear interpolations are shown implicitly as one property being a function of another.

A.2.1. Stator inlet state solution: sample calculation

The values of the known flow field, gas property and geometric parameters at the stator inlet are shown in Table A-2.

Table A-2: Known parameter values at the stator inlet

Parameter	Known value
Cross-sectional flow area, A_0	0,001752 m^2
Absolute flow angle, α_0	0°
Total temperature, T_{t0}	1119 K
Total pressure, p_{t0}	308,3 kPa
Total temperature dependent specific entropy, s_{t0}^o	3,097 kJ/kg/K
Static pressure, p_0	297,3 kPa

The calculations for obtaining the mass flow rate at the stator inlet are shown in equations (A-54) to (A-60):

$$s_0^o = s_{0t}^o + R_{air} \ln(p_0/p_{t0}) = 3,087 \text{ kJ/kg/K} \tag{A-54}$$

$$h_0 = h(s_0^0) = 1172 \text{ kJ/kg} \tag{A-55}$$

$$T_0 = T(s_0^o) = 1109 \text{ K} \tag{A-56}$$

$$\rho_0 = p_0/(R_{air} T_0) = 0,934 \text{ kg/m}^3 \tag{A-57}$$

$$h_{t0} = h(T_{t0}) = 1183 \text{ kJ/kg} \tag{A-58}$$

$$C_0 = \sqrt{2(h_{t0} - h_0)} = 152,3 \text{ m/s} \tag{A-59}$$

$$\dot{m}_0 = A_0 \rho_0 C_0 \cos \alpha_0 = 0,249 \text{ kg/s} \tag{A-60}$$

A.2.2. Stator exit state solution: sample calculation

The values of the known flow field, gas property and geometric parameters at the stator exit are shown in Table A-3.

Table A-3: Known parameter values at the stator exit

Parameter	Known value
Cross-sectional flow area, A_1	0,001752 m^2
Blade angle, β_1	57,86°

Total enthalpy, h_{t1}	1183 kJ/kg
Static pressure, p_1	256,8 kPa

The calculations for obtaining the mass flow rate at the stator exit are shown in equations (A-61) to (A-69). Since only the last iteration is shown, the stator blade row total pressure loss coefficient has already converged to the value shown in (A-61):

$$Y_S = 0,125 \tag{A-61}$$

$$s_{t1}^o = s^o(h_{t1}) = 3,097 \text{ kJ/kg/K} \tag{A-62}$$

$$s_1^o = s_{t1}^o - R_{air} \ln\left(\frac{p_{t0} + p_1 Y_S}{p_1 + p_1 Y_S}\right) = 3,05 \text{ kJ/kg/K} \tag{A-63}$$

$$T_1 = T(s_1^o) = 1075 \text{ K} \tag{A-64}$$

$$\rho_1 = p_1/(R_{air} T_1) = 0,833 \text{ kg/m}^3 \tag{A-65}$$

$$h_1 = h(T_1) = 1132 \text{ kJ/kg} \tag{A-66}$$

$$C_1 = \sqrt{2(h_{t1} - h_1)} = 321,1 \text{ m/s} \tag{A-67}$$

$$\alpha_1 = \beta_1 = 57,86° \tag{A-68}$$

$$\dot{m}_1 = \rho_1 A_1 C_1 \cos(\alpha_1) = 0,249 \text{ kg/s} \tag{A-69}$$

A.2.3. Rotor inlet state solution: sample calculation

The values of the known flow field, gas property and geometric parameters at the rotor inlet are shown in Table A-4. Furthermore, at the stator exit, the mean radius is taken to be 27.65 mm and the values for the absolute gas velocity are as in the previous section.

Table A-4: Known parameter values at the rotor inlet

Parameter	Known value
Cross-sectional flow area, A_2	0,001897 m²
Total enthalpy, h_{t2}	1183 kJ/kg
Total pressure, p_{t2}	302,6 kPa
Mean radius, r_{m2}	27,62 mm
Static density guess, ρ_2	0,838 kg/m³

The axial component of the absolute gas velocity at the rotor inlet is calculated in equation (A-70) and the circumferential component is calculated using equation (3.37). The magnitude of the absolute gas velocity is then calculated using equation (A-72).

$$C_{z2} = \frac{\dot{m}_1}{\rho_2 A_2} = 156,9 \text{ m/s} \tag{A-70}$$

$$C_{\theta 2} = C_1 (\sin \alpha_1) \left(\frac{r_{m1}}{r_{m2}} \right) = 272,2 \text{ m/s} \tag{A-71}$$

$$C_2 = \sqrt{C_{z2}^2 + C_{\theta 2}^2} = 313,6 \text{ m/s} \tag{A-72}$$

The relative circumferential gas velocity component is calculated using (3.38) and the magnitude is calculated using equation (3.39).

$$W_{\theta 2} = C_{\theta 2} - U_2 = C_{\theta 2} - r_{m2}\omega = -74,89 \text{ m/s} \tag{A-73}$$

$$W_2 = \sqrt{C_{z2}^2 + W_{\theta 2}^2} = 174,0 \text{ m/s} \tag{A-74}$$

The calculations for obtaining the static properties at the rotor inlet are shown in equations (A-75) to (A-79).

$$h_2 = h_{t2} - \frac{1}{2}C_2^2 = 1134 \text{ kJ/kg} \tag{A-75}$$

$$T_2 = T(h_2) = 1077 \text{ K} \tag{A-76}$$

$$s_2^o = s^o(T_2) = 3,053 \text{ kJ/kg/K} \tag{A-77}$$

$$p_2 = p_{t2} \exp\left(\frac{s_2^o - s_{t2}^o}{R_{air}} \right) = 258,8 \text{ kPa} \tag{A-78}$$

$$\rho_2 = \frac{p_2}{R_{air}T_2} = 0,838 \text{ kg/m}^3 \tag{A-79}$$

The calculations for obtaining the relative total gas properties at the rotor inlet are shown in equations (A-80) to (A-82).

$$h_{t2}' = h_2 + \frac{1}{2}W_2^2 = 1149 \text{ kJ/kg} \tag{A-80}$$

$$s_{t2}^{o'} = s^o(h_{t2}') = 3,066 \text{ kJ/kg/K} \tag{A-81}$$

$$p_{t2}' = p_2 \exp\left(\frac{s_{t2}^{o'} - s_2^o}{R_{air}} \right) = 271,7 \text{ kPa} \tag{A-82}$$

A.2.4. Rotor exit state solution: sample calculation

The values of the known flow field, gas property and geometric parameters at the rotor exit are shown in Table A-5.

Table A-5: Known parameter values at the rotor exit

Parameter	Known value
Cross-sectional flow area, A_3	0,001897 m^2
Blade angle, β_3	-62,35°
Mean radius, r_{m3}	27,62 mm
Relative total enthalpy, h'_{t3}	1149 kJ/kg
Static pressure, p_3	153,0 kPa

The calculations for obtaining the mass flow rate at the rotor exit are shown in equations (A-83) to (A-91). Since only the last iteration is shown, the rotor blade row relative total pressure loss coefficient has already converged to the value shown in (A-83):

$$Y_R = 0,360 \tag{A-83}$$

$$s^{o'}_{t3} = s^o(h'_{t3}) = 3,066 \text{ kJ/kg/K} \tag{A-84}$$

$$s^o_3 = s^{o'}_{t3} - R_{air} \ln\left(\frac{p'_{t2} + p_3 Y_R}{p_3 + p_3 Y_R}\right) = 2,937 \text{ kJ/kg/K} \tag{A-85}$$

$$T_3 = T(s^o_3) = 973,3 \text{ K} \tag{A-86}$$

$$\rho_3 = p_3/(R_{air} T_3) = 0,548 \text{ kg/m}^3 \tag{A-87}$$

$$h_3 = h(T_3) = 1016 \text{ kJ/kg} \tag{A-88}$$

$$W_3 = \sqrt{2(h'_{t3} - h_3)} = 516,9 \text{ m/s} \tag{A-89}$$

$$\alpha'_3 = \beta_3 = -62,35° \tag{A-90}$$

$$\dot{m}_3 = \rho_3 A_3 W_3 \cos(\alpha'_3) = 0,2492 \text{ kg/s} \tag{A-91}$$

A.2.5. Turbine stage performance parameters: sample calculation

The turbine stage has three performance parameters: mass through flow rate, total-to-total pressure ratio and total-to-total isentropic efficiency. The stage mass through flow rate is taken as the mass flow rate calculated during the gas states calculation process. In this case it is taken to be 0.2492 kg/s. To calculate the

total-to-total pressure ratio, the rotor exit total pressure is needed. The calculations for obtaining the total-to-total pressure ratio are shown in equations (A-92) to (A-98).

$$C_{\theta 3} = W_3 \sin \alpha'_3 + r_{m3}\omega = -110,8 \text{ m/s} \tag{A-92}$$

$$C_{z3} = W_3 \cos \alpha'_3 = 239,9 \text{ m/s} \tag{A-93}$$

$$C_3 = \sqrt{C_{\theta 3}^2 + C_{z3}^2} = 264,2 \text{ m/s} \tag{A-94}$$

$$h_{t3} = h_3 + \frac{1}{2}C_3^2 = 1051 \text{ kJ/kg} \tag{A-95}$$

$$s_{t3}^o = s^o(h_{t3}) = 2,972 \text{ J/kg/K} \tag{A-96}$$

$$p_{t3} = p_3 \exp\left(\frac{s_{t3}^o - s_3^o}{R_{air}}\right) = 173,0 \text{ kPa} \tag{A-97}$$

$$PR_{tt} = \frac{p_{t0}}{p_{t3}} = 1,782 \tag{A-98}$$

The ideal total stage exit enthalpy is required to calculate the total-to-total isentropic efficiency of the turbine stage. It is calculated using isentropic relations in equations (A-99) and (A-100).

$$s_{t3,ideal}^o = s_{t0}^o + R_{air} \ln\left(\frac{p_{t3}}{p_{t0}}\right) = 2,932 \text{ kJ/kg/K} \tag{A-99}$$

$$h_{t3,ideal} = h\left(s_{t3,ideal}^o\right) = 1011 \text{ kJ/kg} \tag{A-100}$$

Using equation (3.40), the total-to-total isentropic efficiency of the turbine stage is calculated:

$$\eta_{tt} = \frac{h_{t0} - h_{t3}}{h_{t0} - h_{t3,ideal}} = 0,7680 = 76,8 \text{ \%}. \tag{A-101}$$

Appendix B: Turbine design process calculations

This appendix contains sample calculations for different stages of the design procedure. As in Appendix A, the intrinsic ideal gas properties of air are related by property table interpolations.

B.1. Turbine inlet total temperature sample calculation

The turbine inlet total temperature and pressure are calculated from the experimental test results shown in Table 4-2. Using ideal gas isentropic relations, the compressor work is calculated from the compressor inlet total temperature, the total-to-total pressure ratio and the total-to-total efficiency. This procedure is shown in equations (B-1) to (B-5).

$$h_{C,t,in} = h(T_{C,t,in}) = 289,4 \text{ kJ/kg} \tag{B-1}$$

$$s^o_{C,t,in} = s^o(T_{C,t,in}) = 1,665 \text{ kJ/kg/K} \tag{B-2}$$

$$s^o_{C,t,id,out} = s^o_{C,t,in} + R_{air} \ln\left(\frac{p_{C,t,out}}{p_{C,t,in}}\right) = 1,986 \text{ kJ/kg/K} \tag{B-3}$$

$$h_{C,t,id,out} = h(s^o_{C,t,id,out}) = 398,4 \text{ kJ/kg} \tag{B-4}$$

$$w_C = \frac{(h_{C,t,id,out} - h_{C,t,in})}{\eta_{C,tt}} = 129,2 \text{ kJ/kg} \tag{B-5}$$

The turbine work is obtained by assuming zero mechanical losses between the compressor and the turbine. This assumption results in equal power output and consumption by the turbine and the compressor respectively. The turbine work is then found by dividing the power output by the turbine mass flow rate. These calculations are shown in equations (B-6) to (B-9).

$$P_C = \dot{m}_{air} w_C = 37,3 \text{ kW} \tag{B-6}$$

$$P_T = P_C = 37,3 \text{ kW} \tag{B-7}$$

$$\dot{m}_T = \dot{m}_{air} + \dot{m}_{fuel} = 0,2942 \text{ kg/s} \tag{B-8}$$

$$w_T = \frac{P_T}{\dot{m}_T} = 126,8 \text{ kJ/kg} \tag{B-9}$$

Ideal gas relations and energy conservation are employed in calculating the turbine inlet total temperature from the measured turbine exit temperature and the calculated turbine work. Equations (B-10) to (B-12) show the calculation of the turbine inlet total temperature.

$$h_{T,t,out} = h(T_{T,t,out}) = 1056 \text{ kJ/kg} \tag{B-10}$$

$$h_{T,t,in} = h_{T,t,out} + w_T = 1183 \text{ kJ/kg} \tag{B-11}$$

$$T_{T,t,in} = T(h_{T,t,in}) = 1119 \text{ K} \tag{B-12}$$

The total pressure is assumed to remain constant throughout the combustion chamber. Therefore, the turbine inlet total pressure is taken to be equal to the compressor exit total pressure. This relation is shown in equation (B-13).

$$p_{T,t,in} = p_{C,t,out} = 310 \text{ kPa} \tag{B-13}$$

B.2. Non-dimensional performance parameters sample calculation

The non-dimensional performance parameters are dependent on the axial gas velocity through the turbine stage, the rotor blade speed, the exit flow angle and the power absorbed. The latter three parameters are known from previous calculations, which leaves the axial gas velocity to be calculated. The axial gas velocity is dependent on the mass flow rate, the static gas density and the flow area at a given cross section. The flow area is calculated from the stage inlet geometry specified in Table 4.1:

$$A_0 = \pi(r_{s0}^2 - r_{h0}^2) = 3{,}46(10)^{-4} \text{ m}^2 \tag{B-14}$$

Since the turbine inlet total gas properties are specified in Table 4.3, the static flow properties can be calculated using the mass flow rate obtained in equation (B-8). In equations (B-15) and (B-16), the static density of the gas at the turbine inlet is approximated by assuming it to equal the total gas density. This density is then used in equation (B-17) with the known inlet flow area and mass flow rate to obtain an inlet axial velocity estimate. Since a purely axial inlet velocity has been chosen, the velocity magnitude equals the axial velocity. Therefore, the velocity estimate, together with the known total thermodynamic properties, can be used to find the static density, as shown in equations (B-18) to (B-22).

$$\rho_{0,estimate} = p_{t0}/(R_{air}T_{t0}) = 0{,}965 \text{ kg/m}^3 \tag{B-15}$$

$$\rho_0 = \rho_{0,estimate} \tag{B-16}$$

$$C_0 = \dot{m}_{turbine}/(\rho_0 A_0) = 217 \text{ m/s} \tag{B-17}$$

$$h_0 = h_{t0} - C_0^2/2 = 1160 \text{ kJ/kg} \tag{B-18}$$

$$T_0 = T(h_0) = 1100 \text{ K} \tag{B-19}$$

$$s_0^o = s^o(T_0) = 3{,}08 \text{ kJ/kg/K} \tag{B-20}$$

$$p_0 = p_{t0}\exp[(s_0^o - s_{t0}^o)/R_{air}] = 288 \text{ kPa} \tag{B-21}$$

$$\rho_0 = p_0/(R_{air}T_0) = 0{,}913 \text{ kg/m}^3 \tag{B-22}$$

The density obtained in equation (B-22) can then be used as a new static density estimate in equation (B-17). The calculation of equations (B-17) to (B-22) is

repeated until the calculated value of the static inlet density has converged. For the values in this sample calculation, the converged static density and axial velocity are $0,906 \text{ kg/m}^3$ and 232 m/s respectively. The non-dimensional flow coefficient, work coefficient and reaction ratio are then calculated in equations (B-23) to (B-25).

$$\phi_{mean} = C_m/U = C_m/(r_{mean}\omega_{turbine}) = 0,670 \tag{B-23}$$

$$\psi_{mean} = \Delta h_0/U^2 = (P_{turbine}/\dot{m}_{turbine})/(r_{mean}\omega_{turbine})^2 \\ = 1,07 \tag{B-24}$$

$$R_{mean} = 1 - \phi_{mean}\tan\alpha_{3,mean} - \psi_{mean}/2 = 0,466 \tag{B-25}$$

B.3.　Mean radius gas velocity triangle calculations

For a constant radius stream sheet, the blade speed remains constant across a blade row. Therefore, since the mean radius remains constant throughout the turbine stage,

$$W_{\theta2,mean} - W_{\theta3,mean} = C_{\theta2,mean} - C_{\theta3,mean}. \tag{B-26}$$

The stage flow and work coefficients are defined as:

$$\phi_{mean} = \frac{C_{z,mean}}{U_{mean}} \tag{B-27}$$

and

$$\psi_{mean} = \frac{\Delta h_t}{U_{mean}^2}. \tag{B-28}$$

Applying Euler's turbine equation and equation (B-26), the stage work coefficient can be written as either

$$\psi_{mean} = \frac{C_{\theta2,mean} - C_{\theta3,mean}}{U_{mean}}, \tag{B-29}$$

or

$$\psi_{mean} = \frac{W_{\theta2,mean} - W_{\theta3,mean}}{U_{mean}}. \tag{B-30}$$

The stage reaction ratio is defined as the ratio of the static enthalpy drop across the rotor blade row to the total enthalpy drop across the whole stage.

$$R_{mean} = \frac{h_2 - h_3}{\Delta h_t}. \tag{B-31}$$

Using the definition of total enthalpy and considering that all of the stage work is done on the rotor blade row; this expression can be rewritten as

$$R_{mean} = \frac{h_{t2} - h_{t3} - \frac{1}{2}\left(C_{2,mean}^2 - C_{3,mean}^2\right)}{\Delta h_t}$$

$$= \frac{\Delta h_t - \frac{1}{2}\left(C_{2,mean}^2 - C_{3,mean}^2\right)}{\Delta h_t}.$$

(B-32)

By applying Euler's turbine equation and breaking the gas velocities up in orthogonal components, the turbine stage reaction ratio can be written as:

$$R_{mean} = 1 + \frac{C_{\theta2,mean} - C_{\theta3,mean}}{2U_{mean}} - \frac{C_{\theta2,mean}}{U_{mean}}$$

$$= 1 + \frac{1}{2}\frac{C_{\theta2,mean} - C_{\theta3,mean}}{U_{mean}} - \frac{C_{z,mean}\tan\alpha_{2,mean}}{U_{mean}}.$$

(B-33)

Substituting equations (B-27) and (B-29) into equation (B-33) allows the stage exit angle to be expressed as:

$$\alpha_{2,mean} = \tan^{-1}\left(\frac{1 - R_{mean} + \frac{\psi_{mean}}{2}}{\phi_{mean}}\right).$$

(B-34)

It can similarly be shown by substituting equations (B-26) and (B-30) into equation (B-33) that the rotor relative inlet and exit flow angles are given by equations (4.6) and (4.7).

Table B-1: Calculated turbine stage gas velocities

Location, i	Absolute flow angle, α_i	Absolute gas velocity magnitude, C_i	Relative flow angle, α_i'	Relative gas velocity magnitude, W_i
0	0 °	237 m/s	0 °	237 m/s
1	57,1 °	437 m/s	57,1 °	437 m/s
2	57,1 °	437 m/s	5,15 °	238 m/s
3	0 °	237 m/s	-55.6 °	419 m/s

B.4. Turbine gas states sample calculation

This is a sample calculation of the gas states throughout the turbine stage. The gas states are calculated from the stage inlet total gas properties in Table 4-3, the mean radius gas velocities in Table B-1, and stator and rotor blade row total

pressure loss coefficients of 0,085 and 0,166 respectively. Since the both the relative and the absolute gas velocities are known throughout the turbine stage, the definitions of total enthalpy and relative total enthalpy are used throughout the calculations to interrelate the static, total and relative total enthalpies.

B.4.1. State 0 calculation

The turbine stage inlet static gas conditions are calculated from the turbine inlet total temperature and pressure, and the turbine inlet velocity. The definition of total enthalpy is used to relate the total state to the static state in equation (B-37). Variable specific heat isentropic ideal gas relations are then used to relate the static pressure to the total pressure in equation (B-40). With the static state known, the sonic velocity and gas density at the stator inlet are calculated in equations (B-41) and (B-42) respectively.

$$h_{t0} = h(T_{to}) = 1183 \text{ kJ/kg} \tag{B-35}$$

$$s_{t0}^o = s^o(T_{to}) = 3,097 \text{ kJ/kg/K} \tag{B-36}$$

$$h_0 = h_{t0} - \frac{1}{2}C_0^2 = 1155 \text{ kJ/kg} \tag{B-37}$$

$$T_0 = T(h_0) = 1095 \text{ K} \tag{B-38}$$

$$s_0^o = s^o(T_0) = 3,072 \text{ kJ/kg/K} \tag{B-39}$$

$$p_0 = p_{t0} \exp\left(\frac{s_0^o - s_{t0}^o}{R_{air}}\right) = 284 \text{ kPa} \tag{B-40}$$

$$a_0 = \sqrt{\gamma(T_0)\, R_{air}\, T_0} = 657 \text{ m/s} \tag{B-41}$$

$$\rho_0 = \frac{p_0}{R_{air}\, T_0} = 0,903 \text{ kg/m}^3 \tag{B-42}$$

B.4.2. State 1 calculation

Assuming conservation of total enthalpy, the total enthalpy is known at the stator exit. The definition of total enthalpy is used to obtain the static enthalpy in equation (B-44). The stator total pressure loss coefficient is then used in equation (B-47) to calculate the static pressure. The sonic velocity and density are then calculated as before in equations (B-49) and (B-50) respectively.

$$h_{t1} = h_{t0}, \qquad T_{t1} = T_{t0}, \qquad s_{t1}^o = s_{t0}^o \tag{B-43}$$

$$h_1 = h_{t1} - \frac{1}{2}C_1^2 = 1088 \text{ kJ/kg} \tag{B-44}$$

$$T_1 = T(h_1) = 1036 \text{ K} \tag{B-45}$$

$$s_1^o = s^o(T_1) = 3{,}009 \text{ kJ/kg/K} \tag{B-46}$$

$$p_1 = \frac{p_{t0}}{(1 + Y_S) \exp\left(\dfrac{s_{t1}^o - s_1^o}{R_{air}}\right) - Y_S} = 222{,}6 \text{ kPa} \tag{B-47}$$

$$p_{t1} = p_1 \exp\left(\frac{s_{t1}^o - s_1^o}{R_{air}}\right) = 303{,}1 \text{ kPa} \tag{B-48}$$

$$a_1 = \sqrt{\gamma(T_1)\, R_{air}\, T_1} = 639{,}8 \text{ m/s} \tag{B-49}$$

$$\rho_1 = \frac{p_1}{R_{air}\, T_1} = 0{,}748 \text{ kg/m}^3 \tag{B-50}$$

B.4.3. State 2 calculation

The total and static thermodynamic properties are assumed to remain constant from the stator exit to the rotor inlet. However, the relative total properties do change due to the motion of the rotor. The definition of the relative total enthalpy and variable specific heat isentropic ideal gas relations are used to determine the relative total state in equations (B-53) and (B-56).

$$h_{t2} = h_{t1}, \qquad T_{t2} = T_{t1}, \qquad s_{t2}^o = s_{t1}^o, \qquad p_{t2} = p_{t1} \tag{B-51}$$

$$h_2 = h_1, \qquad T_2 = T_1, \qquad s_2^o = s_1^o, \qquad p_2 = p_1 \tag{B-52}$$

$$h_{t2}' = h_2 + \frac{1}{2}W_2^2 = 1116 \text{ kJ/kg} \tag{B-53}$$

$$T_{t2}' = T(h_{t2}') = 1061 \text{ K} \tag{B-54}$$

$$s_{t2}^{o\prime} = s^o(T_{t2}') = 3{,}036 \text{ kJ/kg/K} \tag{B-55}$$

$$p_{t2}' = p_2 \exp\left(\frac{s_{t2}^{o\prime} - s_2^o}{R_{air}}\right) = 244{,}5 \text{ kPa} \tag{B-56}$$

B.4.4. State 3 calculation

Assuming constant radius flow, the relative total enthalpy stays conserved across the rotor blades. Therefore, the static enthalpy at the rotor exit is found from the definition of relative total enthalpy in equation (B-58). Similarly to the stator exit

static pressure, in equation (B-61) the rotor exit static pressure is obtained using the rotor relative total pressure loss coefficient and the variable specific heat isentropic ideal gas relations. The latter is utilised again in equation (B-66) to obtain the total pressure at the rotor exit. The sonic velocity and gas density are found as before in equations (B-67) and (B-68).

$$h'_{t3} = h'_{t2}, \qquad T'_{t3} = T'_{t2}, \qquad s^{o'}_{t3} = s^{o'}_{t2} \tag{B-57}$$

$$h_3 = h'_{t3} - \frac{1}{2}W_3^2 = 1028 \text{ kJ/kg} \tag{B-58}$$

$$T_3 = T(h_3) = 984,3 \text{ K} \tag{B-59}$$

$$s^o_3 = s^o(T_3) = 2,950 \text{ kJ/kg/K} \tag{B-60}$$

$$p_3 = \frac{p'_{t2}}{(1 + Y_R)\exp\left(\dfrac{s^{o'}_{t3} - s^o_3}{R_{air}}\right) - Y_R} = 173,8 \text{ kPa} \tag{B-61}$$

$$p'_{t3} = p_3 \exp\left(\frac{s^{o'}_{t3} - s^o_3}{R_{air}}\right) = 234,5 \text{ kPa} \tag{B-62}$$

$$h_{t3} = h_3 + \frac{1}{2}C_3^2 = 1056 \text{ kJ/kg} \tag{B-63}$$

$$T_{t3} = T(h_{t3}) = 1009 \text{ K} \tag{B-64}$$

$$s^o_{t3} = s^o(T_{t3}) = 2,978 \text{ kJ/kg/K} \tag{B-65}$$

$$p_{t3} = p_3 \exp\left(\frac{s^o_{t3} - s^o_3}{R_{air}}\right) = 191,8 \text{ kPa} \tag{B-66}$$

$$a_3 = \sqrt{\gamma(T_3)\, R_{air}\, T_3} = 624,1 \text{ m/s} \tag{B-67}$$

$$\rho_3 = \frac{p_3}{R_{air}\, T_3} = 0,615 \text{ kg/m}^3 \tag{B-68}$$

Since both the gas velocities and thermodynamic states throughout the turbine are known, equation (B-69) is used to calculate the absolute and relative Mach numbers throughout the turbine. These calculated values are shown in Table B-2.

$$M'_i = \frac{W_i}{a_i} \tag{B-69}$$

Table B-2: Calculated turbine stage gas Mach numbers

Location, i	Absolute Mach number, M_i	Relative Mach number, M_i'
0	0,36	0,36
1	0,68	0,68
2	0,68	0,37
3	0,38	0,67

B.5.   Blade row geometric parameters – sample calculations

This is a sample calculation of the blade parameters of a rotor blade row during the design process. The calculation uses the flow angles and Mach numbers given in Tables B-1 and B-2 respectively and uses the gas states calculated in section B.4. The calculation also uses the geometrical design parameters given in Table 4-1. The optimal pitch-to-chord ratio is first calculated, and then the other blade row geometric parameters are determined.

B.5.1. Calculating the optimal pitch-to-chord ratio

Firstly, the relative flow angles before and after the rotor blade row obtained in section B.3 are transformed into the generic blade angle convention using equations (1.3) and (1.4).

$$\alpha_{b2}' = 90° - \alpha_2' = 84{,}85° \tag{B-70}$$

$$\alpha_{b3}' = 90° + \alpha_3' = 34{,}4° \tag{B-71}$$

The optimal pitch-to-chord ratio is now determined by first calculating the optimal pitch-to-chord ratios for nozzle and impulse blades with the the given relative exit flow angle in equations (B-73) and (B-74) respectively. The gas deflection ratio, obtained in equation (B-72), is then used to interpolate between these two values in equation (B-75), thus yielding the optimal pitch-to-chord ratio. (Aungier, 2006)

$$\xi = \frac{90° - \alpha_{b2}'}{90° - \alpha_{b3}'} = 0{,}0926 \tag{B-72}$$

$$(s/c)_{nozzle} = 0.427 + \frac{\alpha_{b3}'}{58°} - \left(\frac{\alpha_{b3}'}{93°}\right)^2 = 0{,}883 \tag{B-73}$$

$$(s/c)_{impulse} = 0.224 + \left(1.575 - \frac{\alpha'_{b3}}{90°}\right)\left(\frac{\alpha'_{b3}}{90°}\right) = 0{,}680 \tag{B-74}$$

$$(s/c)_{opt} = (s/c)_{nozzle} + \left[(s/c)_{nozzle} - (s/c)_{impulse}\right]|\xi|\xi = 0{,}882 \tag{B-75}$$

B.5.2. Determining the blade pitch, chord and stagger angle

The blade pitch, chord and stagger angle are calculated iteratively. However, the pitch-to-chord ratio depends on the stream sheet area ratio correction factor, calculated in equation (B-75), which is unaffected by the other variables.

$$F_{AR} = 0{,}8 + 0{,}2\left(\frac{\rho_2\,C_{z2}}{\rho_3\,C_{z3}}\right) = 0{,}8 + 0{,}2\left(\frac{\rho_2}{\rho_3}\right) = 1{,}04 \tag{B-75}$$

As a starting point for the iterative procedure for satisfying equations (4.21), (4.25), (4.24) and (4.23), a zero deviation angle is assumed. However, the calculated deviation angle converges to a value of $\delta = 1{,}92°$. Therefore, for the final iteration shown in equations (B-76) to (B-79), the converged value is used.

$$(o/s) = F_{AR}\sin(\alpha'_{b3} - \delta) = 0{,}56 \tag{B-76}$$

$$\beta_g = \sin^{-1}(o/s) = 34{,}1° \tag{B-77}$$

$$\delta_0 = \sin^{-1}\left\{(o/s)[1 + (1 - o/s)]\left(\frac{\beta_G}{90°}\right)\right\} - \beta_G = 2{,}48° \tag{B-78}$$

$$\delta = \begin{cases} \delta_0, & M'_3 \leq 0{,}5 \\ \delta_0(1 - 10(2M'_3 - 1)^3 + 15(2M'_3 - 1)^4 - 6(2M'_3 - 1)^5), & M'_3 > 0{,}5 \\ = 1.92° \end{cases} \tag{B-79}$$

The stagger angle is now calculated using equation (4.26). The blade chord is then calculated in equation (B-81), enabling the calculation of the blade pitch in equation (B-82) and subsequently the number of blades in equation (B-83).

$$\gamma = \frac{(180° - \beta_2 + 1.5\beta_g)}{2.5} = 58{,}5° \tag{B-80}$$

$$c = \frac{b_{zr}}{sin(\gamma)} = 8{,}21\ mm \tag{B-81}$$

$$s = c\,(s/c)_{opt} = 7{,}24\ \text{mm} \tag{B-82}$$

$$N = \frac{2\pi r_m}{s} = 23{,}9 \tag{B-83}$$

Since a prime number of blades is preferable, the blade number is rounded down to 23.

Appendix C: CFD verification

C.1. Inlet and outlet block length independence

This section illustrates the inlet and outlet domain length independence of the flow solutions obtained during the CFD performance analysis. The inlet and outlet sections act as buffer zones between the turbine blade rows and the domain inlet and outlet surfaces. The inlet and outlet section lengths must therefore be long enough to prevent the constant property and zero gradient boundary conditions from influencing the flow field near the blades.

To determine whether the inlet and outlet section lengths are long enough, three different lengths for the inlet and outlet sections are simulated. The three simulations have constant values for the other flow simulation parameters, and computational meshes of similar elements counts. The results of the three simulations are shown in Table. The simulated mass flow rate through the turbine and the total-to-total stage efficiency are shown for different inlet and outlet domain lengths.

Table C-1: Domain length independence study results

Inlet and outlet domain lengths	Simulated turbine mass flow rate, kg/s	Simulated turbine total-to-total efficiency
5 mm	0,287	91,7 %
10 mm	0,287	91,8 %
20 mm	0,287	91,7 %

It can be seen in Table that doubling the inlet and outlet domain lengths first from 5 mm to 10 mm and then again to 20 mm has very little effect on the measured parameters. It is therefore concluded that inlet and outlet lengths of 10 mm can be used with minimal influence on the flow field around the turbine blades.

C.2. Computational mesh independence

This section illustrates the mesh density independence of the flow solutions obtained during the CFD performance analysis. This is done by simulating the same flow problem using three computational meshes with different element counts. Simulation B of the 95 % work coefficient design is solved using three computational meshes consisting of roughly 100,000, 200,000 and 400,000 elements respectively. The results of the three simulations are shown in Table.

The simulated mass flow rate through the turbine and the total-to-total stage efficiency are shown for each mesh element count.

Table C-2: Mesh independence study results

Number of mesh elements	Simulated turbine mass flow rate, kg/s	Simulated turbine total-to-total efficiency
119 595	0,287	92,1 %
212 630	0,288	91,8 %
424 844	0,285	92,3 %

It is clear from Table that varying the mesh density in between element counts of approximately 100,000, 200,000 and 400,000 has little effect on the predicted mass flow rate or total-to-total efficiency. Therefore, it is concluded that a computational mesh element count of approximately 200,000 can be used with confidence to generate mesh independent results.

Appendix D: FEM analysis information

D.1. Material properties of Inconel IN713 LC

Table D-1: Mechanical properties of Inconel IN713 LC (Nickel Development Institute, 1995)

Density, kg/m^3			8000
Poisson's ratio (Creci, et al., 2010)			0,382
Temperature, K	**Thermal expansion coefficient, µm/m°C**	**Modulus of elasticity, GPa**	**Yield strength, MPa**
294	-	197	750
366	10,1	194	-
477	12,6	186	-
589	13,7	183	-
700	14,9	178	-
811	15,8	172	760
922	16	165	785
1033	10,1	159	760
1144	16,2	149	580
1255	16,7	136	285
1366	17	-	-
1033	18,9	-	-

D.2. FEM mesh convergence studies

D.2.1. Mesh independence of static structural analyses

To investigate the dependence of the static structural analysis results on the computational mesh element size, a mesh independence study is performed. Static structural analyses of the 95 % work coefficient turbine design are performed using computational meshes with different element counts. The mesh element count and the resulting tip displacement and maximum Von-Mises stress of each simulation are shown in Table.

Table D-2: Static structural mesh independence study results

Number of mesh elements	Total tip displacement, mm	Max. von-mises root stress, MPa
14,994	0,330	738
22,923	0,330	743
45,182	0,330	710
93,117	0,330	707
168,354	0,330	709

The blade tip displacement does not change between the different simulations, but the maximum Von-Mises stress does change markedly for the first three simulations. Thereafter the maximum Von-Mises stress remains fairly constant. Therefore, it is concluded that a mesh element count of approximately 45,000 is sufficient to obtain mesh independent static structural analysis results.

D.2.2. Mesh independence of structural modal analyses

A mesh independence study is also performed to investigate the dependence of the modal structural analysis results on the computational mesh element size. Modal structural analyses of the 95 % work coefficient turbine design are performed using computational meshes with different element counts. The mesh element count and the resulting first three blade natural frequencies of each simulation are shown in Table.

Table D-3: Modal analysis mesh independence study results

Number of mesh elements	1st natural frequency	2nd natural frequency	3rd natural frequency
14,999	6,57 kHz	15,2 kHz	23,3 kHz
23,182	6,57 kHz	15,2 kHz	23,3 kHz
45,046	6,57 kHz	15,2 kHz	23,3 kHz

The computed natural frequencies do not change between the different simulations. Therefore, it is concluded that a mesh element count of approximately 45,000, as used for the static structural analyses, is also sufficient to obtain mesh independent modal analysis results.

References

Ainley, D. G. & Mathieson, G. C. R., 1951. *A method of performance estimation of axial-flow turbines,* London: Her Majesty's Stationary Office.

Aungier, R. H., 2006. *Turbine aerodynamics.* 1st ed. New York: ASME press.

Baskharone, E. A., 2006. *Principles of turbomachinery in air-breathing engines.* New York: Cambridge University Press.

Cengel, Y. A. & Boles, M. A., 2004. *Thermodynamics: an engineering approach.* Boston: McGraw-Hill Professional Publishing.

Chen, L.-C. & Lin, G. C. I., 2000. Reverse engineering in the design of turbine blades - a case study in applying the MAMDP. *Robotics and Computer Integrated Manufacturing,* pp. 161-167.

Chivate, P. N. & Jablokow, A. G., 1995. Review of surface representations and fitting for reverse engineering. *Computer Integrated Manufacturing Systems,* pp. 193-204.

Cohen, H., Rogers, G. F. C. & Saravanamuttoo, H. I. H., 1996. *Gas turbine theory.* Harlow: Longman Group Limited.

Creci, G., Menezes, J. C., Barbosa, J. R. & Corra, J. A., 2010. *Rotor-bearing analysis of a single spool gas turbine by considering bearing stiffness and damping dynamics.* Campina Grande, Brazilian Association of Mechanical Sciences and Engineering.

De la Calzada, P., 2011. Profile loss coefficient definitions revisited. *International Journal of Turbo Jet-Engines,* pp. 209-225.

De Wet, A. L., 2011. *Performance investigation of a turbocharger compressor.* Stellenbosch: Stellenbosch University.

Dixon, S. L., 1998. *Fluid Mechanics and Thermodynamics of Turbomachinery.* 4th ed. Oxford: Butterworth-Heinemann.

Djouimaa, S., Messaoudi, L. & Giel, P. W., 2007. Transonic turbine loading calculations using different turbulence models - effects of reflection and non-reflecting boundary conditions. *Applied Thermal Engineering,* pp. 779-787.

Dong, Y.-w., Bu, K., Dou, Y.-q. & Zhang, D.-h., 2011. Determination of a wax pattern die profile for investment casting of turbine blades. *Transactions of Nonferrous Metal Society of China,* pp. 378-387.

Japikse, D. & Baines, N. C., 1994. *Introduction to turbomachinery.* 1st ed. Oxford: Oxford university press.

Junhui, H., Zhao, W., Jianmin, G. & Yu, Y., 2010. *Overview of the profile measurement of a turbine blade and its development.* Wollongong, SPIE, pp. 76560L-1 - 76560L-11.

Korakianitis, T. & Papagiannidis, P., 1993. Surface curvature distribution effects on turbine cascade performance. *Journal of Turbomachinery,* 2(115), pp. 334-341.

Krige, D. S., 2012. *Performance evaluation of a micro gas turbine centrifugal compressor diffuser.* Stellenbosch: Stellenbosch University.

Lau, Y. L., Leung, R. C. K. & So, R. M. C., 2007. Vortex-induced vibration effect on fatigue life estimate of turbine blades. *Journal of Sound and Vibration,* pp. 698-719.

Mitchell, N. A., 1982. The preliminary analysis of axial turbines by a simplified throughflow procedure. *Journal of Mechanical Engineering Science,* pp. 5-10.

Mohaghegh, K., Sadeghi, M. H. & Abdullah, A., 2006. Reverse engineering of tubine blades based on design intent. *International Journal of Advanced Manufacturing Technology,* pp. 1009-1020.

Nickel Development Institute, 1995. *High-temperature high-strength Nickel base alloys (393).* [Online]
Available at: http://www.nickelinstitute.org/~/Media/Files/TechnicalLiterature/High_TemperatureHigh_StrengthNickel_BaseAlloys_393_.pdf#page=
[Accessed 21 September 2012].

Smith, S. F., 1965. A simple correlation of turbine efficiency. *Journal of Royal Aeronautical Society,* Issue 69, pp. 467-470.

Struwig, D., 2012. *Design and construction of a test bench for micro turbomachinery.* Stellenbosch: Stellenbosch University.

Van der Merwe, B. B., 2012. *Design of a centrifugal compressor impeller for micro gas turbine application.* Stellenbosch: Stellenbosch University.

Wesssels, F., Venter, G. & Von Backström, T., 2012. *An efficient scheme for describing airfoils using non-uniform rational B-splines.* Copenhagen, American Society of Mechanical Enigneers.

Wilson, D. G., 1987. New guidelines for the preliminary design and performance prediction of axial-flow turbines. *Proceedings of the Institution of Mechanical Engineers, Part A: Journal of Power and Energy,* pp. 279-290.